

I.M.M Ghazali

# The Impact of Wind Shear and Turbulence on the Loads and Performance of Wind Turbines





# The Impact of Wind Shear and Turbulence on the Loads and Performance of Wind Turbines

By

I.M.M Ghazali

For the degree of Master of Science in Sustainable Energy Technologies

at Delft University of Technology

to be defended publicly on Tuesday August 22, 2023 at 9:00 AM.

Supervisor:	Dr. ir. D. De Tavernier
	Dr. ir. D. Allaerts
Thesis committee:	Prof. dr. D. Von Terzi, TU Delft
	Dr. ir. S. Mulders, TU Delft
	Dr. ir. D. De Tavernier, TU Delft

An electronic version of this thesis is available at <http://repository.tudelft.nl/>.

*The cover photo is generated via Discort.com*





# Abstract

Operating in real-world conditions, modern large capacity wind turbines often experience off-design situations, enduring dynamic loads characterized by complex unsteady aerodynamics. Key among the challenges in predicting these dynamic loads is understanding the effects of wind shear and turbulence, both individually and in their complex interplay. This research aims to shed light on these phenomena, with an emphasis on their impacts on wind turbine fatigue loads and power production.

The research first provides an in-depth analysis of the influence of atmospheric stability on wind shear profile, aiming to extend the wind shear profile beyond the range of LiDAR measurements. Recognizing the limitations of existing power law and logarithmic law extrapolation methods, the study validates the use of multiple stability correction functions for accurate wind speed extrapolation. Subsequently, the research delves into the intricate effects of wind shear and turbulence on fatigue loads at the blade root of wind turbines, leveraging aeroelastic simulations. This research addresses the challenge of assessing wind turbine suitability for sites where one or several wind climate parameters surpass their design class values. It investigates the potential of the Response Surface Methodology (RSM) to estimate site-specific fatigue loads, a process that conventionally requires extensive aeroelastic simulations. This research also extends the scope to include the assessment of site-specific wind turbine power curves, validating the use of the Rotor Equivalent Wind Speed (REWS) and turbulence renormalization methods. Both methods show promise in estimating site-specific wind turbine power curves using a power curve measured under varying wind conditions.

In essence, this study emphasizes the significant impact of wind shear and turbulence on the performance and longevity of wind turbines. By shedding the light on potential improvements, this study hopes to contribute towards accurate power output and fatigue load assessments.

# Table of Contents

Abstract.....	v
Table of Contents.....	vi
List of Tables.....	viii
List of Figures.....	ix
<b>Chapter 1. Introduction.....</b>	<b>1</b>
1.1. Motivation.....	1
1.2. Aims and Objectives.....	2
1.3. Research Questions.....	2
1.4. Outline.....	3
<b>Chapter 2. Theoretical Background.....</b>	<b>4</b>
2.1. Atmospheric Stability.....	4
2.2. Wind Shear.....	6
2.3. Turbulence Intensity.....	7
2.4. Turbulence Spectra.....	8
2.5. Fatigue Loads.....	10
2.6. Power Production.....	11
<b>Chapter 3. Analysis of Offshore Wind Conditions.....</b>	<b>13</b>
3.1. Introduction.....	13
3.2. Data Collection.....	13
3.3. Atmospheric Conditions.....	15
3.3.1. Atmospheric Stability.....	15
3.3.2. Wind Shear Profile.....	17
3.3.3. Turbulence Intensity.....	18
3.4. Wind Shear Profile in Relation to Atmospheric Stability.....	20
3.4.1. Stability Correction Functions.....	20
3.4.2. Data Analysis.....	21
<b>Chapter 4. Simulation Tools.....</b>	<b>25</b>
4.1. The Aeroelastic Model.....	25
4.1.1. AeroDyn.....	26
4.1.2. ElastoDyn.....	26
4.1.3. ServoDyn.....	26
4.1.4. SubDyn.....	26
4.1.5. Inflow Conditions.....	27
4.2. Reference Turbine.....	27
4.3. Limitations.....	28
4.4. Simulation Cases.....	29
<b>Chapter 5. Fatigue Load Analysis in Relation to Atmospheric Conditions ...</b>	<b>30</b>
5.1. Introduction.....	30
5.2. Methodology.....	33
5.2.1. Fatigue Load Calculations.....	33
5.2.2. Artificial Site Development.....	34

5.2.3.	Response Surface Methodology .....	35
5.2.4.	Validation .....	36
5.3.	Results .....	37
5.3.1.	Fatigue Loads in Relation to Atmospheric Conditions .....	37
5.3.2.	Response Surface Methodology .....	41
5.4.	Summary and Conclusion.....	45
<b>Chapter 6.</b>	<b>Performance of Wind Turbines in Relation to Atmospheric</b>	
	<b>Conditions.....</b>	<b>47</b>
6.1.	Introduction.....	47
6.2.	Aim and Objectives.....	52
6.3.	Methodology.....	53
6.3.1.	Evaluating the Impact of Wind Shear and Turbulence Intensity on the Performance of Wind Turbines.....	53
6.3.2.	Rotor Equivalent Wind Speed Method.....	54
6.3.3.	Turbulence Renormalization Method.....	58
6.4.	Results .....	63
6.4.1.	Analysis of the Wind Shear and Turbulence Intensity Effects on Power Production of a wind turbine .....	63
6.4.2.	Assessment of Rotor Equivalent Wind Speed Methodology .....	66
6.4.3.	Assessment of Turbulence Renormalization Methodology .....	70
6.5.	Discussion and Conclusion.....	75
<b>Chapter 7.</b>	<b>Conclusions and Recommendations.....</b>	<b>78</b>
7.1.	Conclusion.....	78
7.1.1.	Analysis of Offshore Wind Conditions .....	78
7.1.2.	Analysis of Fatigue Loads in Relation to Site-Specific Atmospheric Conditions .....	79
7.1.3.	Power Production in Relation to Atmospheric Conditions .....	80
7.2.	Recommendations.....	81
<b>References.....</b>		<b>83</b>
Appendix A.	Measurements of Turbulence Intensity at Hollandse Kust (Zuid) Within 30° Directional Sectors. ....	91
Appendix B.	Calculation of REWS Segment Areas .....	92
Appendix C.	Examples of Calculating the Power Law Exponent Through a Linear Regression in a log(z)-log(u) Plot .....	93

## List of Tables

Table 1: Turbulence spectral parameters for the Kaimal model (IEC, 2005) .....	10
Table 2: Stability classes in terms of Obukhov length (Gryning et al., 2007).....	16
Table 3: Representation of wind shear profiles for four different cases.....	22
Table 4: Stability classes as a function of the dimensionless stability parameter $\zeta$ ...	22
Table 5: Key parameters for IEA 15-MW reference turbine (Gaertner et al., 2022)..	27
Table 6: Overview of simulation cases .....	29
Table 7: Overview of atmospheric conditions f Hollandse Kust (Zuid) that exceed the design limits of the IEA 15-MW reference turbine.....	34
Table 8: Overview of mean values and standard deviations of turbulence intensity and power law exponent at Hollanse Kust (Zuid) wind farm .....	35
Table 9: Wind climate parameters used for the central composite design and the upper range of the modified central composite design.....	36
Table 10: Wind climate parameters used for the lower range of the modified central composite design .....	36
Table 11: Overview of required simulations to validate the accuracy of the proposed response surface methods .....	37
Table 12: Estimated damage equivalent loads using the central composite design and a modified version of the central composite design .....	42
Table 13: Estimated damage equivalent loads for Class IB 15-MW reference turbine under Hollandse Kust (Zuid) atmospheric conditions.....	44
Table 14: Rotor equivalent wind speed (REWS) parameter values based on the depicted five segment heights (van Sark et al., 2019) .....	55
Table 15: Root Mean Square Error (RMSE) values corresponding to power curves fitted using the hub heigh wind speed method and the rotor equivalent wind speed method. The simulated power outputs are based on fixed wind shear exponents ranging from 0 to 0.3 for each wind speed bin. ....	68
Table 16: Root Mean Square Error (RMSE) values corresponding to power curves fitted using the hub heigh wind speed method and the rotor equivalent wind speed method. The simulated power outputs are based on potential variations in the wind shear profile based on semi-random selections of data obtained from Hollanse Kust (Zuid) wind farm .....	70

## List of Figures

Figure 1: Possible wind profiles in accordance to atmospheric stability (Viselli et al., 2022).....	7
Figure 2: Kaimal spectrum of turbulence for different values of turbulence intensities (Li et al., 2019) .....	9
Figure 3: Derivation of SN-curve (Zaayer, 2021) .....	11
Figure 4: Power curve for the IEA 15-MW reference turbine (Gaertner et al., 2022) 12	
Figure 5: Hollanse Kust (Zuid) wind farm layout (left) and wind rose (right) .....	14
Figure 6: (a) Stability classes as a function of wind speed at 150m height. (b) Weibull probability distribution with a shape factor $k=2.111$ and a scale factor $a=10.4577$ .....	17
Figure 7: (a) Mean power law exponent and standard deviation as a function of wind speed. (b) the mean Power Law exponent as a function of atmospheric stability and wind speed. ....	18
Figure 8: Turbulence Intensity as a function of wind speed at 150 meter height (left) and as a function of atmospheric stability (right).....	19
Figure 9: Power Law exponent as a function of TI and atmospheric stability (black: stable, blue: neutral, red).....	20
Figure 10: Observed and theoretical wind shear as a function of the dimensionless stability parameter. The wind shear profile is represented by the ratio of velocities (U) measured at two heights, (a) $U_{200}/U_{30}$ and (b) $U_{160}/U_{30}$ .....	23
Figure 11: Observed and theoretical wind shear as a function of the dimensionless stability parameter. The wind shear profile is represented by the ratio of velocities (U) measured at two heights, (a) $U_{200}/U_{100}$ and (b) $U_{160}/U_{100}$ .....	24
Figure 12: Working principle of OpenFAST (NREL, 2021).....	25
Figure 13: Overview of wind turbine layout (Gaertner et al., 2022) .....	28
Figure 14: 90% quantile turbulence intensity levels at Hollandse Kust (Zuid) wind farm (red), and the design turbulence intensity level of classB wind turbines (yellow) .....	31
Figure 15: Variation of two variable in central composite design, $\gamma = 2$ (Toft et al., 2016).....	32
Figure 16: Variations of variables in central composite design (a), and variation of variables in the modified central composite design (b) .....	35
Figure 17: Blade root damage equivalent load (DEL) in the flapwise direction as a function of wind speed (a), blade root DEL in the flapwise direction as a function of power law exponent (b), and a 3D representation of blade root DEL in the flapwise direction as a function of wind speed and PLE (c) .....	38
Figure 18: Blade root damage equivalent load (DEL) variations in the flapwise direction as a function of wind speed (a), Blade root DEL variation in the flapwise direction as a function of turbulence intensity (b), and a 3D representation of blade root DEL in the flapwise as a function of wind speed and turbulence intensity (c). ....	39

Figure 19: Interaction between turbulence intensity and power law exponent in relation to fatigue load assessment for wind turbines blade root in the flapwise direction.....	40
Figure 20: Distribution of data points for (a) turbulence intensity and (b) power law exponent across different wind speed bins, to which the response surface methodology will be applied.....	43
Figure 21: Estimation of Power production based on (a) Probability density function, (b) wind turbine power curve (Gaertner et al., 2022) .....	48
Figure 22: Influence of TI on power production (L. M. Bardal & Sætran, 2017).....	50
Figure 23: Rotor equivalent wind speed based on five different segments (van Sark et al., 2019) .....	54
Figure 24: Power curve based on hub wind speed (a) and equivalent wind speed (b) (L. Bardal et al., 2015).....	56
Figure 25: Extrapolation-based process for estimating wind speeds at multiple segments' heights .....	57
Figure 26: Process of applying turbulence renormalization method.....	58
Figure 27: simulating power for bin-averaged data.....	60
Figure 28: Example of zero-turbulence power curve derived from step 4 (a), and Newton's interpolation of the zero-turbulence power curve (b) .....	62
Figure 29: Differences in power output between a sheared wind profile and a uniform wind profile as a function of the shear exponent ranging from 0 to 0.5 .....	63
Figure 30: IEA 15-MW turbine's blade pitch at 5 m/s: uniform (blue) vs sheared (yellow) .....	64
Figure 31: IEA 15-MW turbine's power coefficient at 9 m/s: uniform (blue) vs sheared (yellow) .....	65
Figure 32: Effects of turbulence intensity on the power curve of the 15MW reference turbine.....	66
Figure 33: (a), Mean power curve and scatter obtained for two wind speed definitions: the hub height wind speed (blue) and the REWS (red). (b), zoom in of the power curve figure around 9 m/s at hub height.....	67
Figure 34: Example of particular instances (10-minute averaged data) where low-level jets occurred at 150 meters height in Hollandse Kust (Zuid) wind farm location. The power law exponent coefficient is calculated based on a linear regression in a $\log(z)$ - $\log(u)$ scale.....	69
Figure 35: power curve and scatter obtained for two wind speed definitions: the hub height wind speed (blue) and the REWS (red). .....	69
Figure 36: Stepwise figures of applying turbulence renormalization method.....	71
Figure 37: Estimated power curve using TI=15% power data to simulate TI=5% power curve (a) and estimated power curve using TI=5% power data to simulate TI=15% power curve (b).....	71
Figure 38: Estimated power curve using TI=15% power data to simulate TI=5% power curve (a) and estimated power curve using TI=5% power data to simulate TI=15% power curve (b). The correction formula proposed in Eq. (6.9) is followed.....	73
Figure 39: (a): zero turbulence power curve based on data representing very stable atmospheric conditions. (b): Estimated power curve during very unstable conditions using Clifton and Wagner's (2014) correction	

formula (Eq. (6.7)). (c): Estimated power curve during very unstable conditions by applying the new correction formula (Eq. (6.9)). The power curves are smoothed using a smoothing parameter of 0.99 to reduce the noise caused by the binning mechanism ..... 74

# Chapter 1. Introduction

Possible solutions to global warming and air pollution could be offered by renewable energy sources. However, for these renewable sources to provide a robust competition to conventional fossil fuel-based energy systems, they need to be financially sustainable. This includes the reduction of the average total costs of producing wind energy. As a result, there is a growing trend towards developing wind turbines with higher capacities. However, as the capacity of wind turbines increase, so do the challenges in estimating their energy yield production and the extent of loads they can endure. This thesis will therefore explore the effects of wind shear and turbulence on the loads and performance of large-scale wind turbines.

## 1.1. Motivation

Wind energy is the second most abundant source of renewable energy. It currently supplies more than 5% of the world's electricity (Valencia et al., 2018). Over the past decades, manufacturers are continuously developing larger-capacity wind turbines to benefit from the economy of scale. In 2020, the average capacity of offshore wind turbines installed in Europe was 8.2 MW and is expected to increase over the next decade (Wind Europe, 2021). Currently, the largest offshore wind turbine, Vestas V236-15 MW, was introduced in February 2021 and is now installed at Østerild Test Center in Denmark. It has a rotor diameter of 236 meter and a total height of 280 meters.

With the increase in size and capacity of wind turbines, it becomes necessary to accurately estimate their power curves and the amount of energy they produce. Conventionally, wind turbines' power curves are developed based on wind speed measurements that corresponds to the hub height, assuming that the atmospheric stability is near neutral (Ryu et al., 2022). This assumption can be valid for small wind turbines with short blade length since the variation of wind speed by height is relatively small. Thus, the error in predicted power output using hub height wind speed compared to the actual generated power is not large (Ryu et al., 2022; Scheurich et al., 2016). However, for larger wind turbines, the measured wind speed at the hub height does not necessarily represent the inflow across the turbine rotor disk. In the atmosphere, the vertical wind speed usually changes with height, a phenomenon known as "wind shear" (Murphy et al., 2020). Moreover, the wind inflow across the turbine disk is also turbulent in nature, thus varying in time. This increases the complexity of power output predictions, especially since these parameters are correlated through atmospheric stability (M. C. Holtslag, 2016). For instance, a stable boundary layer generally implies low turbulence but high shear. On the other hand, in an unstable boundary layer, the wind speed profile is nearly constant due to high level of turbulence and thermal mixing. As a result of these atmospheric conditions, power curves for the same wind turbine can differ from one location to another. Therefore, it is important to incorporate these effects into a power curve specific to a site location for accurate annual energy production (AEP) estimates.

Another important aspect in wind energy is fatigue load analysis. Wind turbines are designed to ensure that the exerted forces on their components do not cause failure over their lifetime. These forces stem from atmospheric conditions that cause non-uniform bending and fatigue, ultimately resulting in the malfunction or breakdown of the components. To ensure the wind turbine is strong enough without excessive individual component sizing, accurately prescribing the wind conditions for fatigue load assessment is crucial.

Wind turbines are generally designed according to the International Electrotechnical Commission (IEC) standards (IEC, 2005, 2009) with pre-defined wind turbine classes. However, in situations that any of the wind climate parameters at a particular site exceed their designed values, which is often the case (Toft et al., 2016), it is necessary to confirm the structural integrity through load calculations (IEC, 2005, 2009). However, estimating the wind turbine loads specific to a site requires numerous time-consuming and expensive aero-elastic simulations (Toft et al., 2016). For example, when simulating the fatigue damage using actual 10-minute wind measurements, it is necessary to conduct approximately 52,600 simulations for an entire year if only a single turbulence seed is considered. This necessitates the need for alternative methods to accurately estimate wind turbine loads in an efficient manner.

## 1.2. Aims and Objectives

The aim of this master's thesis is twofold. First, the effects of wind shear and turbulence intensity on wind turbine fatigue loads will be analyzed. Subsequently, site-specific fatigue load assessment methodologies will be explored and validated. Second, the impacts of wind shear and turbulence on the performance of a wind turbine will be examined. Consequently, different approaches to integrate their effects into a site-specific wind turbine power curve will be evaluated.

## 1.3. Research Questions

The main research question is phrased as:

**How do wind speed shear and turbulence intensity affect the loads and performance of a multi-megawatt offshore wind turbine?**

*The following is the list of important research questions that are derived from the main research question:*

**• How are wind turbine loads affected by changes in wind shear and turbulence?**

- How does wind shear influence the fatigue loads on a wind turbine?
- In what ways does turbulence contribute to the fatigue loads on a wind turbine?
- is there any interaction between wind shear and turbulence when considering fatigue load assessment?
- How can we determine site-specific fatigue loads while maintaining computational efficiency?

**• How do wind shear and turbulence factor into the projected annual energy output of a wind turbine?**

- In what ways does wind shear impact the energy generation capabilities of a wind turbine?
- How can we integrate wind shear effects into a site-specific wind turbine power curve?
- Can the application of Rotor Equivalent Wind Speed (REWS) reduce uncertainties in energy yield forecasts?
- What methodologies can be used to extend the shear profile beyond LiDAR measurements?
- How does turbulence influence the energy production efficiency of a wind turbine?
- How can we incorporate turbulence effects into a site-specific wind turbine power curve?

## 1.4. Outline

In **Chapter 1**, a brief introduction to the problems statement was discussed and the motivations of this thesis project was introduced. **Chapter 2** presents theoretical background of phenomena related to fatigue analysis and power production of wind turbines. **Chapter 3** discusses and analyses the measurement campaign data of Hollanse Kust Zuid offshore wind farm. Furthermore, it explores and validates different models used to describe the wind shear profile based on atmospheric stability. **Chapter 4** introduces the aeroelastic model and the reference wind turbine used for the analysis of this study. **Chapter 5** and **Chapter 6** investigate the effects of wind shear and turbulence on the loads and performance of wind turbines. Finally, conclusions and recommendations are presented in **Chapter 7**

# Chapter 2. Theoretical Background

This chapter provides an overview of the theoretical framework of the environmental factors which have the potential to impact the performance and loads of wind turbines. Such factors include terrain effect, surface friction, obstacles, wakes of nearby wind turbines, and atmospheric conditions (Kim et al., 2021). However, within the confines of this thesis, the concentration will exclusively be on the implications of atmospheric conditions, with particular emphasis on wind shear, turbulence intensity, and to a lesser degree, atmospheric stability.

## 2.1. Atmospheric Stability

Atmospheric stability refers to the tendency of the atmosphere to either resist or encourage vertical motion of air parcels. In other words, it describes the state of the atmosphere's vertical stratification, which determines whether air parcels will rise or sink. When the atmosphere is stable, air parcels that are displaced vertically tend to return to their original position. This is because the displaced air parcel is cooler and denser than the surrounding air, so it sinks back down to its original level. In contrast, when the atmosphere is unstable, displaced air parcels tend to rise and continue to rise until they reach a level where the surrounding air is of similar density (Stull & Ahrens, 2000).

The stability of the atmosphere is influenced by several factors, including the temperature and moisture content of the air. In meteorology, stability is often estimated using the potential temperature. If there are no condensation effects present, the temperature will change by 9.8 K/km in an adiabatic atmosphere as we move upwards (Stull & Ahrens, 2000). This change in temperature is defined as the potential temperature and is expressed as follows:

$$\theta(z) = T(z) + 0.0098z \quad (2.1)$$

Where,

$\theta(z)$  Potential temperature at a reference height  $z$

$T(z)$  Absolute temperature at a reference height  $z$

The above definition however does not consider the effect of moisture content in the air. As explained by Stull and Ahrens (2000), moisture content in the air affects the air density because water vapor has a lower molecular weight than dry air, and therefore occupies more space for the same mass. As a result, moist air is less dense than dry air at the same pressure and temperature. This means that if an air parcel contains more water vapor, it will be less dense than a dry air parcel at the same temperature and pressure. To account for the impact of humidity on potential temperature, the concept of virtual potential temperature is introduced. This value can be estimated under the assumption that the air is not fully saturated as follows:

$$\theta_v = \theta (1 + 0.61r) \quad (2.2)$$

Where  $\theta_v$  is the virtual potential temperature and the mixing ratio  $r$  is defined as the mass ratio between water vapour to dry air

When the virtual potential temperature is estimated at two different heights, one can determine if the atmospheric surface layer is in stable, neutral, or unstable conditions. If the virtual potential temperature increases with height, the atmosphere can be considered stable. In case the virtual potential temperature is constant with height, the atmosphere can be considered in neutral condition. Otherwise, the atmosphere shall be considered unstable.

The stability parameter is often represented by either the Obukhov length ( $L$ ) or by Richardson number ( $RI$ ). The Obukhov length is defined as the height at which shear and buoyancy effects produce the same amount of turbulent kinetic energy (Veldkamp, 2007) and is expressed as:

$$L = \frac{\overline{\theta}_v u_*^3}{\kappa g (\overline{w'\theta'})} = \frac{\overline{\theta}_v u_*^2}{\kappa g \theta_*} \quad (2.3)$$

Where,

$\overline{\theta}_v$	Mean virtual potential temperature
$u_*$	Friction velocity,
$\kappa$	Von Karman constant = 0.4
$g$	gravity acceleration
$(\overline{w'\theta'})$	Surface virtual potential heat flux,
$\theta_*$	surface layer temperature scale

In case of availability of high temporal resolution data,  $L$  can be directly calculated based on the eddy-covariance method and the observed turbulent fluxes of heat and momentum (M. C. Holtslag et al., 2014). However, in case of absence of these data,  $L$  can be estimated using empirical methods, most commonly using Richardson number which is defined as

$$RI = \frac{g \Delta \overline{\theta}_v \Delta z}{\overline{\theta}_v (\Delta \overline{u})^2} \quad (2.4)$$

Where  $\Delta \overline{u}$  is the change in the average wind speed across the height  $\Delta z$ .

In the literature, there are several methods in which the Richardson number can be calculated. The two most common are the Gradient-Richardson method (RI-G) and the bulk Richardson method (RI-B). The key distinction between these two methods lies in the data they utilize. The Gradient-Richardson method takes into account the wind speeds and temperature measurements from two distinct atmospheric heights. Conversely, the Bulk-Richardson method uses wind speed and temperature measurements from a single atmospheric height, in conjunction with surface temperature measurements.

Following Lange et al. (2004), the Obukhov length can be estimated using the Gradient-Richardson number:

$$L_{Grad} = \begin{cases} \left( \frac{z'}{RI_G} \right) & \text{If } RI_G < 0 \\ \left( \frac{z'(1 - 5RI_G)}{RI_G} \right) & \text{If } RI_G > 0 \end{cases} \quad (2.5)$$

$$z' = \frac{z_1 - z_2}{\ln\left(\frac{z_1}{z_2}\right)} \quad (2.6)$$

Where  $z_1 > z_2$ . Alternatively, the Obukhove Length can be estimated using the Bulk-Richardson method following Grachev & Fairall (1997)

$$\zeta = \begin{cases} 10RI & \text{If } RI < 0 \\ \left( \frac{10RI}{1 - 5RI} \right) & \text{If } RI > 0 \end{cases} \quad (2.7)$$

$$\zeta = \frac{z}{L} \quad (2.8)$$

Where  $\zeta$  is a dimensionless stability parameter, and  $z$  is the observation height.

## 2.2. Wind Shear

Wind shear refers to the change in wind speed as a function of height. It is a phenomenon that can occur at any altitude, but the effects are more pronoun in the lowest part of the atmosphere, the surface boundary layer (M. C. Holtslag, 2016). This variation in wind speed is often represented by the power law which is defined as

$$U(z) = U(z_r) \left( \frac{z}{z_r} \right)^\alpha \quad (2.9)$$

Where  $U(z)$  is the wind speed at a specific height  $z$ ,  $U(z_r)$  is the wind speed at the reference heigh  $z_r$  and  $\alpha$  is the wind shear power law exponent (PLE). The value of the PLE can change dependant on the mean wind speed, atmospheric stability, and other environmental factors (M. C. Holtslag, 2016). However, the power law fails to take the effects of atmospheric stability into account. A stable boundary layer generally implies a high wind shear profile, whereas in an unstable boundary layer, the wind profile is nearly constant due to turbulent mixing. An example of some possible wind shear profiles is shown in Figure 1 (Viselli et al., 2022).

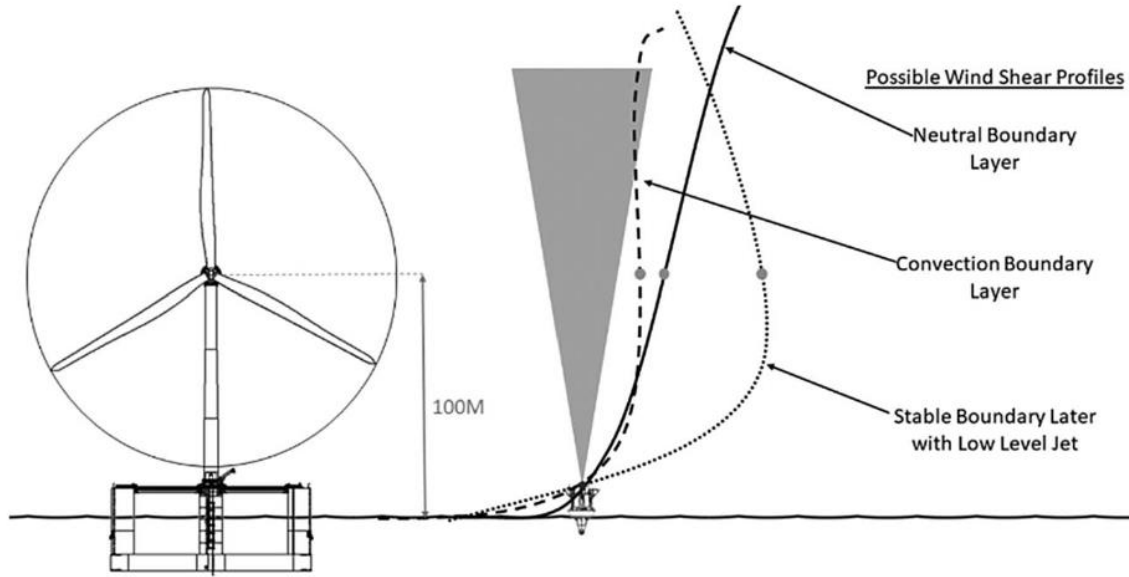


Figure 1: Possible wind profiles in accordance to atmospheric stability (Viselli et al., 2022)

Another method to represent the wind profile as a function of height is the logarithmic wind shear profile. The advantage of using this method is the possibility of including the stability effects. For neutral conditions, the logarithmic wind shear profile is defined as

$$\bar{U}(z) = \frac{u_{*0}}{\kappa} \ln\left(\frac{z}{z_0}\right) \quad (2.10)$$

Where  $u_{*0}$  is the surface friction velocity representing the shear stress exerted by wind on the surface and  $z_0$  is the surface roughness which is defined as the height of the roughness elements (e.g. open land, built environment, offshore). Both  $u_{*0}$  and  $\kappa$  are assumed to be constant with height.

For stable and unstable conditions, the logarithmic wind shear profile can be expressed as:

$$\bar{U}(z) = \frac{u_{*0}}{\kappa} \left[ \ln\left(\frac{z}{z_0}\right) - \Psi(\zeta) + \Psi(\zeta_0) \right] \quad (2.11)$$

Where  $\Psi$  is the stability correction function and  $\zeta_0 = z_0/L$ . The correction function  $\Psi(\zeta_0)$  on the right side of the equation can be neglected since its value is much less than  $\Psi(\zeta)$ . Several methods for estimating the value of  $\Psi(\zeta)$  have been proposed based on empirical observations (Beljaars & Holtslag, 1991; Businger et al., 1971; Dyer, 1974; A. a. M. Holtslag & Bruin, 1988). The applicability of each module will be evaluated in Chapter 3.

## 2.3. Turbulence Intensity

Turbulence intensity is a measure of the amount of turbulence in a fluid flow. It is usually expressed as a percentage and is defined as the root mean square (RMS) of

the velocity fluctuation divided by the mean velocity of the flow. Both turbulence ( $\sigma$ ) and turbulence intensity (TI) are respectively defined as

$$\sigma^2 = \frac{1}{T} \int_0^T (U(t) - \bar{U})^2 dt \quad (2.12)$$

$$TI = \frac{\sigma}{\bar{U}} \quad (2.13)$$

Where  $U(t)$  is the wind speed measured during a time interval  $T$  (e.g. 10 minutes), and  $\bar{U}$  is the mean wind speed during that time interval.

Turbulent flows exhibit irregular patterns, unpredictable behavior, and have multiple time and space scales. They arise when the kinetic energy source driving the fluid's motion is powerful enough to overcome viscosity. Conversely, when viscosity dominates, the flow is laminar, predictable, and regular (Bailly & Comte-Bellot, 2015). The unpredictable feature of turbulence and the interaction of large range of scales can be captured through Navier-Stokes equations. For an incompressible flow, it is defined as

$$\rho \left( \frac{\partial \mathbf{u}}{\partial t} + \mathbf{u} \cdot \nabla \mathbf{u} \right) = -\nabla p + \mu \nabla^2 \mathbf{u} \quad (2.14)$$

Where  $\mathbf{u}$  is the velocity vector,  $\rho$  is the fluid density,  $p$  the pressure and  $\mu$  the dynamic molecular viscosity.

While the Navier-Stokes equations are fundamental to understanding the dynamics of fluid motion, they are extremely complex and computationally intensive, making them difficult to solve for real-world turbulent flows. Turbulent flow involves a wide range of length and time scales which makes it impossible to solve the Navier-Stokes equations analytically. Therefore, the concept of turbulence spectra will be introduced which provides a simplified and useful way to describe the statistical properties of turbulence in the atmosphere, without requiring the full solution of Navier-stokes equations.

## 2.4. Turbulence Spectra

Turbulence spectra is a mathematical representation of how the energy of turbulent fluid flows is distributed across different length scales. The energy of turbulence is composed of eddies of different sizes, ranging from large-scale eddies that are hundreds of meters in size to small-scale eddies that are only a few millimeters in size.

The spectrum of turbulence is typically represented using the power spectral density function (IEC, 2005), which describes how the energy of turbulence is distributed over different frequencies or length scales. The power spectral density function is a mathematical function that represents the energy at each frequency or length scale.

The two most commonly used turbulence models recognized by IEC design standards are the Mann uniform shear turbulence model and Kaimal spectral model (IEC, 2005). The IEC guidelines for design load calculations recommend the use of Man uniform

turbulence model, however, it is common in the literature to use the Kaimal spectral model in offshore and open flat terrain conditions (M. C. Holtslag, 2016; Slot et al., 2018; Toft et al., 2016; Veldkamp, 2007). Though the Mann model may possibly be applicable for offshore as well, it was not derived based on these scaling principles, but derived based on linearization of Navier-Stokes equations (M. C. Holtslag, 2016). The work of Holtslag (2016) also concluded that the Kaimal spectrum can be used quite accurately to describe the median of all spectra in different stability classes. Therefore, the use of Kaimal spectrum will be adopted in this thesis. A graphical representation of the Kaimal spectrum for different turbulence intensities is shown in Figure 2 (Li et al., 2019). The y-axis depicts the power spectrum and the x-axis depicts its frequency.

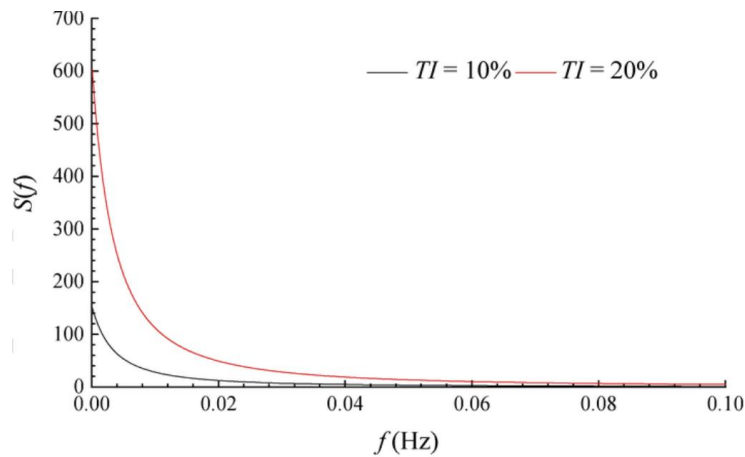


Figure 2: Kaimal spectrum of turbulence for different values of turbulence intensities (Li et al., 2019)

The component power spectral densities are given in a non-dimensional form as (IEC, 2005)

$$\frac{f S_k(f)}{\sigma_k^2} = \frac{4fL_k/V_{hub}}{(1 + 6fL_k/V_{hub})^{5/3}} \quad (2.15)$$

And

$$\sigma_k^2 = \int_0^{\infty} S_k(f)df \quad (2.16)$$

Where,

- f Frequency (Hz)
- k velocity directional component (1 = longitudinal, 2 = lateral, and 3 = upwards)
- $S_k$  velocity component spectrum
- $\sigma_k$  velocity component standard deviation,
- $L_k$  velocity component integral scale parameter.

The spectral parameters for each velocity component k is presented in Table 1 (IEC, 2005)

Table 1: Turbulence spectral parameters for the Kaimal model (IEC, 2005)

	Velocity component (k)		
	1	2	3
$\sigma_k$	$\sigma_1$	$0.8 \sigma_1$	$0.5 \sigma_1$
$L_k$	$8.1 \Lambda_1$	$2.7 \Lambda_1$	$0.66 \Lambda_1$

The longitudinal turbulence scale parameter ( $\Lambda_1$ ) is given by (IEC, 2005)

$$\Lambda_1 = \begin{cases} 0.7z & \text{If } z \leq 60m \\ 42m & \text{If } z \geq 60m \end{cases} \quad (2.17)$$

## 2.5. Fatigue Loads

Fatigue is a phenomenon whereby repeated fluctuations in load, even if these loads are below the static yield limit, can ultimately cause a material to fail. This typically happens because localized stresses, often triggered by surface flaws that lead to stress concentration, can exceed the yield limit, and cause localized plastic deformation (Veldkamp, 2007). When the load varies, there may be new instances of plastic deformation with each cycle, which can create micro cracks that eventually develop into larger cracks and cause the component to fail. The primary challenge lies in accurately predicting the lifespan of components under variable loading conditions, with lifespan defined as the time until a crack of a specified length or depth is formed, or until the component collapses (Veldkamp, 2007).

The SN-curve or Wohler curve is one way to indicate the durability of a turbine component in terms of fatigue by showing the relationship between the number of cycles before failure (N) and the stress (S) caused by constant cyclic loads. For wind turbine blades, this relationship can be expressed using the modified Minor (or Corten-Dolan) rule (Veldkamp, 2007) which implies the following relation

$$\log(S) = \log(UCS) - \frac{1}{m} \log(N) \quad (2.18)$$

Thus

$$N = \left( \frac{UCS}{S} \right)^m \quad (2.19)$$

Where UCS is the Ultimate Compressive Strength, and m is the Wohler exponent (or slope of SN-curve) which is derived from experimental data as shown in Figure 3 (Zaayer, 2021).

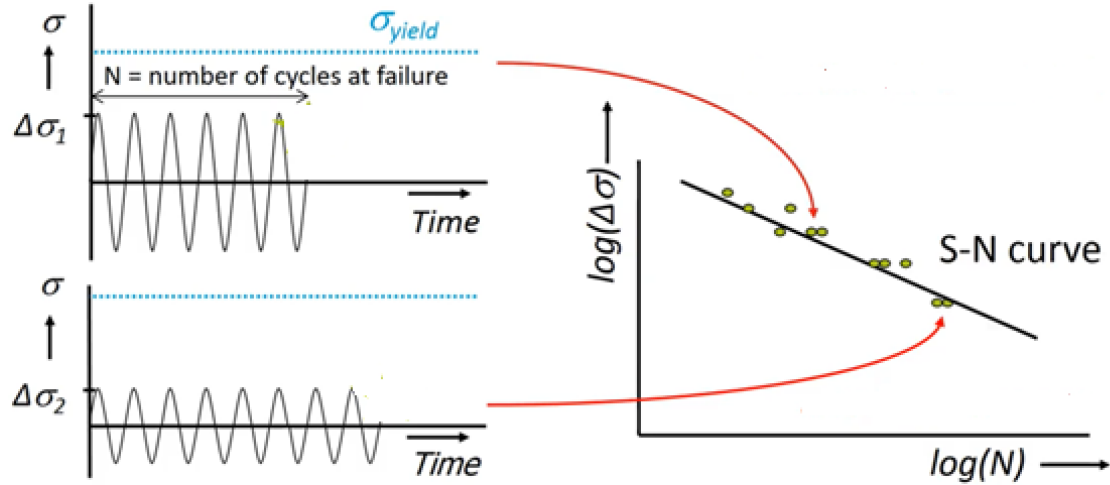


Figure 3: Derivation of SN-curve (Zaayer, 2021)

According to Miner's hypothesis (IEC, 2005), when a load occurs  $n$  times rather than the number of cycles before failure ( $N$ ), a proportion of the component's lifetime equal to  $d=n/N$  is consumed. This proportion is referred as partial damage. If the sum of all partial damages is equal to 1, the component will fail. By using this hypothesis, one can determine the total damage caused by all loads combined

$$D = \sum_j d_j = \sum_j \frac{n_j}{N_j} \quad (2.20)$$

Another important concept to be introduced is the so-called damage equivalent load (DEL). The DEL represents the load that for some chosen number of cycles  $N_{EQ}$  would produce the same damage as all loads combined as follows

$$DEL = \sqrt[m]{\frac{1}{N_{EQ}} \sum_j N_j (\Delta F_j)^m} \quad (2.21)$$

or

$$DEL = \sqrt[m]{\frac{1}{N_{EQ}} \sum_j D_j (UCS)^m} \quad (2.22)$$

## 2.6. Power Production

Wind turbines convert wind power to mechanical power and then to electricity. Wind power  $P_w$  is a function of the wind speed cubed, air density  $\rho$ , and the overall area  $A$ .

$$P_w = \frac{1}{2} \rho A U^3 \quad (2.23)$$

The process of obtaining energy from wind turbines involves the reduction of wind speed. There is a theoretical limit to the amount of energy that can be extracted by wind turbines from wind energy. That theoretical limit is around 59.3% and is known

as the Betz limit. This limit was derived from the principle of conservation of mass and momentum of the wind stream flowing through an idealized actuator disk. For wind turbines to extract 100% of wind's power, it would require to stop all wind flow, which is impossible without having a solid rotor disk that cannot turn and generate kinetic energy. Practically, modern wind turbines only achieve around 75-85% of Betz limit due to various electrical and mechanical losses (Burton, 2001).

To consider these inefficiencies on the power output of a wind turbine, the power coefficient ( $C_p$ ) is introduced. It is the ratio of the net electrical power output of a wind turbine to the power available from the freestream wind. Therefore, the overall power output of a wind turbine can be expressed as:

$$P = \frac{1}{2} \rho C_p A U^3 \quad (2.24)$$

Typically, wind turbines operate under three to four distinct control regions (Cooperman & Martinez, 2014). An example of a wind turbine power curve along with the control regions is given in Figure 4 (Gaertner et al., 2022). Under region 1.5 and above the cut-in wind speed, a PI controller on the generator torque is used to regulate the turbine speed to its minimum design set value. This design minimum value is usually set to avoid any resonance which can ultimately lead to failure. Under region 2, below rated wind speed, the rotor speed is regulated to operate at the turbine's optimal tip speed ratio (TSR). In this region, the power coefficient ( $C_p$ ) is maximized. Finally, in region 3, above the rated wind speed and below the cut-out wind speed, the turbine's blade pitch controller is used to regulate the rotor speed to achieve the wind turbine's rated power.

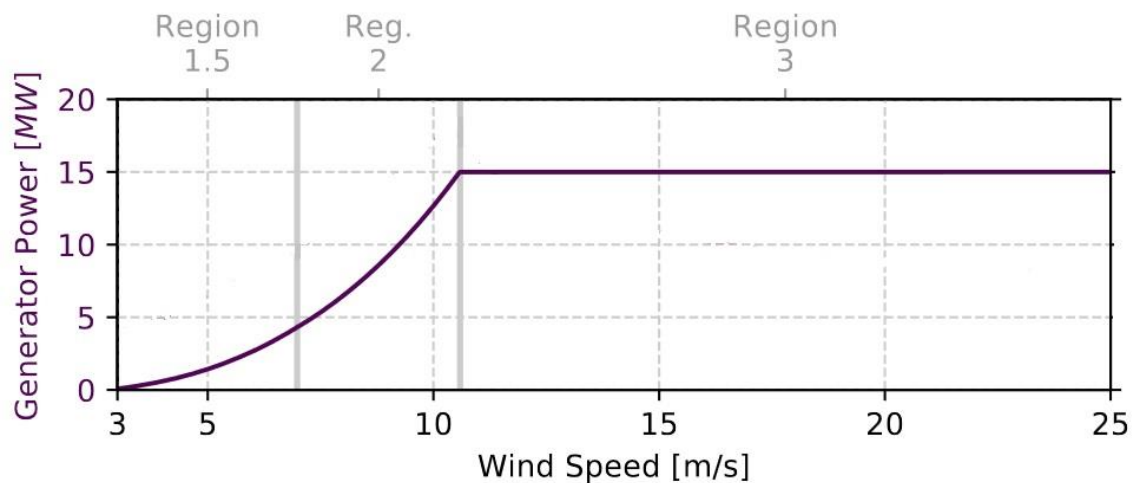


Figure 4: Power curve for the IEA 15-MW reference turbine (Gaertner et al., 2022)

# Chapter 3. Analysis of Offshore Wind Conditions

## 3.1. Introduction

In this chapter, the meteorological measurement data at the Hollandse kust Zuid (HKZ) will be presented and further analyzed. The measurement data will be used in later chapters to construct realist scenarios for simulation purposes. First, in section 3.2, the measurement campaign will be briefly summarized to establish an overview of how the data was collected and validated. All campaign description, specifications and data collection have been obtained from (Fugro, 2018). Next, section 3.3 will further analyze the data to describe the atmospheric conditions at the site location. Finally, section 3.4 will validate existing wind shear profile models in relation to atmospheric stability.

## 3.2. Data Collection

The measurement campaign has been conducted by Fugro through the deployment of two Seawatch Wind LIDAR Buoys (SWLB) at the site location. The purpose of the campaign was to obtain two sets of high-quality meteorological and oceanographic (metocean) data, including wind profiles, over a period of two years from June 2016 until June 2018. The deployed buoys were equipped with a motion sensor, an air pressure sensor, an air temperature sensor, a humidity sensor, and a wind sensor measuring winds at 4 m above sea level.

The wind farm layout along with the wind speed distribution over its direction is presented in Figure 5. The location of the two buoys referred to as HKZA and HKZB are encompassed by the purple rectangles. It should be noted that the two measurement stations are within 10-15 km away from the nearby wind farm, Luchterduinen (represented by the green area in Figure 5). Moreover, Hollandse Kust (Zuid) wind farm is located around 20 km away from shore. Therefore, it is possible that campaign data measurements could be affected by the nearby wind farm wake or the onshore surface roughness.

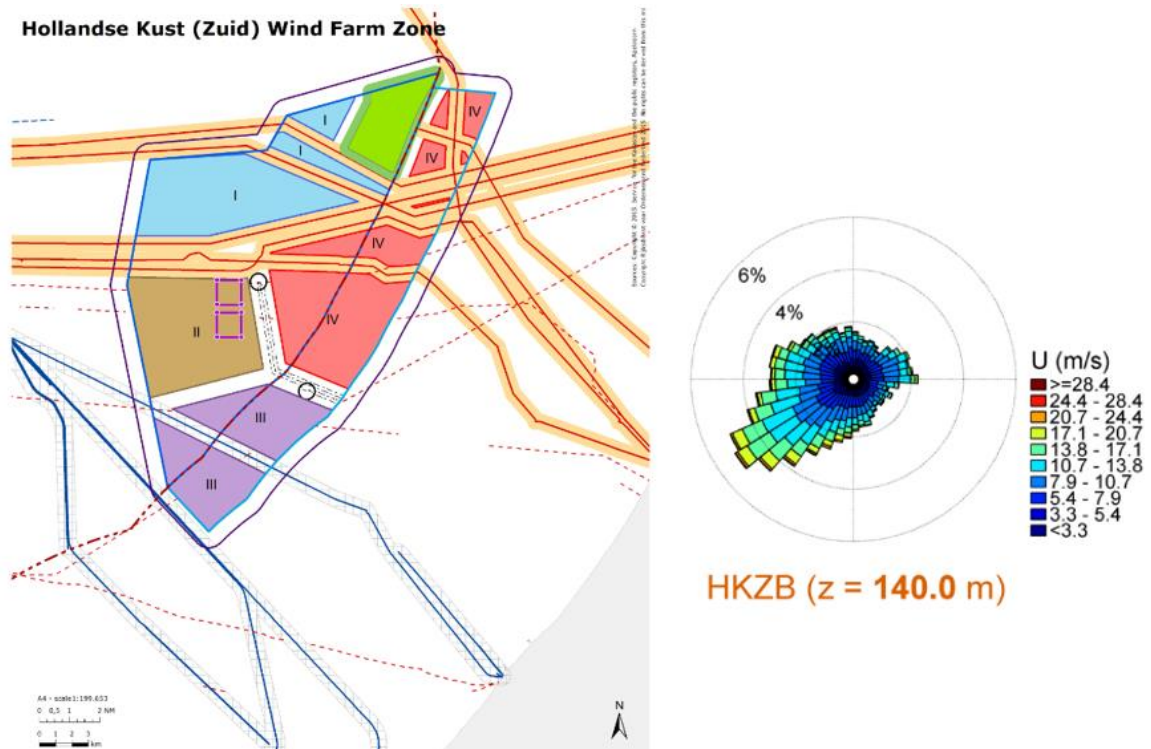


Figure 5: Hollandse Kust (Zuid) wind farm layout (left) and wind rose (right)

The wind speed measurements and direction profiles are collected by two types of wind sensors, the Gill Windsonic and ZephIR 300 LIDAR. The LIDAR wind speed and direction measurements are taken at height levels of 4, 30, 40, 50, 80, 100, 120, 140, 160, 180 and 200 m above sea surface. The LiDAR emits a steady beam of light from its top window, which is angled away from the vertical and rotates around a central axis once every second. This scanning motion allows the LiDAR to continuously survey a cone-shaped area in the air. A focus stage within the LiDAR helps to concentrate the returning light from a specific elevation and samples individual points of the sightline around the circle. The magnitude of the Doppler shift of the backscattered light from each of these individual points is analyzed to create a representation of the wind field at that particular elevation over a one-second interval.

The LiDAR device sequentially focuses on 10 chosen elevations to sample the wind profile. After each elevation profile, the LiDAR carries out additional tasks such as detecting precipitation, fog and cloud base, and measuring the reference height of 38 m above the laser before moving on to the next profile. The time interval between each profile is approximately 17 seconds. The wind profiles collected at 17-second intervals are combined to create a time series that represents the average horizontal and vertical wind over a 10-minute period. The SWLB Wavesense3 processing unit utilizes an algorithm that incorporates data from other sensors to generate the 10-minute averages from each 1-second sample. The LiDAR measurements are then validated against anemometer observations at platform K13a (K13), Lichteiland Goeree (LEG), and EuroPlatform (EPL) as per the requirements of IEC standards (IEC, 2005, 2009).

The air temperature and humidity are measured at 4 m height above sea surface using HPM155 and HUMICAP180R sensors. The surface temperature measured at 1 m below sea surface is sampled by Nortek Aquadopp current meter. The air pressure is measured by the Vaisala pressure sensor PTB330A which is located inside the buoy.

The Turbulence Intensity (TI) defined as  $TI = (\sigma/\bar{u})C$  is calculated by the SWLB Wavesense3 processing unit. The constant  $C=0.95$  is needed to convert the scan-averaged LIDAR measurements to the point measurements of a cup anemometer. It is important to mention that this definition frequently provides relatively high values of TI when the wind speed is low but variable. However, this should not be a concern since low wind speeds contribute very little when considering the overall fatigue loads and power output of wind turbines (Veldkamp, 2007).

### 3.3. Atmospheric Conditions

The measurements data of Hollandse Kust (Zuid) are further analyzed to determine the atmospheric stability, wind shear profile, and the turbulence intensity. This analysis will be used in later chapters to establish realistic wind conditions which are used for simulation purposes.

#### 3.3.1. Atmospheric Stability

Due to the absence of measurements of turbulent fluxes of heat and momentum, the eddy-covariance method cannot be used to determine the Obukhov length near the surface. An alternative approach is to utilize the Bulk-Richardson number to estimate  $\zeta$  as described by Grachev & Fairall (1997). This method involves obtaining 10-minute mean observations of the surface temperature, as well as the temperature and wind speed at a height of 4 m. The virtual potential temperature is calculated at both the surface and 4 m height as

$$\overline{\theta}_v(z) = (T(z) + 0.0098z) [1 + 0.61r] \quad (3.1)$$

The mixing ration  $r$  is calculated as

$$r = \frac{\epsilon_R e}{P - e} \quad (3.2)$$

Where  $P$  is the air pressure measured in pascals,  $\epsilon_R = 0.622$  is the ratio between the gas constant of dry air and water vapour, and  $e$  is the vapor pressure expressed as a function of the relative humidity (RH) and the saturated pressure at equilibrium over pure water ( $e_s$ ). It is approximated using the Clausius-Clapeyron equation (Stull & Ahrens, 2000)

$$e = e_s RH \quad (3.3)$$

$$e_s = e_0 \cdot \exp \left[ \frac{L}{\mathfrak{R}_v} \left( \frac{1}{T_0} - \frac{1}{T} \right) \right] \quad (3.4)$$

Where the water-vapor gas constant  $\mathfrak{R}_v = 461 \text{ J.K}^{-1}.\text{kg}^{-1}$ ,  $e_0 = 0.6113 \text{ KPa}$ ,  $T_0 = 273.15 \text{ K}$ , and the latent-heat parameter for liquid water is  $L = 2.5 \times 10^6 \text{ J.kg}^{-1}$ , giving  $\frac{L}{\mathfrak{R}_v} = 5423 \text{ K}$ . The surface pressure and surface relative humidity at the offshore location are assumed to be 101.3 kPa and 100% respectively (Grachev & Fairall, 1997)

The dimensionless stability parameter  $\zeta$  is calculated following Grachev and Fairall method (1997). To use the Richardson bulk method, one needs to know the sea surface temperature. However, since this is not available at HKZ, the temperature of the water at a depth of 1 meter is used instead. Due to the cool skin effect, this temperature is typically slightly higher than the actual skin temperature (Fairall, Bradley, Godfrey, et al., 1996). As a result, the temperature difference between the surface and 4 meters is slightly overpredicted, leading to an overprediction of the stability parameter. This means that the calculated values of 4m/L are slightly too high for stable conditions and too low for unstable conditions. However, following Grachev and Fairall (1997), the calculated stability parameters are assumed to be unaffected.

Table 2: Stability classes in terms of Obukhov length (Gryning et al., 2007)

Stability Class	Range of Obukhov Length
Very Unstable (VS)	$-200 < L < 0$
Unstable (U)	$-500 \leq L < -200$
Neutral (N)	$ L  > 500$
Stable (S)	$200 < L \leq 500$
Very Stable (VS)	$0 < L \leq 200$

The boundaries of stability classes in relation to Obukhov length are presented in Table 2 (Gryning et al., 2007). The frequency of stability classes occurrences along the Weibull probability distribution function ( $k=2.11$ ,  $a=10.46 \text{ m/s}$ ) at 150m height are shown in Figure 6. Both the mean and median wind speeds are found to be 9.25m/s and 8.73m/s respectively.

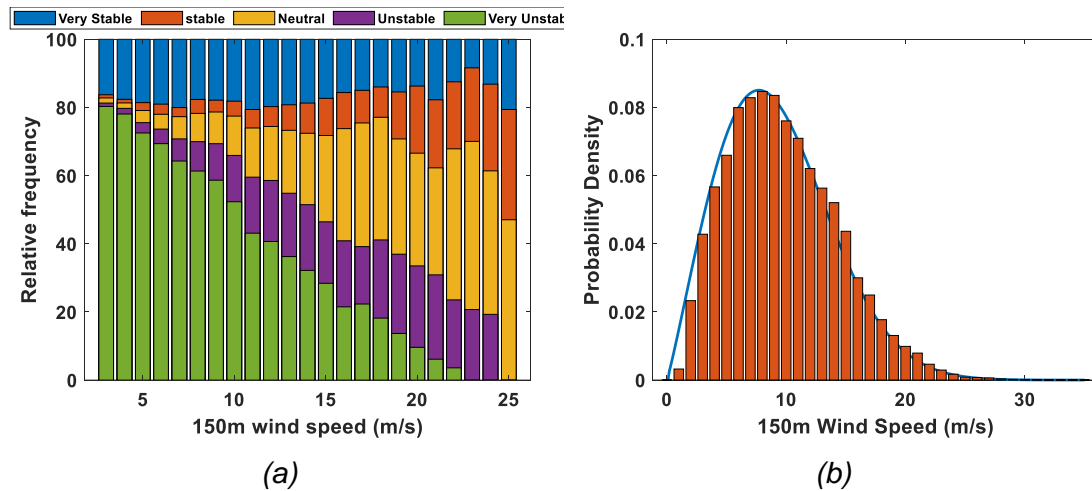


Figure 6: (a) Stability classes as a function of wind speed at 150m height. (b) Weibull probability distribution with a shape factor  $k=2.111$  and a scale factor  $a=10.4577$

Assessment of Figure 6 reveals that for the lower range of wind speeds (below 10 m/s), the occurrence of very unstable conditions is predominant at Hollandse Kust (Zuid) wind farm, followed by very stable conditions. For strong wind speeds (above 15 m/s), it is found that neutral are more frequent. In moderate wind speeds (15-20 m/s), both the occurrences of very stable conditions and very unstable conditions decline when the wind speed increases, and the occurrence of stable, neutral, and unstable conditions increase as a function of wind speed.

In general, it is found that the atmospheric conditions shift from predominately unstable conditions at lower wind speeds to predominately neutral conditions at the higher range of wind speeds. These results align well with Holtslag et al. (2014) who analyzed the atmospheric stability for far offshore wind conditions. Moreover, it is expected that high wind speeds are often associated with neutral atmospheric conditions (Stull & Ahrens, 2000), which was also found to be the case based on the analysis of Hollandse Kust (Zuid) wind farm.

### 3.3.2. Wind Shear Profile

Based on wind speed measurements at heights of 30 m, 60 m, 80 m, 100 m, 120 m, 140 m, 160 m, 180 m, and 200 m, the wind shear power law exponent is determined at each 10-minute time-step average measurements. Following Slot et al. (2018), the wind speed measurements at the different heights were arranged in a  $\log(z)$ - $\log(u)$  plot, and the shear exponent is determined based on the least squares linear regression method (refer to Appendix C.).

As demonstrated in Figure 7 (a), the mean power law exponent (PLE) tends to increase as wind speed increases, while the standard deviation decreases. This observation is in line with expectations, as it indicates a shift in atmospheric stability. At lower wind speeds, the atmospheric conditions are very unstable, which results in low values and larger variations in the PLE. As wind speeds increase, the atmosphere becomes more neutral, leading to a more consistent and higher PLEs.

In general, it is expected that very stable atmospheric conditions lead to higher values of PLEs, while very unstable conditions lead to lower values of PLE. While this was found applicable for very unstable conditions, it is observed from Figure 7 (b) that low and even negative values of PLE can occur at the lower range of wind speeds during very stable, stable, and neutral atmospheric conditions. This could be explained as the thickness of the surface boundary layer is reduced when the stability parameters increase (M. C. Holtslag, 2016). In return, low-level jets can occur at heights even below 100 meters which can result in low or negative PLE (Gutierrez et al., 2016).

These findings highlight the importance of considering atmospheric stability when studying wind shear and its relationship with wind speed. The results indicate that the wind shear profile can vary significantly depending on the stability of the atmosphere, emphasizing the need to account for atmospheric conditions when analyzing and modeling wind behavior.

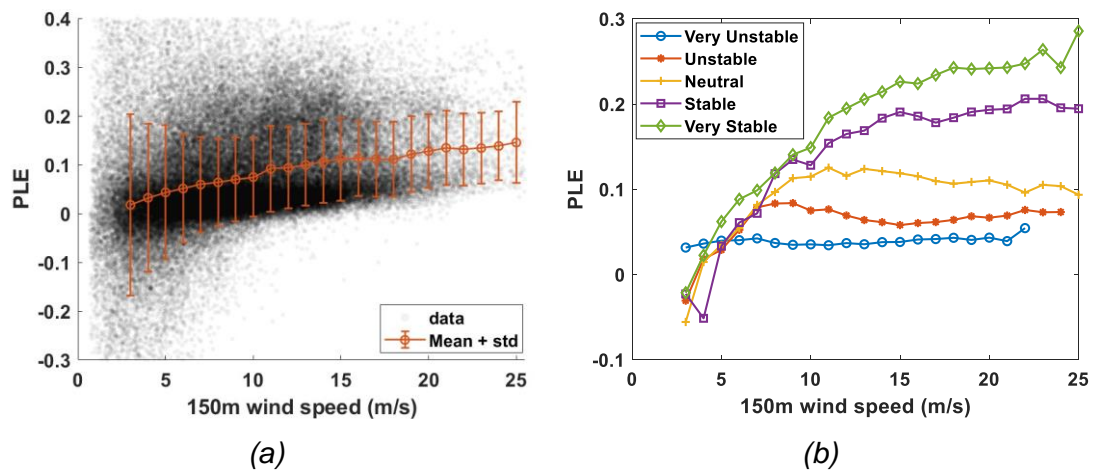


Figure 7: (a) Mean power law exponent and standard deviation as a function of wind speed. (b) the mean Power Law exponent as a function of atmospheric stability and wind speed.

### 3.3.3. Turbulence Intensity

The average turbulence intensity is calculated within a specific range of wind speeds, from 3m/s to 25m/s, using a 1m/s interval. This binning method is used to help organize the data and provides a more detailed understanding of turbulence intensity across different wind speed ranges.

The variation of TI as a function of wind speed and atmospheric stability is shown in Figure 8. It is found that high TI values are primarily associated with lower wind speeds, specifically below 6 m/s. As wind speed increases within the range of 6-10 m/s, TI continues to decline. However, for wind speeds above 10 m/s, there is an observed change in behavior as TI starts to increase. This can again be explained considering the atmospheric stability. For lower wind speeds, very unstable conditions dominate, contributing to higher TI values. As wind speeds increase, the occurrence of neutral atmospheric conditions becomes more frequent, leading to a decline in average TI.

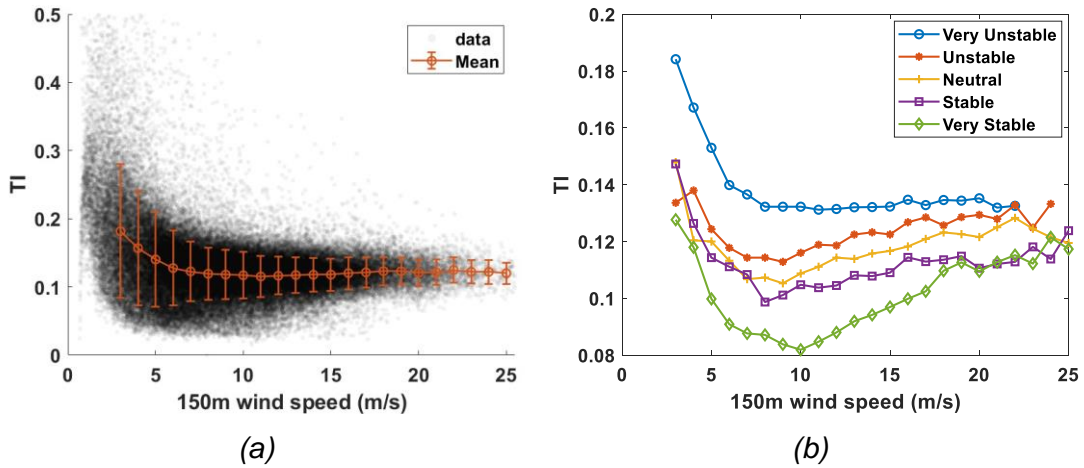


Figure 8: Turbulence Intensity as a function of wind speed at 150 meter height (left) and as a function of atmospheric stability (right)

It can be noticed from Figure 8 that the mean TI values are relatively high when compared to the analysis of other offshore locations (Eecen & Machiels, n.d.; Sakagami et al., 2022; Viselli et al., 2022). It is expected that main reason for this is associated to the proximity to the nearby Luchterduinen wind farm, which is located around 11 km from HKZA and HKZB measurement locations. Based on a 30° directional analysis of the turbulence intensities (see Appendix A.), this indeed was found to be the case. It is found that TI values are highest at the 180° -210° directional sector, which aligns with the direction of the wind approaching from the near-by wind farm.

The correlation between turbulence intensity and wind shear exponent through atmospheric stability can be observed in Figure 9. In general, it is found that the mean PLE decreases as TI increases. This implies that higher turbulence intensity is associated with a decrease in the mean PLE. However, an exception to this relationship is noted for TI values below 0.05. In this range, the expected decrease in mean PLE with increasing TI did not hold true. This deviation could be attributed to the occurrence of low-level jets. Low-level jets are strong, localized wind features typically observed within the boundary layer (M. C. Holtslag, 2016). They are characterized by high wind speeds at a specific height and can disrupt the expected relationship between TI and the PLE. The presence of low-level jets may introduce additional complexity to the wind shear patterns and turbulence characteristics, leading to deviations from the typical TI-PLE correlation.

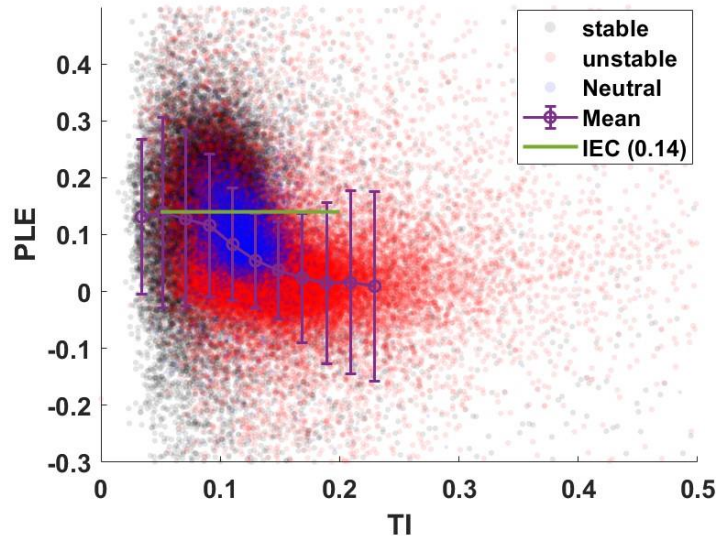


Figure 9: Power Law exponent as a function of TI and atmospheric stability (black: stable, blue: neutral, red)

### 3.4. Wind Shear Profile in Relation to Atmospheric Stability

The field measurements of Hollandse Kust Zuid extend to a maximum height of 200 meters above sea surface level. However, the heights of new large capacity wind turbines can extend beyond these measurements. It is recognized that the wind profile over height does not always follow the power law or the logarithmic law due to its dependence on atmospheric stability.

Therefore, the aim of this section is to validate multiple stability correction functions proposed in literature against the actual site measurement data.

#### 3.4.1. Stability Correction Functions

The general expression of the wind shear profile was denoted earlier in Eq. (2.11). The concept of the stability correction function was introduced but not validated. There are several methods proposed in the literature to estimate the value the stability correction function  $\Psi(\zeta)$ . The two most frequently used in meteorology and wind energy as suggested by Holtslag (2016) are the Businger and Dyer stability correction functions (Businger et al., 1971; Dyer, 1974) which are expressed as:

$$\Psi(\zeta \leq 0) = 2 \ln\left(\frac{1+x}{2}\right) + \ln\left(\frac{1+x^2}{2}\right) - 2 \arctan(x) + \frac{\pi}{2} \quad (3.5)$$

$$\Psi(\zeta \geq 0) = -\beta\zeta \quad (3.6)$$

Where  $x = [1 - \gamma\zeta]^{\frac{1}{4}}$ ,  $\gamma = 19.3$  and  $\beta = 6.0$  following Högström (1988).

For very unstable conditions, it can be assumed that the effects of the friction velocity ( $u_0$ ) are no longer valid (M. C. Holtslag, 2016). Accordingly, the so-called free convection stability correction is proposed (Carl et al., 1973)

$$\Psi(\zeta \leq 0) = 1.5 \ln\left(\frac{y^2 + y + 1}{3}\right) - \sqrt{3} \arctan\left(\frac{2y + 1}{\sqrt{3}}\right) + \frac{\pi}{\sqrt{3}} \quad (3.7)$$

Where  $y = [1 - \gamma\zeta]^{\frac{1}{3}}$  and  $\gamma = 12.87$  inline with Fairall et al. (1996). Note that Eq. (3.7) has been validated for moderate unstable conditions as explained by Högström (1988). However, following Holtslag (2016), it will be assumed valid for all unstable conditions.

During very stable atmospheric conditions, the linearity of the correction function as shown in Eq. (3.6) results in overestimating the effects of wind shear as observed by Holtslag and Bruin (1988) and Brutsaert (1982). As such, two alternative stability correction functions have been proposed. The formulation of Holtslag and Bruin (1988) is given by:

$$\Psi(\zeta \geq 0) = -a\zeta - b\left(\zeta - \frac{c}{d}\right) \exp(-d\zeta) - \frac{bc}{d} \quad (3.8)$$

Where  $a = 1$ ,  $b = 2/3$ ,  $c = 5$ ,  $d = 0.35$  following Beljaars and Holtslag (1991). The other formulation developed by Brutsaert (1982) is given by:

$$\Psi(\zeta \geq 0) = f(x) = \begin{cases} -\beta\zeta, & 0 < \zeta \leq 1 \\ -\beta \ln(\zeta) - \beta, & \zeta > 1 \end{cases} \quad (3.9)$$

### 3.4.2. Data Analysis

The observational LiDAR measurement data collected from Hollanse Kust (Zuid) wind farm are used to validate the stability correction functions presented previously. The dimensionless stability parameter  $\zeta$  is calculated based on the Bulk-Richardson method as presented in section 3.3.1. Following Holtslag et al. (2014), the wind shear profile will be represented by the ratio between wind speeds at two different heights, and will be expressed as a function of  $\zeta$ . Moreover, the surface roughness  $z_0$  assumed to be 0.0002 for offshore condition(NREL, 2021)s.

To assess the precision of the stability correction functions, four distinct cases will be examined. For each case, the wind shear profile is represented by the ratio between wind speed at two different heights as presented in Table 3. The main objective of this analysis is to determine the best method to extrapolate wind speeds from a lower height to a higher altitude. This is of particular importance in wind energy field as the size of large of large capacity wind turbines could extend beyond the LiDAR measurements, necessitating accurate extrapolation.

Table 3: Representation of wind shear profiles for four different cases

Case #	Wind shear profile
1	$U_{200}/U_{30}$
2	$U_{160}/U_{30}$
3	$U_{200}/U_{100}$
4	$U_{160}/U_{100}$

The initial two cases are dedicated to assessing the performance of extrapolation techniques when wind speeds need to be projected from a relatively low altitude, (e.g. 30 meters) to a much higher altitude. The first case will consider a wind shear profile represented by the ratio of wind speed at 200 meters height to that at 30 meters height. In the second case, the effectiveness of the extrapolation method used in the first case is put to the test. Here, the wind shear profile is represented by the ratio of wind speeds measured at 160 meters and 30 meters. The primary aim of this case is to determine whether the extrapolation method can adapt and remain reliable when the difference in height changes.

The third and fourth cases shift the extrapolation starting point to an intermediate altitude, here defined as 100 meters. This new starting point provides an opportunity to examine the extrapolation methods under different scenarios. In the third case scenario, the wind shear profile is determined by the ratio of wind speed measured at 200 meters to that at 100 meters. Finally, the fourth is developed to validate the extrapolation method used in the third case over varying altitude spans. Here, the focus is on the ratio of wind speeds at 160 meters to 100 meters. This case seeks to understand whether the extrapolation method used in the third case remains robust and effective when applied to different height variations.

The stability classifications based on the value of  $\zeta$  are outlined in Table 4, following the classification of Gryning et al. (2007).

Table 4: Stability classes as a function of the dimensionless stability parameter  $\zeta$

Stability Class	Range of $\zeta$
<b>Very Unstable (VS)</b>	$\zeta < -1$
<b>Unstable (U)</b>	$-1 < \zeta < -0.4$
<b>Neutral (N)</b>	$-0.4 < \zeta < 0.4$
<b>Stable (S)</b>	$0.4 < \zeta < 1$
<b>Very Stable (VS)</b>	$\zeta > 1$

Figure 10 showcases the performance of the extrapolation techniques when wind speeds need to be projected from a relatively low altitude (30 meters) to a much higher altitude. It is found during very unstable atmospheric conditions ( $\zeta < -1$ ), the stability corrected logarithmic law using both Businger-Dyer and the free convection stability correction functions perform relatively well in predicting the mean shear profile. The differences between the two correction functions are small. On the other hand, both the power law and logarithmic law overestimated the shear profile, with the power law being most inaccurate.

For unstable conditions ( $-1 < \zeta < -0.4$ ), the observed mean shear profile falls between the logarithmic law and the stability corrected logarithmic law. The logarithmic law is found to be the most accurate at  $-0.6 < \zeta < -0.4$ , whereas the stability corrected logarithmic law is found to be the most accurate at  $-1 < \zeta < -0.6$ . For neutral conditions where  $-0.4 < \zeta < 0$ , the logarithmic shear profile tends to underestimate wind shear, whereas the power law overestimates wind shear. The stability corrected logarithmic law showed the worst performance.

In case of a positive  $\zeta$ , the stability corrected logarithmic law performs relatively well during neutral atmospheric conditions ( $0 < \zeta < 0.4$ ). However, during stable and very stable atmospheric conditions, they perform the worst. A potential cause of this is the reduced thickness in the surface layer during stable atmospheric conditions as explained by Holtslag (2016).

During stable and very stable atmospheric conditions, the power law was found to be relatively accurate when extrapolating the wind speed from 30 meters height to 200. However, when extrapolating from 30 meters height to 160 meters, the accuracy of the power law is decreased. Interestingly, the mean wind shear profile remained relatively similar for those two cases with an average value of 1.3.

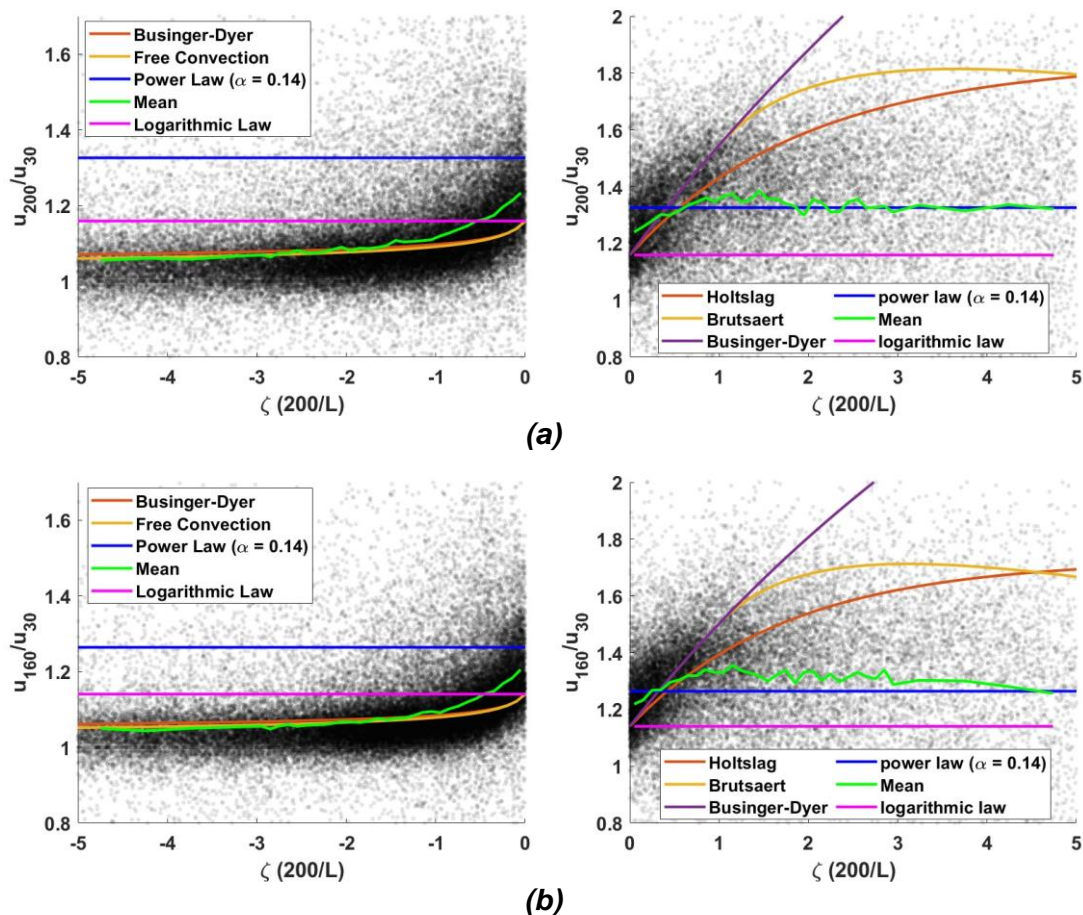


Figure 10: Observed and theoretical wind shear as a function of the dimensionless stability parameter. The wind shear profile is represented by the ratio of velocities ( $U$ ) measured at two heights, (a)  $U_{200}/U_{30}$  and (b)  $U_{160}/U_{30}$ .

On the other hand, in Figure 11, the starting point for extrapolation shifts from a low altitude to an intermediate altitude of 100 meters. The results are almost identical to those discussed earlier, except for the wind shear profile represented by stable and very stable atmospheric conditions. During stable conditions ( $0.4 < \zeta < 1$ ), the wind shear profile is best represented using the power law. However, during extreme stability cases, the logarithmic law showed to provide the best results.

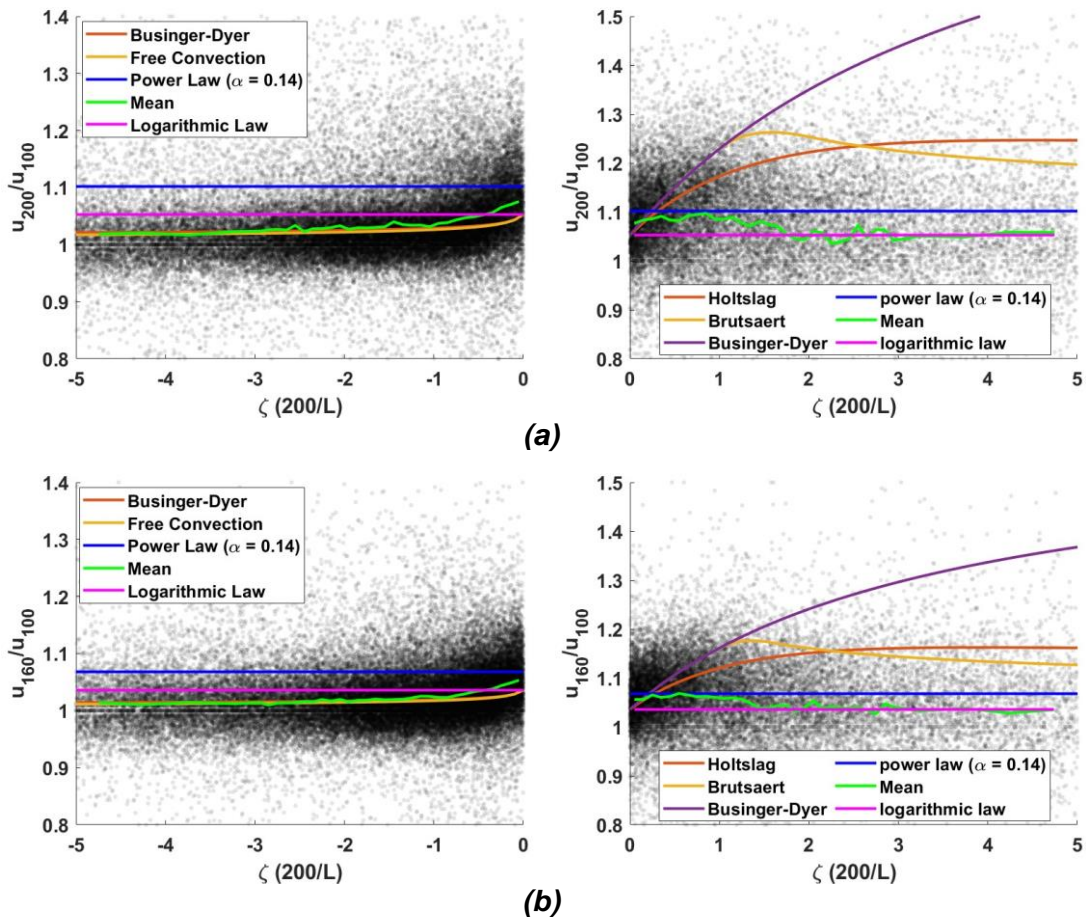


Figure 11: Observed and theoretical wind shear as a function of the dimensionless stability parameter. The wind shear profile is represented by the ratio of velocities ( $U$ ) measured at two heights, (a)  $U_{200}/U_{100}$  and (b)  $U_{160}/U_{100}$

The results reveal that the performance of each extrapolation model is significantly influenced by atmospheric conditions. In general, the free convection and Businger-Dyer stability correction functions worked relatively well during unstable atmospheric conditions. However, during stable conditions, there is a varying degree of accuracy of each model dependent on the starting point of the extrapolation process. This suggests the need for a comprehensive model capable of accurately representing the wind shear profile beyond the confines of the surface boundary layer.

# Chapter 4. Simulation Tools

This chapter provides an overview of the aeroelastic model utilized in this research. First, the working principle of the aeroelastic model will be explained. Next, the specifications of the reference wind turbine used in this study will be discussed. The potential limitations of the aeroelastic tool will also be addressed. Lastly, an overview of the simulation conditions used in this study will be presented.

## 4.1. The Aeroelastic Model

To investigate the influence of wind shear and turbulence intensity on the loads and performance of wind turbines, OpenFAST software is used (NREL, 2021). OpenFAST is an open-source computer-aided engineering software package developed by the National Renewable Energy Laboratory (NREL) for simulating the aerodynamics, structural dynamics, and control systems of wind turbines. It is a comprehensive software tool for designing and analyzing wind turbines. OpenFAST is designed to be highly modular and customizable, allowing users to easily configure and modify the software to meet their specific needs. The software can be used to simulate both onshore and offshore wind turbines, and it includes advanced features for modeling the complex aerodynamic and structural behavior of wind turbine components such as blades, towers, and control systems.

The working principle of OpenFAST is demonstrated in Figure 12. The software includes several modules such as AeroDyn, ElastoDyn, ServoDyn, SubDyn and others that work simultaneously to simulate the behavior of wind turbines.

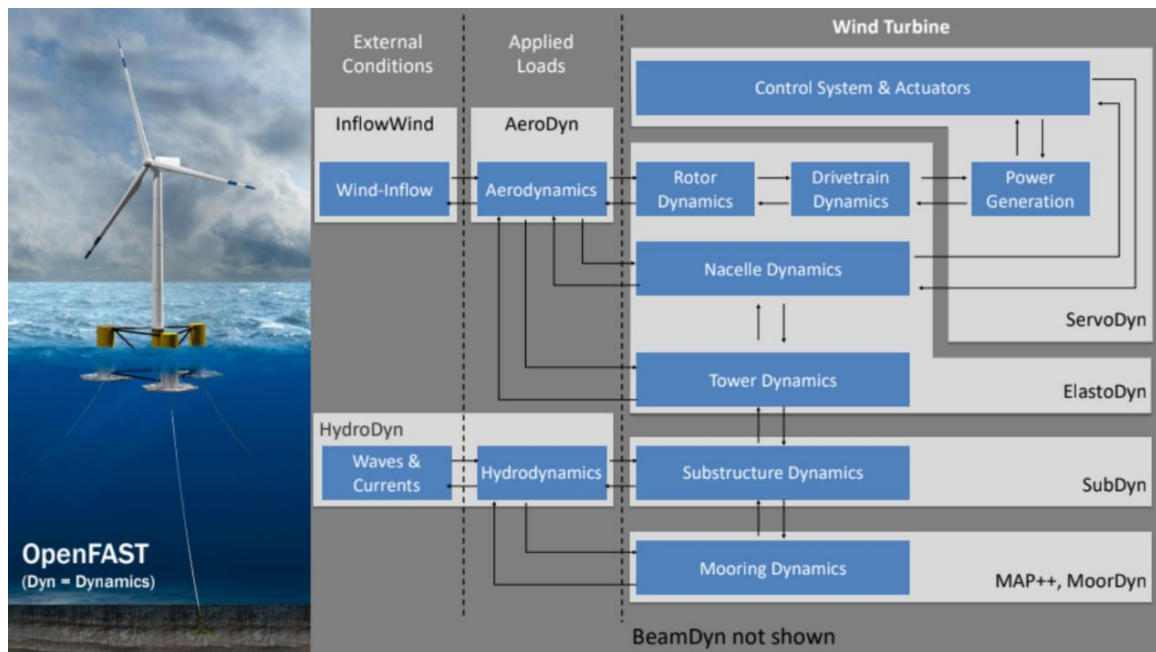


Figure 12: Working principle of OpenFAST (NREL, 2021)

### **4.1.1. AeroDyn**

The AeroDyn module (NREL, 2021) simulates the aerodynamic forces acting on the turbine blades. It models the unsteady flow around the blades and calculates the lift and drag forces, as well as the torque generated by the rotor. AeroDyn considers several factors, such as the wind speed, turbulence intensity, blade geometry, and rotational speed, to accurately model the aerodynamic behavior of the turbine using the blade element momentum theory (BEM).

Blade Element Momentum (BEM) theory is a model utilized to estimate the aerodynamic forces acting upon rotating blades. It integrates two methodologies: blade element theory and momentum theory. Blade element theory treats each segment of the blade as an individual airfoil that produces lift and drag due to local wind conditions. Momentum theory, views the turbine's rotor as a disc that decelerates the incoming wind to harness energy, determining the rotor's thrust and the power extracted from the wind based on the air's momentum change. The BEM theory combines these approaches in an iterative process to calculate the aerodynamic forces and power performance of a wind turbine

### **4.1.2. ElastoDyn**

ElastoDyn (NREL, 2021) models the structural dynamics of wind turbine blades, including their flexibility and deformation in response to aerodynamic loads and other external forces. This module considers several factors, such as the mass and the stiffness of the tower and blades, to accurately simulate the structural response of the turbine.

### **4.1.3. ServoDyn**

ServoDyn (NREL, 2021) models the behavior of the turbine's control system. It simulates the interactions between the control system and the mechanical and aerodynamic components of the turbine. This module receives information from the AeroDyn and ElastoDyn modules and uses it to calculate the forces and moments acting on the turbine. It then sends signals to the turbine controller to adjust the pitch angle of the blades, the rotor speed, and other parameters to maintain the desired power output and operational conditions.

### **4.1.4. SubDyn**

The SubDyn (NREL, 2021) module simulates the dynamic behavior of the wind turbine substructure including the tower, foundation, and monopile. This module considers several factors such as mass properties, material properties, and geometry of the wind turbine substructure. For the purpose of this research, a fixed-bottom monopile support structure is assumed.

### 4.1.5. Inflow Conditions

OpenFAST allow users to generate the inflow conditions through different formats including uniform wind file, steady wind conditions, TurbSim full-field (NREL et al., 2021), and others. When using the steady wind conditions format, one can specify the power law exponent parameter and wind speed at a reference height, however, a turbulent field cannot be generated. TurbSim (NREL et al., 2021) on the other hand can be used to generate time series of synthetic turbulent wind fields. The user is able to define which spectral techniques to used (e.g. Kaimal) and can prescribe the statistical properties that match those of the measured wind data.

## 4.2. Reference Turbine

The IEA 15-Megawatt offshore wind turbine with a fixed-bottom monopile support structure (Gaertner et al., 2022) is used throughout this research. The conceptual design was done as a part of a joint effort between the National Renewable Energy Laboratory (NREL) and the Technical University of Denmark (DTU). The design was sponsored by the European Union’s H2020 program through the International Energy Agency (IEA) work package. The wind turbine belongs to Class IB direct-drive turbine and has a rotor diameter of 240m and a hub height of 150m. An overview of the key parameters and turbine layout are presented in Table 5 and Figure 13 respectively. The NREL opensource controller (ROSCO) (Nikhar J. Abbas et al., 2021) is adopted in this design. To prevent 3-period interference with the natural frequency of the tower/monopile, the rotor runs at a minimum speed of 5 rpm in control region 1.5, starting from the cut-in wind speed (3 m/s) up to 7 m/s. In control region 2, below the rated wind speed (10.59 m/s), the rotor operates in according to the turbine’s optimal tip speed ratio (TSR). When the wind speed reaches the rated wind speed (10.59 m/s), the rotor rotates at a rated speed of 7.55 rpm, which gives it a maximum tip speed of 95 m/s. Above the rated wind speed, the blade pitch angle is set by the controller to maintain the turbine’s rated power.

Table 5: Key parameters for IEA 15-MW reference turbine (Gaertner et al., 2022)

Parameter	Value
Power rating	15 MW
Turbine class	IEC Class 1B
Control	Variable speed, collective pitch
Cut-in wind speed	3 m/s
Rated wind speed	10.59 m/s
Cut-out wind speed	25 m/s
Design tip-speed ratio	9
Min/max rotor speed	5.0 / 7.56 rpm
Rotor diameter	240 m
Hub height	150 m
Drivetrain	Direct drive

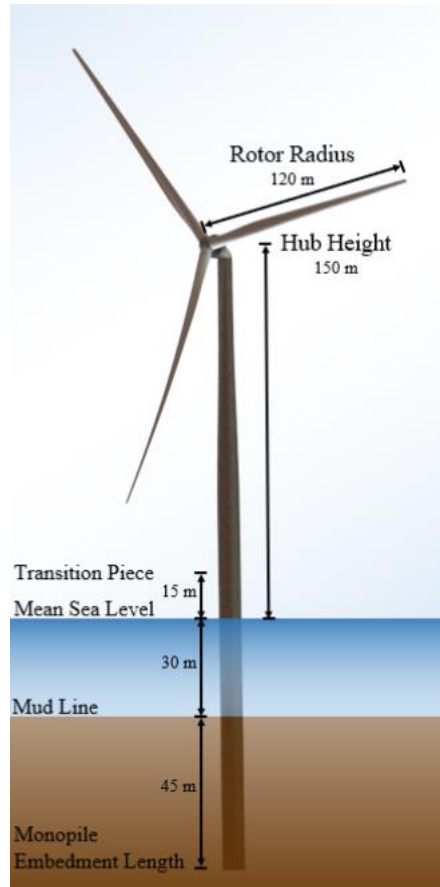


Figure 13: Overview of wind turbine layout (Gaertner et al., 2022)

Note that when generating a wind field for the IEA 15-MW reference turbine using TurbSim (NREL et al., 2021), the grid height and width should be greater than the rotor diameter plus the shaft length (NREL et al., 2021). In this research, both the grid height and width are chosen to be 260 meters to satisfy this requirement. Moreover, the IEC design standards (IEC, 2005, 2009) specify a requirement that the maximum distance between the grid cells should be smaller than 25% of  $\Lambda_1$  (refer to Eq. (2.17)) and no longer than 15% of the rotor diameters. Therefore, the number of grids adopted in this research in both the vertical and horizontal dimensions is chosen to be 23x23 to satisfy the standard requirements.

### 4.3. Limitations

As elaborated by Moriarty and Hansen (2005), there are several limitation when considering the use of BEM theory in AeroDyn module. One of the limitations is that it assumes a quasi-steady state condition, which may not be valid for all wind turbine operating conditions. For example, during transient events such as gusts, the aerodynamic forces acting on the blades can change rapidly, and BEM may not capture these effects accurately. This can lead to errors in the prediction of wind turbine performance and loads. Another limitation is its inability to model complex three-dimensional flow phenomena, such as blade tip vortices and wake turbulence which can significantly affect the performance of downstream wind turbines. Moreover, BEM models typically assume a simplified two-dimensional flow field and neglect the

effect of curvature. This decreases the accuracy when the blades experience significant out of plane deflection. However, despite these limitations, BEM theory remains a valuable and widely used method for calculating the induced velocity and elemental forces on wind turbine blades (Moriarty & Hansen, 2005).

## 4.4. Simulation Cases

To gain a better understanding on the influence of wind shear and turbulence intensity on the loads and performance of wind turbines, simulations of the IEA 15-MW reference turbine are carried out using OpenFAST, covering wind speeds ranging from 5 to 25 m/s with a 1 m/s interval. Two distinct cases will be considered, which are designed to individually investigate the impacts of wind shear and turbulence intensity as independent variables. An overview of the simulation cases is presented in Table 6.

The first case is set to analyze the effects of wind shear on the loads and performance of wind turbines absence of turbulence. A total of 315 simulations are conducted, covering 21 wind speed bins and 15 distinct power law exponent values ranging between -0.2 and 0.5. Each simulation lasts for 10 minutes, with an additional 100 seconds representing transient conditions.

The second case is set to analyze the effects of turbulence intensity on the loads and performance of wind turbines absence of wind shear. A total of 189 simulations are conducted, covering 21 wind speed bins and 9 distinct turbulence intensity values ranging between 0 to 0.5, increasing by 0.05 increments. Each simulation lasts for 1-hour, with an additional 100 seconds representing transient conditions, to meet the requirement of at least 6 turbulent seeds as per IEC guidelines (IEC, 2005).

Table 6: Overview of simulation cases

Case #	TI range	PLE range	Speed bins	Simulation time	Nr. Of simulations
Case 1	0	-0.2 to 0.5	21	10-min	21x15 = 315
Case 2	0 to 0.5	0	21	1-hr	21x9 = 189

In **Chapter 5**, the results derived from these two cases will be used to identify the effects of TI and PLE on the fatigue damage encountered at the blade root of a wind turbine. In **Chapter 6**, the results of the simulations will be used to identify the effects of TI and PLE on the performance and power output of a wind turbine.

# Chapter 5.

## Fatigue Load Analysis in Relation to Atmospheric Conditions

The design and certification of wind turbines typically rely on a standardized set of reference wind climate parameters, such as those outlined in IEC-61400 design standards (IEC, 2005, 2009). Consequently, wind turbines can be mass-produced within predetermined classes, facilitating their widespread deployment (Toft et al., 2016). Nevertheless, it is necessary to prove that the atmospheric conditions at a specific site are not more severe than those considered during the wind turbine design process. If the actual conditions are more severe, it is mandatory to assess the structural integrity through load calculations (IEC, 2005). However, conducting these calculations involves a large number of simulations, which are both time-consuming and expensive (Toft et al., 2016).

This chapter therefore investigates whether it is possible to improve the accuracy of a site-specific fatigue load assessments, and whether it can be done with computational efficiency, despite the increased complexity.

### 5.1. Introduction

According to IEC-61400 (2005, 2009), the assessment of structural integrity can be conducted by comparing the site-specific wind data with the reference wind climate parameters. This comparison aims to demonstrate that the local wind conditions are less severe than those defined in the design parameters. While this approach suffices in cases where all wind climate parameters fall within their respective design limits, there are instances where one or more parameters exceed their design values. This situation often arises due to natural variations in wind climate parameters (Toft et al., 2016).

To illustrate this, consider the example of the IEA 15-MW reference turbine, which falls under the Class IB category with  $V_{ref}$  equal to 50 m/s (IEC, 2005). To ensure it is suitable to be deployed at Hollandse Kust (Zuid) wind farm location, it is necessary to confirm that the 90% quantile of turbulence at the site location, measured between  $0.2 V_{ref}$  and  $0.4 V_{ref}$ , remains below the design limit set for Class IB wind turbines (IEC, 2005, 2009). However, when examining the turbulence intensity levels at the site location, it becomes evident, as shown in Figure 14, that the 90% quantile turbulence exceeds the design values for wind speed bins greater than 18 m/s. In such cases, it becomes mandatory to confirm the structural integrity through load calculations (IEC, 2005, 2009). These calculations involve estimating the wind turbine loads using aero-elastic simulations that incorporate the site-specific wind climate parameters. However, performing a significant number of these simulations is both time-consuming and

expensive (Toft et al., 2016). For instance, simulating fatigue damage using actual 10-minute wind measurements requires approximately 52,600 simulations for an entire year, considering only one turbulence seed. Therefore, alternative methods are needed to estimate wind turbine loads efficiently and accurately.

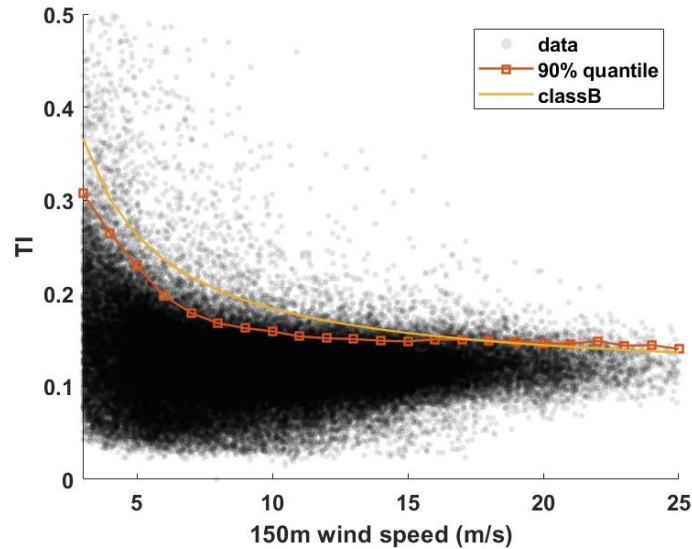


Figure 14: 90% quantile turbulence intensity levels at Hollandse Kust (Zuid) wind farm (red), and the design turbulence intensity level of classB wind turbines (yellow)

In order to quickly assess the site specific wind turbine loads, Toft et al. (2016) proposed to use the response surface methodology (RSM) based on pre-run aero-elastic simulations. Two approaches have been taken to establish a response surface. First, using Taylor's approximation, and second, using a central composite design.

The Taylor approximation is based on the assumption that there is no interaction between the climate parameters and that the loads response surface can be obtained by a first order Taylor-series (Toft et al., 2016). On the other hand, the central composite design (Montgomery, 2013) is based on a second order response which should capture the interaction between the climate parameters. Overall, the central composite design was found more accurate for fatigue load assessment (Toft et al., 2016).

The central composite design (CCD) was initially introduced by Box and Wilson (1951) to estimate the second-order effects in a response. These second order effects are often observed when considering the interactions between turbulence and wind shear (Toft et al., 2016). The CCD uses different combinations between variables in a circular (refer to Figure 15) or spherical design in order to establish a response to a system. The overall number variable combination used is  $n = 2^k + 2k + n_0$ , where  $k$  represents the number of variables being considered, and  $n_0$  is the center point as shown in Figure 15. The distance between the center point and the surrounding points is a function of  $\gamma = 2^{k/4}$  following Montgomery (2013).

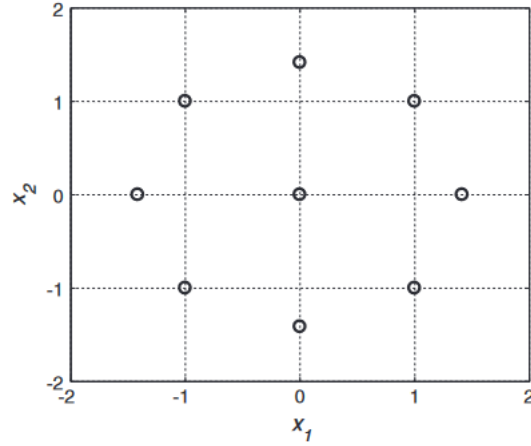


Figure 15: Variation of two variable in central composite design,  $\gamma = \sqrt{2}$  (Toft et al., 2016)

To establish a response in terms of fatigue load analysis, Toft et al. (2016) proposed to use the following linear regression model with an interaction term

$$f(x) = \beta_0 + \sum_{i=1}^k \beta_i X_i + \sum_{i=1}^k \sum_{j \geq 1}^k \beta_{ij} X_i X_j + \varepsilon \quad (5.1)$$

Where  $\beta$  is the regression parameter,  $X$  is a matrix containing the variables, and  $\varepsilon$  is the residual which is assumed to be unbiased normally distributed following Toft et al. (2016). Note that the residual is the error between a predicted value and the actual value. Assuming an unbiased normal distribution of the residuals means that all residuals will eventually cancel out.

For the purpose clarity, Eq. (5.1) can be expressed as:

$$\begin{aligned} f(x) = & \beta_0 + \beta_1 X_1 + \beta_2 X_2 + \beta_3 X_3 + \dots && \text{(linear term)} \\ & + \beta_{12} X_1 X_2 + \beta_{13} X_1 X_3 + \beta_{23} X_2 X_3 \dots && \text{(interaction term)} \\ & + \varepsilon && \text{(residual)} \end{aligned} \quad (5.2)$$

From Eq. (5.2), one can notice that the regression model consists of a linear term and an interaction term. This implies that there should a linear relationship between turbulence and fatigue loads if the effects of wind shear are neglected. Similarly, there should be a linear dependency between wind shear and fatigue loads when the effects of turbulence are not accounted for. While it is true, to some extent, that there exists a linear dependency between turbulence and fatigue loads (Veldkamp, 2007), the relationship between wind shear and fatigue loads is slightly more complex. From Slot et al. (2018), it was noticed that the relation between wind shear and fatigue loads can be divided into two regions. Generally, for PLE values above 0.1, a linear relationship between fatigue loads and wind shear becomes apparent. However, at the lower range of the PLE, there exists a region where non-linearity occurs. The same observation was also found in a later analysis as shown in Figure 17 (b).

Based on this observation, this study will propose a new approach to incorporate the non-linear region to the response function of fatigue loads. This proposal will adopt the response surface method using the central composite design in two distinct regions. The first region considers a quadratic relation between wind shear and fatigue loads

in the region where non-linearity occurs, and the second region is the linear region. Accordingly, a quadratic response surface model will be adopted for the first region (see Eq. (5.3)), and the linear regression model expressed in Eq. (5.2) will be used in the second region.

The regression model which accounts for the quadratic response can be expressed as

$$f(x) = \beta_0 + \sum_{i=1}^k \beta_i X_i + \sum_{i=1}^k \sum_{j \geq 1}^k \beta_{ij} X_i X_j + \sum_{i=1}^k \beta_{ii} X_i^2 + \epsilon \quad (5.3)$$

Or could also be expressed as

$$\begin{aligned} (x) = & \beta_0 + \beta_1 X_1 + \beta_2 X_2 + \beta_3 X_3 + \dots && (\text{linear term}) \\ & + \beta_{12} X_1 X_2 + \beta_{13} X_1 X_3 + \beta_{23} X_2 X_3 \dots && (\text{interaction term}) \\ & + \beta_{11} X_1 + \beta_{22} X_2 + \beta_{33} X_3 \dots && (\text{quadratic term}) \\ & + \epsilon && (\text{residual}) \end{aligned} \quad (5.4)$$

## 5.2. Methodology

This section is subdivided into several parts. First, the state-of-the-art method for calculating fatigue loads using Miner's rule (IEC, 2005) will be addressed. Next, statistical data obtained from the Hollandse Kust (Zuid) wind farm will be used to create a simplified artificial site. The purpose of creating this simplified artificial site is to reduce the number of simulations required to assess the accuracy of each fatigue assessment model. Lastly, the methodology employed for fatigue load assessment using the response surface method will be explained.

### 5.2.1. Fatigue Load Calculations

The central principle of fatigue analysis, known as Miner's rule (IEC, 2005), suggests that the state of limit, which predicts possible failure due to fatigue, is reached when the cumulative damage equals or surpasses one. Therefore, it is crucial to ensure that the total accumulated damage throughout the turbine's lifecycle remains below this threshold.

The focus of this thesis is on computing the fatigue damage borne by the wind turbine's blades, with the blade root being of particular interest due to the maximal stresses and moments it endures (Teixeira et al., 2017). Using OpenFast, simulations of the IEA 15-MW reference turbine are performed in accordance to the parameters stated in the section 4.4. The bending moments outputs of the simulations are used to determine the stresses on the root of the wind turbine blade as follows:

$$\sigma = \frac{M * R}{I} \quad (5.5)$$

Where,

- M            Bending moment
- R            Radius at the blade root
- I            Moment of inertia

The Moment of inertia  $I$  is defined as

$$I = \frac{K}{E} \quad (5.6)$$

Where,

- K            Blade root stiffness equal to 138 GN.m<sup>2</sup> (Gaertner et al., 2022)
- E            Young's module of elasticity, estimated to 56 GPa (Hu et al., 2012).

The Rainflow counting algorithm developed by Greaves (2023) along with equations (2.18) to(2.20) 2.22), as described in Chapter 2.5, are used to estimate the lifetime fatigue damage and damage equivalent loads. Since the IEC 15-MW offshore turbine is a hypothetical reference turbine, there are no S-N curves available to obtain the Wohler exponent  $m$ . Typical values of the Wöhler exponent for wind turbine blades can range from 8 to 12 (Veldkamp, 2007). Therefore, the slope  $m$  is assumed to be 9 and the UCS for the blade roots is assumed to be 600 MPa (Mallick, 2008).

### 5.2.2. Artificial Site Development

Since it is very difficult to simulate every combination of TI and shear based on actual site measurements, a simplified artificial site will be created to reduce the number of simulations required to assess the accuracy of each fatigue assessment model.

Considering the atmospheric conditions at Hollandse Kust (Zuid), a total of 50 different combinations of PLE & TI values are selected for each wind speed bin that surpasses the design limits of the Class IB 15-MW reference turbine. Only wind speed bins ranging from 0.2  $V_{ref}$  to 0.4  $V_{ref}$  are considered following IEC-61400-1-ed.3 (IEC, 2005), where  $V_{ref} = 50$  m/s is the reference velocity specified for Class 1 wind turbines. An overview of the wind speed bins in Hollandse Kust (Zuid) exceeding the design limit of the Class IB reference turbine is presented in Table 7.

*Table 7: Overview of atmospheric conditions f Hollandse Kust (Zuid) that exceed the design limits of the IEA 15-MW reference turbine*

Speed bin	TI design limit	90% quantile of TI
18 m/s	14.86%	14.96
19 m/s	14.63%	14.85
20 m/s	14.42%	14.63

The TI and PLE values are randomly generated assuming a normal distribution, with the mean and the standard deviation estimated based on actual site measurements as presented in Table 8. The TI values will be arranged in ascending order and the PLE values will be arranged in descending order in order to mimic real-life situations (e.g. high TI values are often associated with low PLE values and vice versa). Although this is an idealized scenario and may not be representative of real-

life conditions, it does provide a way to evaluate the accuracy of the propose fatigue analysis methods.

Table 8: Overview of mean values and standard deviations of turbulence intensity and power law exponent at Hollanse Kust (Zuid) wind farm

Speed bin	Mean TI	std TI	Mean PLE	std PLE
18 m/s	12.31%	0.0206	0.1127	0.0763
19 m/s	12.30%	0.0199	0.1217	0.0780
20 m/s	12.10%	0.0198	0.1279	0.0752

### 5.2.3. Response Surface Methodology

Two RSMs will be assessed for the purpose of fatigue load assessment. First, using the central composite design as proposed by Toft et al. (2016), and second, using a modified version of the central composite design in order to capture the non-linearity region between fatigue loads and the wind shear exponent. Only two variables are considered; wind shear exponent and turbulence intensity.

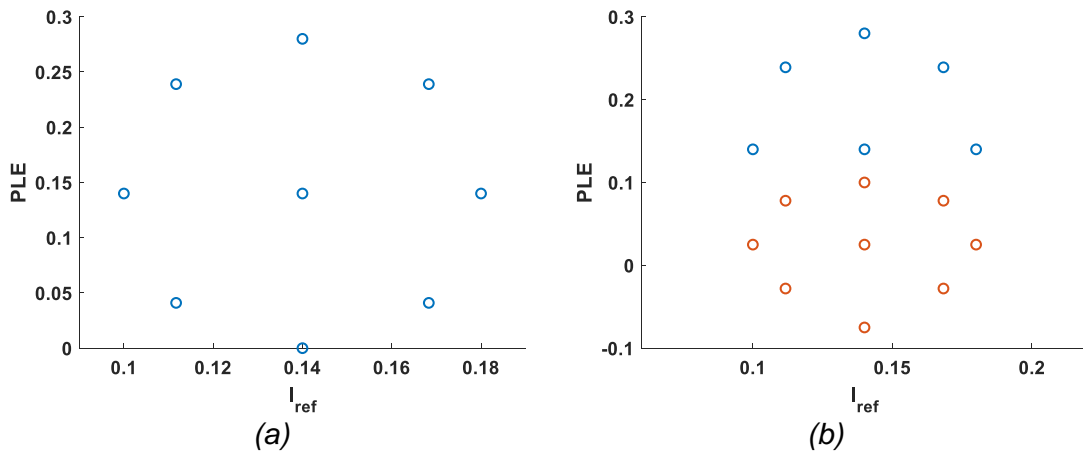


Figure 16: Variations of variables in central composite design (a), and variation of variables in the modified central composite design (b)

The variations between the wind climate variables (TI and PLE) for the central composite design are shown in Figure 16 (a) (Toft et al., 2016). They are derived based on the wind climate parameters listed in Table 9. The wind climate parameter correspond on average to IEC 61400-1 wind turbine Class IB (IEC, 2005, 2009), which is the design class of the IEA 15-MW reference turbine (Gaertner et al., 2022). The upper and lower limits have been selected to reflect typical site conditions for offshore wind farms (Toft et al., 2016).

In Figure 16 (a), corresponding to the central composite designed proposed by Toft et al. (2016), the distance from the center point (represented by the mean values) to the surrounding points is normalized by a factor of  $\gamma = 2^{k/4} = \sqrt{2}$  (Montgomery, 2013). The response surface function for this design will follow a linear regression with an interaction term as expressed in Eq. (5.1) (Toft et al., 2016). The regression parameter  $\beta$  can be estimated using `rstool` in Matlab.

Note that  $I_{ref}$  in Table 9 and Figure 16 correspond to the expected value of the turbulence intensity at 15 m/s, which equals to 0.14 for Class B wind turbines (IEC, 2005). The turbulence intensity for each wind speed follows (IEC, 2005):

$$TI = I_{ref} \left( 0.75 + \frac{5.6}{V_{hub}} \right) \quad (5.7)$$

Table 9: Wind climate parameters used for the central composite design and the upper range of the modified central composite design

Climate parameter	Mean	Lower limit	Upper limit
Turbulence Intensity ( $I_{ref}$ )	0.14	0.1	0.18
Power law exponent ( $\alpha$ )	0.14	0	0.28

The second response surface methodology proposed in this study adopts the modified central composite design as demonstrated in Figure 16 (b). The concept behind this method is to apply the central composite design in two regions. The first region considers a quadratic relation between wind shear and fatigue loads. It is assumed that this region occurs at PLE values below 0.1 for wind speed bins of 18, 19 and 20 m/s based on the analysis of Figure 17 (presented later in this chapter). Subsequently, the second region encapsulates the linear relation between wind shear and fatigue loads for PLE values above 0.1.

The climate parameters for the first region (PLE<0.1) and second region (PLE>0.1) are listed in Table 10 and Table 9 respectively. The response surface function for the first region (PLE<0.1) follows a quadratic response with an interaction term as expressed in Eq. (5.3), whereas, the response surface function for the second region (PLE>0.1) follows a linear regression with an interaction term as expressed in Eq. (5.1).

Table 10: Wind climate parameters used for the lower range of the modified central composite design

Climate parameter	Mean	Lower limit	Upper limit
Turbulence Intensity ( $I_{ref}$ )	0.14	0.1	0.18
Power law exponent ( $\alpha$ )	0.025	-0.075	0.1

## 5.2.4. Validation

Fatigue loads estimated using the response surface methodology will be validated against the fatigue loads calculated for each data point for the artificial site. First, a total of 50 1-hour simulations will be performed for each wind speed bin listed in Table 11. The damage equivalent load for each wind speed bin will then be calculated following the process of section 5.2.1. This forms the baseline for comparison.

Next, 9 one-hour simulations are performed for each data point of the central composite design, and 15 one-hour simulations for the modified central composite design. The response surface methodology is applied based on the calculated damage equivalent loads using *rstool* in Matlab in order to obtain the regression parameters  $\beta$ .

These response surface functions are then used to calculate the DEL for each data point of the artificial site. The cumulative DEL is calculated following

$$DEL = \left( \sum_{i=1}^n DEL_i^m \right)^{\frac{1}{m}} \quad (5.8)$$

The estimated fatigue loads using the response surface methodologies can then be validated against the baseline value.

Table 11: Overview of required simulations to validate the accuracy of the proposed response surface methods

Wind speed bin	No. of simulations		
	Artificial site	Central composite design	Modified central composite design
18 m/s	50	9	15
19 m/s	50	9	15
20 m/s	50	9	15

## 5.3. Results

This section will delve into the analysis of the effects of wind shear and turbulence intensity on the fatigue loads at a wind turbine blade root. The initial part focuses on the separate effects of these wind conditions on fatigue loads, followed by an investigation into their combined impact. Next, the validity of the surface response methodology using multiple design techniques will be tested against the hypothetical site. Lastly, these models will be contextualized within real-world conditions, specifically through their application to the site conditions found at the Hollandse Kust (Zuid) wind farm.

### 5.3.1. Fatigue Loads in Relation to Atmospheric Conditions

Understanding the impact of wind shear and turbulence on wind turbine loads is a complex process and is not yet fully understood. Various factors contribute to this complexity, including the wind turbine's control strategy, aerodynamics, and rotor inertia (Kovalnogov et al., 2022). Attempting to analytically resolve these effects can be challenging as a result of these complexities. Therefore, a qualitative approach will be adopted to analyze these effects using aeroelastic simulations as presented in Chapter 4.4.

#### *Fatigue Loads in Relation to Wind Shear*

Simulations of the IEA 15-MW reference turbine were executed using OpenFast, during which the PLE is varied for each wind speed bin ranging from 5-25 m/s in a 1 m/s interval (refer to Chapter 4.4). This allows for a focused investigation into the effect of wind shear on the fatigue loads of the wind turbine, by isolating it from other influencing factors such as turbulence. The primary focus is related to the fatigue loads that occurs at the blade root of a wind turbine in the flapwise direction. This is due to

the fact that the flapwise direction typically experiences the most significant loads (Teixeira et al., 2017).

From the results represented in Figure 17 (a), it is apparent that as wind speed increases, the Damage Equivalent Load (DEL) increases as well. This is likely due to the higher energy carried by the wind at higher speeds, which translates into larger forces exerted on the turbine blades. Figure 17 (b) provides an insight into how wind shear, represented by varying values of PLE, impacts fatigue loads at different wind speeds. An interesting pattern is noticed: a linear relationship between PLE and fatigue DEL is observed within a certain range of the PLE (e.g.  $PLE > 0.1$ ). However, there exists a region where non-linearity occurs. Instead, it exhibits more of a quadratic behavior. This is likely due to the aerodynamic forces acting on the blades overwhelm the effect of wind shear within that region. Overall, the results presented in Figure 17 are in good correspondence to findings of Slot et al. (2018)

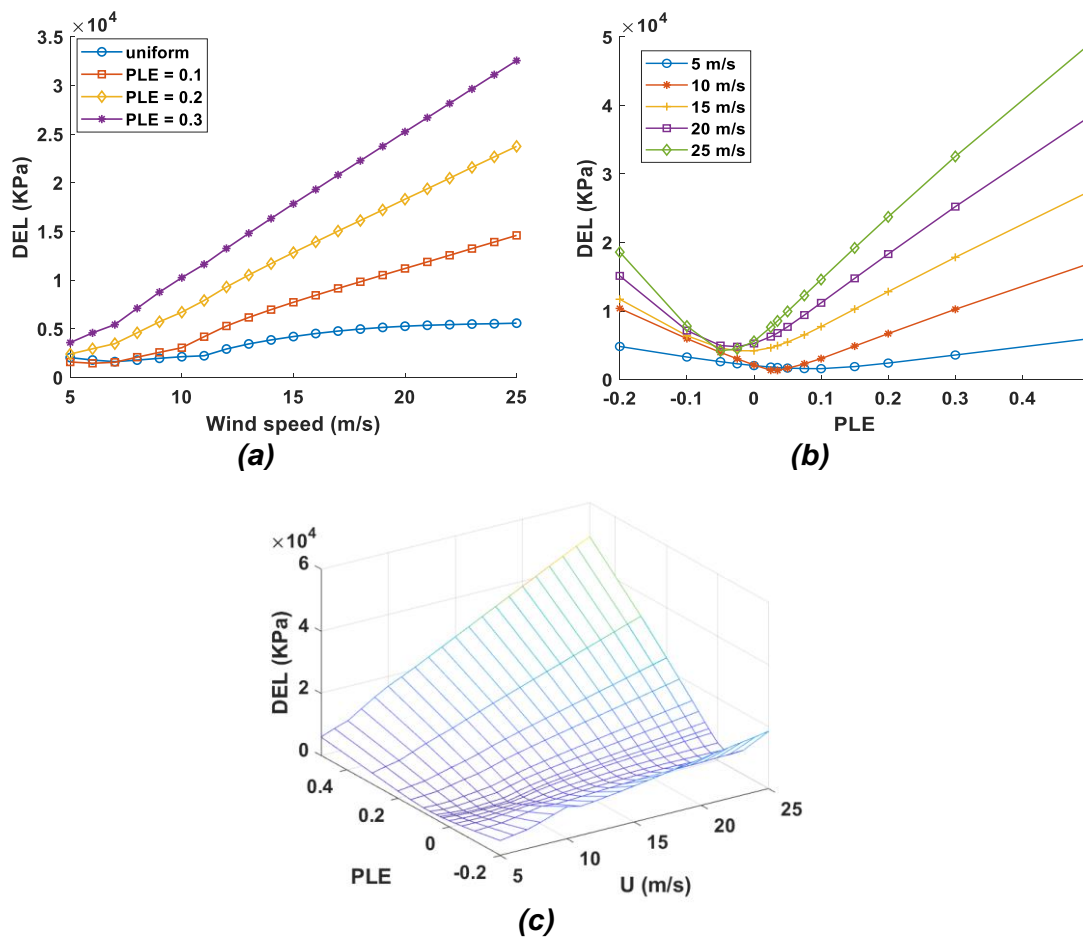


Figure 17: Blade root damage equivalent load (DEL) in the flapwise direction as a function of wind speed (a), blade root DEL in the flapwise direction as a function of power law exponent (b), and a 3D representation of blade root DEL in the flapwise direction as a function of wind speed and PLE (c)

### Fatigue Loads in Relation to Turbulence Intensity

A qualitative approach will be adopted to analyze the effects of turbulence on fatigue loads that occurs at the blade root of a wind turbine in the flapwise direction. The flapwise direction is again chosen since that it typically experiences the most significant loads (Teixeira et al., 2017).

Simulations of the IEA 15-MW reference turbine were executed using OpenFast, during which the turbulence intensity level is varied for each wind speed bin ranging from 5-25 m/s in a 1 m/s interval (refer to Chapter 4.4). This allows for a focused investigation into the effect of turbulence on the fatigue loads, by isolating it from other influencing factors such as wind shear.

From Figure 18 (a), it is apparent that the blade root DEL's response (flapwise direction) to changes in wind speed is nonlinear, and this becomes particularly evident when considering the impacts of turbulence. This observation is consistent with the research done by Slot et al. (2018). Moreover, the data displayed in Figure 18 (b) shows that there is roughly a linear correlation between turbulence and the blade root DEL (flapwise direction) when wind speed is held constant. There are a couple of instances where the correlation is not completely linear (e.g. at 25 m/s for TI values above 30%). However, this may be due to the limited number of turbulence seeds being considered. In this research, six turbulence seeds are executed for each wind speed bin and TI value, which is the minimum requirements of IEC standards (IEC, 2005, 2009). However, increasing the number of turbulence seeds is expected to increase the accuracy of the results. Overall, this linear correlation is in line with the research conducted by Veldkamp (2007).

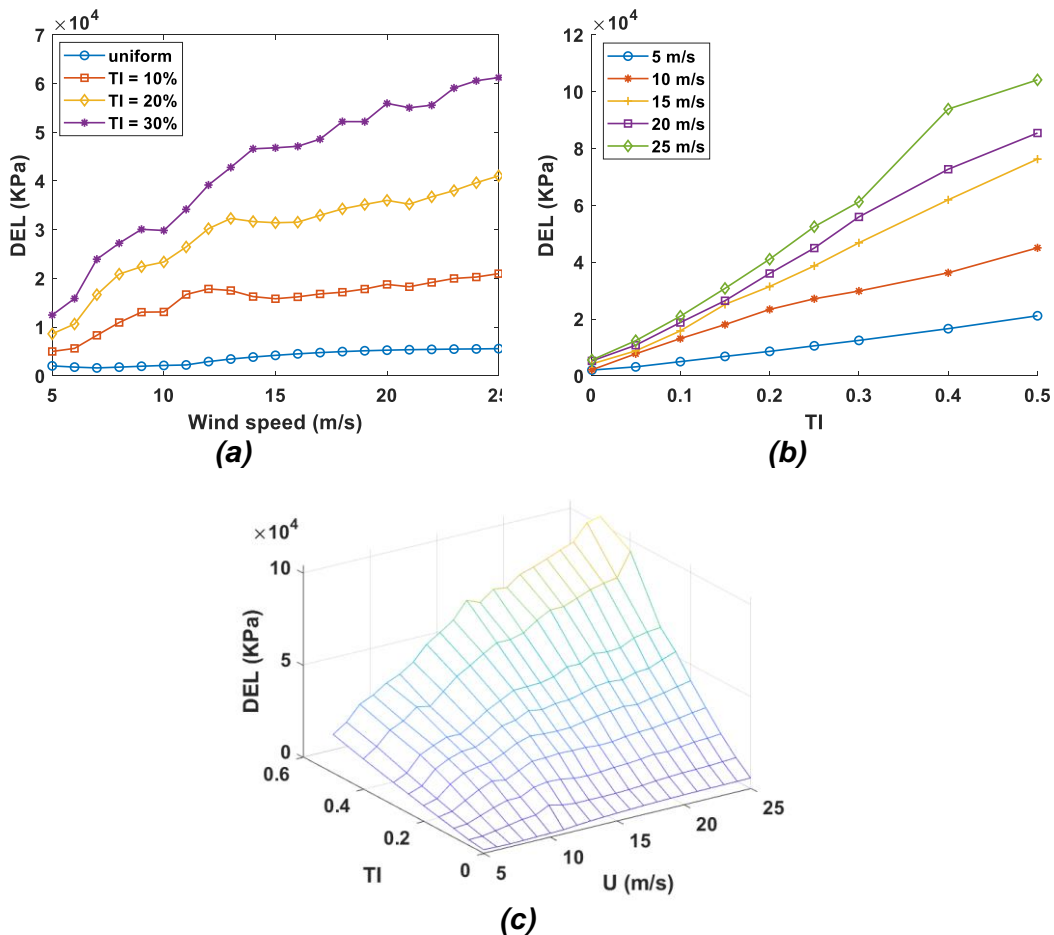


Figure 18: Blade root damage equivalent load (DEL) variations in the flapwise direction as a function of wind speed (a), Blade root DEL variation in the flapwise direction as a function of turbulence intensity (b), and a 3D representation of blade root DEL in the flapwise as a function of wind speed and turbulence intensity (c).

## Effects of Climate Parameter Interactions on Fatigue Load Assessment

The depicted relations between turbulence intensity and blade root DEL in the flapwise direction (see Figure 18) could be used to estimate a wind speed dependent equivalent turbulence intensity, which is an estimate of the exact turbulence level that would ideally produce the exact same loads as a full calculation would do. This could be done using a simple linear regression model using the least squares method. This method was adopted by Veldkamp (2007), and the results were deemed effective but conservative. Similarly, the same approach could also be employed to estimate an equivalent power law exponent. However, a potential drawback of this method is that it overlooks the interaction between wind shear and turbulence intensity.

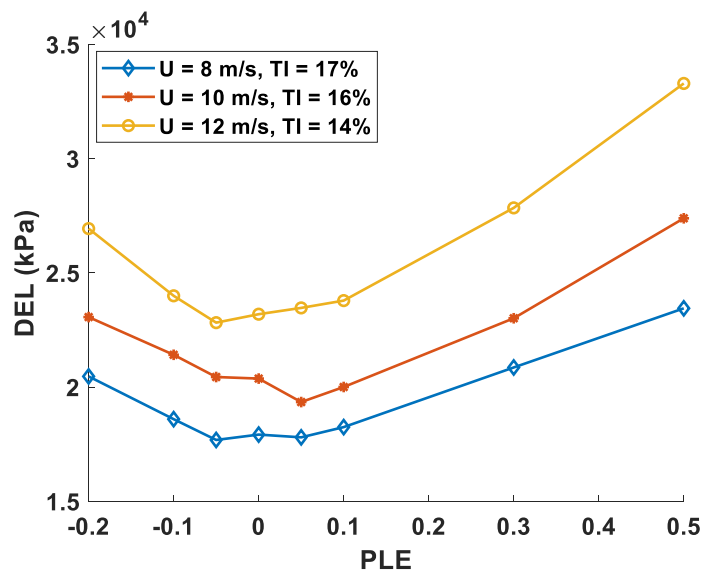


Figure 19: Interaction between turbulence intensity and power law exponent in relation to fatigue load assessment for wind turbines blade root in the flapwise direction

As Figure 19 shows, when the effects of turbulence are accounted for, an increase in the power law exponent value (either in the positive direction or negative direction) does not necessarily lead to an increase in fatigue loads. This indicates a complex relationship between the two variables, where the impact of one variable could amplify or diminish the effect of the other. For instance, higher wind shear might cause different parts of the rotor to experience different wind speeds, potentially increasing fatigue. But if this is combined with high turbulence, the rotor might continuously adapt to the changing wind, thereby reducing the influence of the wind shear. Thus, the interaction between wind shear and turbulence can create a complex effect on fatigue loads that is not simply a sum of the individual effects.

Given these observations, this research will one focus on the regression models which account for the interactions between the climate parameter (e.g. RSM using the central composite design).

### 5.3.2. Response Surface Methodology

The response surface methodology's (RSM) strength lies in its ability to account for the interactions among wind climate parameters (Toft et al., 2016). Within the scope of this research, three methods leveraging this capability are proposed:

1. Using an interactive linear regression of the central composite design (refer to Figure 16(a)) as proposed by Toft et al. (2016). Here, 9 simulations are required to establish a response based on different combinations between TI and PLE.
2. Utilizing an interactive quadratic regression for the non-linear region (highlighted in Figure 17(b)) and an interactive linear regression for the linear region, both within the modified central composite design depicted in Figure 16(b). It is assumed that the non-linear region occurs at PLE values below 0.1 based on the analysis of Figure 17(b). Here, 15 simulations are required to establish a response based on different combinations between TI and PLE.
3. Applying an interactive linear regression across the complete range of the modified central composite design depicted in Figure 16(b). Here, the same 15 simulations done in the second method are used to establish a response. This additional step is included in order to verify if any improvement of accuracy resulting from the second method is not just associated with the increase of number of simulated data (9 vs 15 simulations).

The proposed methods are first implemented on an artificial site, as detailed in section 5.2.2. This artificial site is a simplified model designed to reduce the number of simulations necessary to assess the accuracy of each fatigue assessment model. The estimated fatigue loads are then put to the test by comparing them against the cumulative fatigue loads calculated based on the actual data points within the artificial site. The purpose of this exercise is to validate the accuracy of the proposed fatigue load analysis methods.

Once the proposed models have been verified for accuracy using the artificial site, they will be applied to real-world conditions at the Hollanse Kust (Zuid) wind farm location. The goal of this application is to determine the feasibility of installing a Class IB wind turbine at this specific location.

As mentioned earlier, International Electrotechnical Commission standards (IEC, 2005, 2009) stipulate that the atmospheric conditions at a given site should be less severe than the wind climate parameters that were considered during the design of the turbine class. In terms of turbulence levels, the standards require that the 90% quantile of turbulence for wind speeds ranging from 10 to 20 m/s should not exceed the design value specified for a Class IB wind turbine (IEC, 2005, 2009). However, it has been observed that the 90% quantile of turbulence for wind speed bins of 18, 19, and 20 m/s at the Hollanse Kust (Zuid) wind farm exceed the design limit of a Class IB turbine (refer to Figure 14). Consequently, to ensure the structural integrity of the turbine, it is necessary to perform fatigue load calculations for these specific wind speed bins.

## Validation of Proposed Methodologies

Table 12 showcases the estimated damage equivalent loads for the three proposed methods along with the cumulative DEL, derived from the fatigue load calculations conducted for each data point within the artificial site. An analysis of the results shows that both the central composite design using an interactive linear regression and the modified central composite design featuring a quadratic region performed very well, with a maximum error rate of just 0.72%. In the 18 m/s and 20 m/s wind speed bins, the modified central composite design with the quadratic region provided more accurate results. However, for the 19 m/s wind speed bin, both methods displayed similar performance: the central composite design slightly underestimated the fatigue loads by 0.34%, while the modified central composite design with the quadratic region resulted in a marginal overestimation of 0.35%.

Table 12: Estimated damage equivalent loads using the central composite design and a modified version of the central composite design

Analysis Method	DEL (MPa)			Error (%)		
	18 m/s	19 m/s	20 m/s	18 m/s	19 m/s	20 m/s
<b>Fatigue load calculations of each data point</b>	23.265	24.991	27.213	N/A	N/A	N/A
<b>CCD using interactive linear regression</b>	23.140	24.905	27.410	-0.54%	-0.34%	0.72%
<b>Modified CCD using interactive quadratic regression (PLE&lt;0.1), and interactive linear regression (PLE &gt; 0.1)</b>	23.368	25.079	27.253	0.44%	0.35%	0.15%
<b>Modified CCD using only interactive linear regression</b>	23.594	25.249	27.608	1.41%	1.03%	1.45%

Across all examined wind speed bins, the modified central composite design with the quadratic region slightly overestimated fatigue loads, with the maximum error rate being 0.44%. On the other hand, the central composite design demonstrated a mixed performance – it overestimated fatigue loads in the 20 m/s wind speed bin but underestimated fatigue loads in the 18 m/s and 19 m/s bins. The highest error for the central composite design was found in the 20 m/s wind speed bin, with an overestimation of 0.72%.

Conversely, the modified central composite design, which employed only an interactive linear regression, demonstrated a less satisfactory performance. It showed a minimum error rate of 1.03% and a maximum of 1.45%. Interestingly, this reduced accuracy occurred despite the use of a larger data set compared to the original central composite design. This can potentially be attributed to the fact that the modified central composite design placed more emphasis on the region where the DEL and PLE variation is non-linear. Consequently, this emphasis increased the overall error rate due to the assumption of linearity in that region.

Based on the results of this analysis, only the methodologies which provided the most accurate results will be further utilized. This includes the central composite design utilizing an interactive linear regression and the modified central composite design that incorporates both a quadratic and a linear region. These two methods, having demonstrated the highest accuracy, will be applied to the real-world context of the Hollandse Kust (Zuid) wind farm. This application will not aim at verifying which of the two methods is more accurate, as this would be difficult to be determined in a real-world context. Instead, the purpose is to observe how these methods perform under actual field conditions and to compare the results. This can offer valuable insights into their applicability and potential benefits for use in real-world wind energy scenarios.

### Applying Response Surface Methodology to Hollandse Kust (Zuid) Wind Farm Site Location

The response surface methodology will be utilized to estimate the damage equivalent load of the Class IB 15-MW reference turbine at certain wind speed bins of 18, 19, and 20 m/s under the wind conditions specified in Hollandse Kust (Zuid) wind farm location. These specific wind speed bins are chosen because they correspond to scenarios where the 90% quantile of turbulence surpasses the design limit established for the Class IB 15-MW reference turbine.

The regression parameters ( $\beta$ ), which were derived from both the central composite design and the modified central composite design (see Figure 16) will be utilized to estimate fatigue loads across the various combinations of Turbulence Intensity (TI) and Power Law Exponent (PLE), as depicted in Figure 20. The estimated damage equivalent loads will then be validated against the damage equivalent load calculated for Class IB wind conditions. Note that the design conditions for offshore Class IB wind turbine assume a PLE value of 0.14 and a turbulence intensity level which follows Eq. (5.8) (IEC, 2005, 2009).

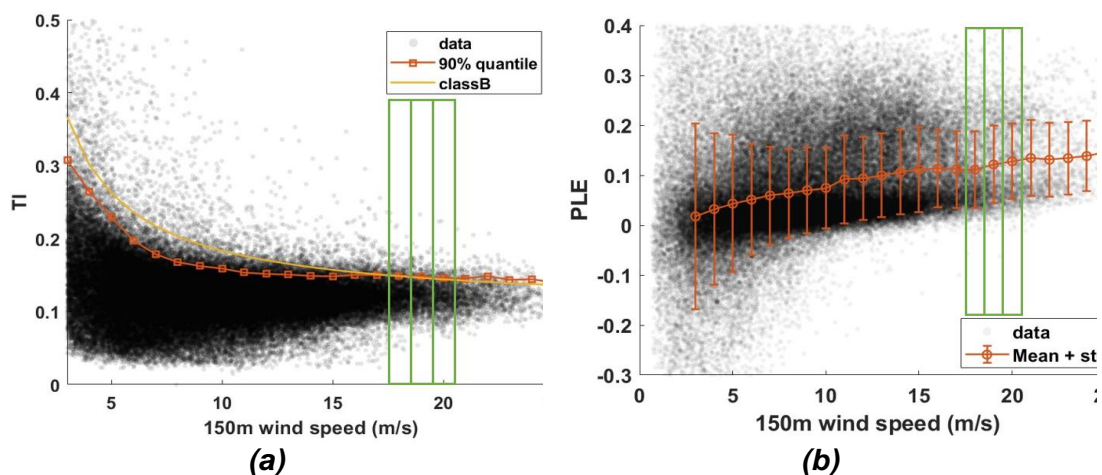


Figure 20: Distribution of data points for (a) turbulence intensity and (b) power law exponent across different wind speed bins, to which the response surface methodology will be applied.

Table 13: Estimated damage equivalent loads for Class IB 15-MW reference turbine under Hollandse Kust (Zuid) atmospheric conditions.

Analysis Method	DEL (MPa)		
	18 m/s	19 m/s	20 m/s
<b>IEC Class IB</b>	28.887	29.133	30.125
<b>CCD using linear regression with an interaction term</b>	26.454	27.668	28.751
<b>Modified CCD using quadratic regression with an interaction term for PLE&lt;0.1, and linear regression with interaction term for PLE &gt; 0.1</b>	26.412	27.715	28.767

The results depicted in Table 13 indicate that the fatigue loads estimated by the response surface methodology are lower than those projected for the design of an IEC Class IB wind turbine. This suggests that the wind conditions at the Hollandse Kust (Zuid) wind farm are less severe than the conditions that were presumed during the design of the IEA 15-MW reference turbine. In comparing the two methods—using the central composite design and the modified central composite design for the response surface methodology—there is minimal variation in the results, with a maximum deviation of around 0.17%.

These findings highlight the efficacy of the response surface methodology in predicting site-specific fatigue loads. It effectively reduces the number of simulations required, with only nine simulations for each wind speed bin when utilizing the central composite design, and 15 simulations for each wind speed bin when adopting the modified central composite design. Despite the slightly more accurate results provided by the modified central composite design when applied to the artificial site, the difference in results becomes almost negligible when applied to the Hollandse Kust (Zuid) wind conditions. Thus, the additional six simulations required for each wind speed bin using the modified central composite design may not be justified in terms of computational efficiency. The aim should be to strike an optimal balance between computational efficiency and prediction accuracy.

## 5.4. Summary and Conclusion

Wind turbines are typically designed and certified in accordance with class categories defined by International Electrotechnical Commission (IEC) standards (IEC, 2005, 2009). When planning to deploy a turbine, these standards necessitate confirmation that the wind conditions at the proposed site are less severe than those outlined in the turbine's design specifications. However, due to the natural variations in wind climate parameters, there may be instances where one or more site parameters exceed their design values. In such cases, it becomes mandatory to verify the turbine's structural integrity via load calculations (IEC, 2005). These calculations involve estimating the wind turbine loads using aero-elastic simulations that incorporate the site-specific wind climate parameters. However, performing a significant number of these simulations is both time-consuming and expensive. Furthermore, in a wind farm, there will typically be several wind turbines that exceed the reference wind climate parameters, requiring a site-specific load calculation for each one (Toft et al., 2016). Hence, the need for an approach that accurately and efficiently conducts these assessments is crucial.

With this in mind, the goal of this chapter was to validate and refine on existing models used for assessing site-specific wind turbine fatigue loads. The primary focus is related to the fatigue loads that occurs at the blade root of a wind turbine in the flapwise direction. This is due to the fact that the flapwise direction typically experiences the most significant loads (Teixeira et al., 2017). Furthermore, this investigation focused on two key atmospheric conditions: wind shear and turbulence. These parameters have been chosen since they exhibit the greatest impacts on wind turbines fatigue loads (Veldkamp, 2007).

This chapter commenced by exploring the separate effects of wind shear and turbulence intensity on the fatigue loads experienced at the wind turbine blade root. Subsequently, the intricate relationship between these two atmospheric conditions and their combined effect on fatigue loads was examined. The chapter then proceeded to the application of a mathematical modeling approach, the response surface methodology (RSM), which leverages the central composite design for fatigue load assessment as proposed by Toft et al. (2016). This methodology was tested against an artificial site in order to understand its efficiency and accuracy in predicting site-specific fatigue loads. Based on these evaluations and insights, the study proposed an enhanced design methodology, the modified central composite design, aiming to provide a more robust and accurate model to assess and predict the impact of site-specific conditions on wind turbine fatigue loads.

Based on aeroelastic simulations of the IEA 15-MW reference turbine (Gaertner et al., 2022) using OpenFast (NREL, 2021), this study found a linear dependency, in good approximation, between turbulence intensity and fatigue loads encountered at the blade root of the wind turbine in the flapwise direction. Similar observations have been reported by Veldkamp (2007) and Slot et al. (2018). However, when examining the effects of wind shear, the study discovered some distinctions. The relationship between the power law exponent (PLE) and fatigue loads differed based on the range of the PLE values. At the upper range of the PLE, there was a linear correlation between the PLE and fatigue loads. On the other hand, at the lower range of the PLE,

a quadratic expression provided a better representation of the relationship between PLE and fatigue loads. Moreover, the study observed that the width of the non-linear region, where the quadratic relationship between PLE and fatigue loads was more accurate, increased as wind speed rose. In specific wind speed conditions, such as a bin of 20 m/s, the non-linear region was found to occur under PLE values ranging between -0.1 to 0.1. However, at a wind speed bin of 10 m/s, the non-linear region was found to occur under PLE values ranging from 0.02 to 0.05.

The study then navigated the complex dynamics between wind shear and turbulence intensity. Instead of viewing them in isolation, this part of the research focused on their interplay and how their combined influence shapes the fatigue loads. The results showed that an increase in PLE does not necessarily result in higher fatigue loads when the effects of turbulence are considered. This implies a complex relationship between the two variables, where the impact of one can either amplify or diminish the effect of the other. For instance, higher wind shear may lead to varying wind speeds across different parts of the rotor, potentially increasing fatigue loads. However, when combined with high turbulence, the rotor continuously adjusts to the changing wind conditions, reducing the influence of wind shear. Thus, the interaction between wind shear and turbulence creates a nuanced effect on fatigue loads that cannot be simply determined by summing the individual effects.

To evaluate site-specific fatigue loads, Toft et al. (2016) introduced the response surface methodology using the central composite design. This methodology incorporates a linear regression model with an interaction term to account for the effects of interactions between the climate parameters in the context of fatigue loads. While this approach has shown effectiveness, it has a limitation in capturing the region where a non-linear relationship between the Power Law Exponent (PLE) and fatigue loads occur. To address this limitation, study presented an alternative approach that utilizes the response surface methodology with a modified version of the central composite design. This approach proposed to utilize a quadrated regression model with an interaction term in the region characterized by non-linearity between PLE and fatigue loads. Additionally, in the region where linearity occurs, a linear regression model with an interaction term is utilized.

During the validation process using an artificial site, both response surface methods, demonstrated a high level of accuracy. The maximum error rate observed for the RSM with the central composite design was 0.72%, while the RSM using the modified central composite design exhibited a maximum error rate of 0.44%. Overall, the latter showed better degree of accuracy. However, when applied to real-world conditions based on the actual measurements obtained from the Hollandse Kust (Zuid) wind farm location, the differences in results obtained from the both methods were minimal, with a maximum deviation of 0.17%. This may suggest that the modified central composite design, which requires an additional six simulations for each wind speed bin, may not be justified in terms of computational efficiency. It is essential to find a balance between computational efficiency and prediction accuracy in order to optimize the load assessment process. Achieving this balance is a topic that should be explored in future research.

# Chapter 6. Performance of Wind Turbines in Relation to Atmospheric Conditions

Wind turbine manufacturers continue to develop larger-capacity turbines as wind farms can be scaled up by cost savings (Bilgili et al., 2021). As the capacity increases, it becomes essential to accurately measure power curves and calculate the anticipated energy yield.

Several factors that influence the power production of wind turbines can be primarily classified into terrain effects (such as obstacles), surface roughness, wakes of nearby wind turbines, and atmospheric conditions. Among these, atmospheric conditions can be further subdivided into aspects such as turbulence intensity, wind shear and atmospheric stability (Kim et al., 2021). However, the impacts of these atmospheric conditions on the performance of wind turbines are complex and not fully understood (Kovalnogov et al., 2022). Therefore, the aim of this chapter is to investigate whether it is possible to accurately predict the power output of wind turbines using simple modules which consider the effects of wind shear and turbulence.

## 6.1. Introduction

Accurate energy yield prediction is the ultimate goal of wind resource assessment (Kim et al., 2021). It enables investors to make informed decisions regarding the feasibility and profitability of wind energy projects. By knowing the expected energy yield, investors can assess the potential return on investment and determine whether the project aligns with their financial goals.

To predict the Annual Energy Production (AEP) of wind turbines, two key parameters are needed; the wind turbine power curve and the wind speed distribution (often represented by a Weibull distribution). A simple graphical representation is shown in Figure 21. If these two parameters are accurately predicted, one can determine the expected annual energy output by integrating the power curve with the Weibull probability distribution function (PDF) over the entire wind speed range and multiply this value by the number of hours in a year. However, both the power curve and the PDF are site dependant and are affected by the atmospheric conditions (Kim et al., 2021). Therefore, careful consideration is needed to account for the atmospheric conditions' effects on power production.

## Power Production =

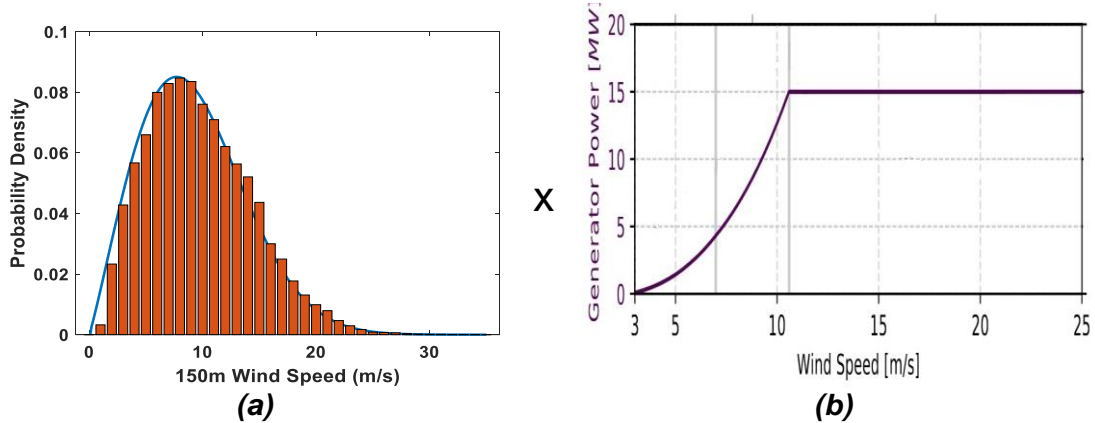


Figure 21: Estimation of Power production based on (a) Probability density function, (b) wind turbine power curve (Gaertner et al., 2022)

Traditionally, power curves and velocity distribution curves are developed based on wind speeds corresponding to the hub height (Ryu et al., 2022). This assumption can be valid for small wind turbines with short blade length since the variation of wind speed by height is relatively small. Thus, the error in predicted power output using hub height wind speed (HHWS) compared to the actual generated power is not large (Ryu et al., 2022; Scheurich et al., 2016). However, for larger wind turbines, the measured wind speed at the hub height does not necessarily represent the inflow across the turbine rotor disk. In the atmosphere, the vertical wind speed usually changes with height, a phenomenon known as wind shear (Murphy et al., 2020). Moreover, the wind inflow across the rotor disk of a wind turbine is also inherently turbulent, causing temporal variations in the wind speed. Turbulence introduces further complexities in accurately predicting the power output of wind turbines. Therefore, the aim of this section is to investigate different methods used to incorporate the effects of wind shear and turbulence intensity on a site-specific power curve in order to accurately estimate the AEP of a wind turbine.

### *Integrating Wind Shear Effects Into a Site-Specific Power Curve*

In order to account for the effects of wind shear on the power output of a wind turbine, the use of the so-called rotor equivalent wind speed (REWS) has been proposed (Ryu et al., 2022; Scheurich et al., 2016; van Sark et al., 2019; Wagner, 2010; Wagner et al., 2014). Rather than considering a simple hub height wind speed for energy prediction, the concept of REWS was developed to represent the energy content of the wind across the entire area of the turbine rotor (Wagner, 2010). Since a wind turbine's rotor sweeps a large vertical area, the wind speed is not the same at the top of the rotor as it is at the bottom. Therefore, the concept behind REWS should ideally account for this vertical variation in wind speed and reduce all speed measurements into a single value. It is calculated by taking the energy-weighted mean of the wind speed over the rotor area as follows (van Sark et al., 2019):

$$REWS = \sqrt[3]{\sum_{i=1}^{n_h} \frac{A_i}{A} u_i^3} \quad (6.1)$$

Where  $A_i$  is the area of each segment,  $A$  is the rotor area,  $n_h$  is the number of segments, and  $u_i$  is the wind speed at the center of each segment (refer to Figure 23).

When estimating the Annual Energy Production (AEP) of a wind turbine for a specific site, the rotor equivalent wind speed (REWS) method can be applied in two steps. First, during performance testing, the power output of the turbine should be measured and recorded as a function of the REWS instead of the hub height wind speed. By doing so, a new power curve can be developed which should ideally account for the effects of wind shear. Second, when modeling the wind speed probability distribution function for the site, it should be expressed as a function of the REWS rather than the hub height wind speed. By incorporating the REWS in these steps, the estimation of AEP should theoretically provide a more precise assessment of the turbine's expected energy production for the specific site. However, the validity of this method has been put into question (Redfern et al., 2019; Ryu et al., 2022; van Sark et al., 2019; Wagner, 2010; Wagner et al., 2014).

#### *Validity of REWS Method*

Ryu et al. (2022) investigated the potential accuracy of REWS based on actual power measurements of Anholt offshore wind farm in Denmark (turbine capacity = 3.6 MW,  $H = 81.6$  m,  $D = 120$  m). The study revealed that a basic hub height wind speed mimicked the real power production more accurately than the REWS under unstable, neutral, and stable atmospheric conditions. However, in instances of extreme instability or strong stability in the atmosphere, the REWS proved superior, showing a notable reduction in error relative to actual power generation as compared to the HHWS. Specifically, under strongly stable atmospheric conditions, the discrepancy between actual power production and REWS predictions can be cut down by over 5%. Redfern et al. (2019) investigated the effectiveness of REWS by evaluating three different cases; neutral stability with low wind shear, high stability with high wind shear, and high stability with non-linear wind shear. The results indicated that REWS can significantly improve the power prediction accuracy when a non-linear strong wind shear occurs. However, marginal impacts were observed in the other two cases. Wagner et al. (2010) found that the use of REWS decreased the scatter around the fitted power curve. However, in a later study, Wagner et al. (2014) compared REWS power curves to hub height power curves for eight different datasets. The results were inconclusive as the REWS resulted in higher AEP when compared hub height wind speed in five cases, but lower in two cases. Moreover, there was no clear reduction in the power curve scatter for all different cases. Therefore, Wagner concluded that the differences between REWS and hub height wind speed are site dependent. Similar results were concluded by van Sark et al. (2019) who found insignificant differences in power predictions between REWS and hub height wind speed for wind shear exponents ranging from  $-0.05 < \alpha < 0.4$ . The differences when considering a non-constant wind profile were also found insignificant and were limited to about 1%.

However, for PLE values outside the range of  $-0.05 < \alpha < 0.4$ , the REWS method has shown to improve the accuracy of power output predictions.

### *Effects of Turbulence on the Power Performance of a Wind Turbine*

Another important aspect when it comes to wind resource assessment is considering the effects of turbulence on wind turbines power curves. In general, the mean kinetic energy is increased by turbulence (refer to Eq. (6.3)). However, the mean power does not necessarily follow the mean kinetic energy since power is not a linear function of the kinetic energy (Wagner, 2010). As explained by Bardal and Sætran (2017), turbulence can increase or decrease power production depending on which region of the power curve the wind turbine is operating at. This is further demonstrated in Figure 22. At the left side of the power curve, power increases with increasing TI. This is because the power output in that region is directly related to the cube of the wind speed. However, TI has the opposite effects while transitioning towards the rated power region. Beyond the inflection point, power decreases with increasing TI. This is because the power produced during positive fluctuation of wind speed is limited to the rated power, while during negative fluctuations in wind speed, power production is reduced approximately following the cube of wind speed.

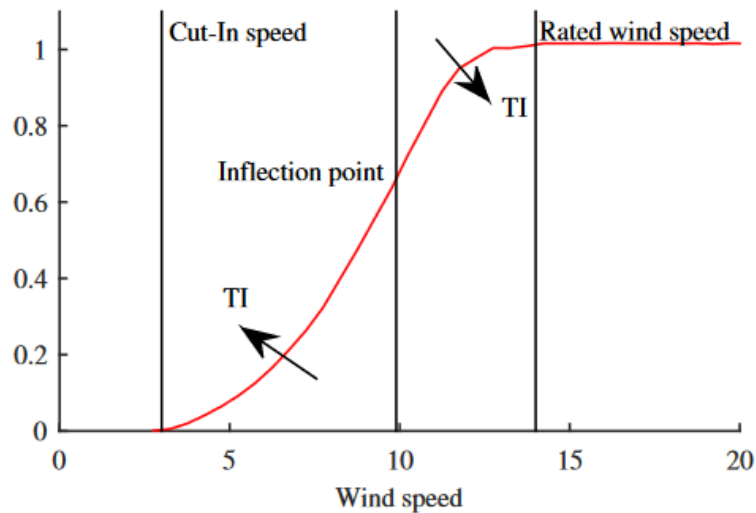


Figure 22: Influence of TI on power production (L. M. Bardal & Sætran, 2017)

Similar to the concept of REWS, one can also wonder if a simple expression of an equivalent wind speed can be developed based on the turbulence kinetic energy flux. Following Wagner et al. (2010), wind speed can be expressed as a sum of its mean and turbulent part. Since power is a function of the cube of wind speed, one can express the cube of wind speed based on Taylor development as:

$$u^3 = (\langle u \rangle + u')^3 = \langle u \rangle^3 + 3\langle u \rangle^2 u' + 3\langle u \rangle u'^2 + u'^3 \quad (6.2)$$

Where,

$u$  Wind speed

$\langle u \rangle$  Mean wind speed

$u'$  Turbulent component of wind speed

Under the assumption that the fluctuation in wind speed follows a Gaussian distribution, the second term and the last term can be canceled. This is because the positive fluctuations and the negative fluctuations of  $u'$  and  $u'^3$  average out to zero. Generally, the term  $(u')^n$  only cancels out if  $n$  is an odd number following a Gaussian distribution. However, if  $n$  is an even number, the results will always become positive, and therefore, the negative fluctuations cannot cancel out the positive ones.

The mean cube wind speed can then be expressed as:

$$\langle u^3 \rangle = \langle u \rangle^3 \left( 1 + 3 \frac{\sigma^2}{\langle u \rangle^2} \right) = \langle u \rangle^3 (1 + 3(TI)^2) \quad (6.3)$$

Finally, one could define the equivalent wind speed as:

$$U_{eq-TI} = \sqrt[3]{\sum_i \langle u_i \rangle^3 (1 + 3(TI_i)^2)} \quad (6.4)$$

From Eq. (6.4), one can notice that  $U_{eq-TI}$  always increases with increasing  $TI$ . However, this is not always the case as explained earlier. The problem arises beyond the inflection point since power decreases with increasing  $TI$ . Therefore, it appears that a simple equivalent wind speed as a function of turbulence cannot be simply accounted for (Wagner, 2010).

### *Integrating Turbulence Effects Into a Site-Specific Power Curve*

To account for the effects of turbulence on wind turbine power curves, manufacturers can rely on aeroelastic simulators to predict the performance of wind turbines under various turbulence conditions. However, such methods are both time-consuming and expensive. Therefore, there is a need for simple models which can be used by site developers to account for the effects of turbulence on a site-specific wind turbine power curve (Clifton & Wagner, 2014).

The so-called turbulence renormalization method (or zero-turbulence power curve method) was developed by Albers et al. (2007) to address such needs. The advantage of this method as explained by Bardal and Sætran (2017) is that it allows for power data gathered under limited turbulence range to be used to mimic power production under diverse turbulence circumstances. For example, during performance testing, manufacturers record key data such as power output, average wind speed (measured at the turbine hub height or based on the REWS method), and changes in wind speed over 10-minute intervals. These data are used to create a site-specific power curve, which describes how the turbine performs under the specific wind conditions at the test site. However, the conditions at the test site are unlikely to match those at other potential wind farm locations. This means the power curve obtained from the test site may not apply to these other sites. This is where the zero-turbulence power curve method proves to be beneficial as it allows us to use the limited range of data collected from the testing site to create a simulation of the turbine's performance under a wider range of wind conditions at other locations.

The concept behind the turbulence renormalization method is to first remove the effects of turbulence from the measured power curve to create a “zero-turbulence power curve.” When there is a need to model a new power curve that represents different atmospheric conditions, the turbulence effects can be reintroduced to the zero-turbulence power curve to reflect those conditions. However, the accuracy of this method is put into question.

Clifton and Wagner (2014) conducted two experimental scenarios. In the first scenario, they used power curve data gathered under low Turbulence Intensity (TI) conditions to predict the power curve under high TI environment. In the second scenario, they used power curve data collected under high TI conditions to forecast the power curve under low TI environment. Overall, it was found that the turbulence renormalization method overcompensated the effects of turbulence which led to overestimating the power production when going from high to low turbulence environment, and underestimation when going from low to high turbulence environment. However, both test cases showed a reduction in energy yield prediction errors when compared to using the original non-renormalized power curve.

A similar approach to evaluate the accuracy of the turbulence renormalization method was adopted by Bardal and Sætran (2017). The results of their study suggested that using the turbulence renormalization method reduced the AEP error by a factor of 50% when compared to the original non-renormalized power curve. However, opposite to the findings of Clifton and Wagner (2014), there was a slight under-compensation for the turbulence effects in both test cases.

## **6.2. Aim and Objectives**

The aim of this chapter is threefold. First, it sets out to investigate the effects of wind shear and turbulence intensity on the power performance of a wind turbine. This involves an exploration of how variations in wind speed and atmospheric turbulence can influence the operational efficiency of a wind turbine and impact its overall energy output.

The second aim is to evaluate the accuracy and applicability of the Rotor Equivalent Wind Speed (REWS) method in predicting wind energy yields. Despite its widespread use, the validity of the REWS method under various atmospheric conditions has been questioned. This research will assess its performance and applicability.

Finally, the research seeks to evaluate the accuracy and applicability of the turbulence renormalization method, also known as the "zero-turbulence power curve" method. This innovative method, used for predicting wind turbine performance under varying turbulence conditions, has yet to be comprehensively validated. By comparing its efficacy with results derived from the use of the original non-renormalized power curve, this research will aim to assess its potential for improving the accuracy of wind energy yield predictions.

## **6.3. Methodology**

This section is broken down into several key components to provide a detailed overview of the approaches adopted in this research. The first subsection details the method used to examine the impacts of wind shear and turbulence intensity on the power performance of a wind turbine. The research tools, software, and techniques involved in this part of the study will be thoroughly discussed

The second part explains the process of calculating the Rotor Equivalent Wind Speed (REWS) and how its accuracy could be verified. This involves a step-by-step walkthrough of the process of determining the REWS from wind speed data and the specifics of how the REWS method is applied and validated.

The final part of the section explores the Turbulence Renormalization method, also known as the "zero-turbulence power curve" method. This section delves into the specifics of this method - from the initial steps of removing turbulence effects from the measured power curve to create a "zero-turbulence power curve," to the process of reintroducing these effects to model a new power curve that represents different atmospheric conditions.

### **6.3.1. Evaluating the Impact of Wind Shear and Turbulence Intensity on the Performance of Wind Turbines**

In order to delve into the effects of wind shear and turbulence intensity on wind turbine performance, this study will utilize the simulation outputs of the IEA 15-MW wind turbine outlined in section 4.4.

To isolate and study the effects of wind shear, the 15-MW reference turbine's power output is simulated under two wind conditions: uniform wind conditions and sheared wind flow conditions while eliminating the effects of turbulence. The Power law exponent is set at different values ranging from 0 to 0.5. The power outputs from these two scenarios are then compared, highlighting the differential impact created by wind shear. It is important to note that this evaluation focuses only on wind speeds below the rated wind speed. The rationale behind this is that the influence of wind shear on power production becomes ambiguous beyond the rated wind speed as the power output is constrained to the rated power. Thus, the research concentrates on the segment of wind speeds where the influence of wind shear on power production is most pronounced and observable.

Similarly, to examine the impact of turbulence intensity on the power output of the 15-MW reference turbine, the study employs an approach that isolates turbulence effects while excluding the influence of wind shear. This approach allows for an unobstructed understanding of how turbulence alone impacts turbine performance. The simulations are conducted across a range of turbulence intensity intensities, ranging from 0% to 50%. Each turbulence intensity level will result in a unique power curve for the 15-MW reference turbine. By comparing these power curves, the study can quantify and

understand how the power output of the wind turbine changes with varying turbulence intensity levels.

### 6.3.2. Rotor Equivalent Wind Speed Method

This section is subdivided into two parts. First, the method used to calculate the rotor equivalent wind speed will be addressed, and second, the strategy adopted to verify the precision and accuracy of the REWS method will be discussed.

#### Computation of Rotor Equivalent Wind Speed

In alignment with the approach utilized by van Sark et al. (2019), the wind turbine's rotor swept area is divided into five distinct segments, as depicted in Figure 23. Detailed calculations pertaining to the area of each segment are provided in Appendix B. The height of each individual segment can be straightforwardly defined as follows:

$$h_i = H + \frac{D}{5}(i - 3) \quad \text{where } i \in (1,5) \quad (6.5)$$

Where, H is the hub height, and D is the rotor diameter.

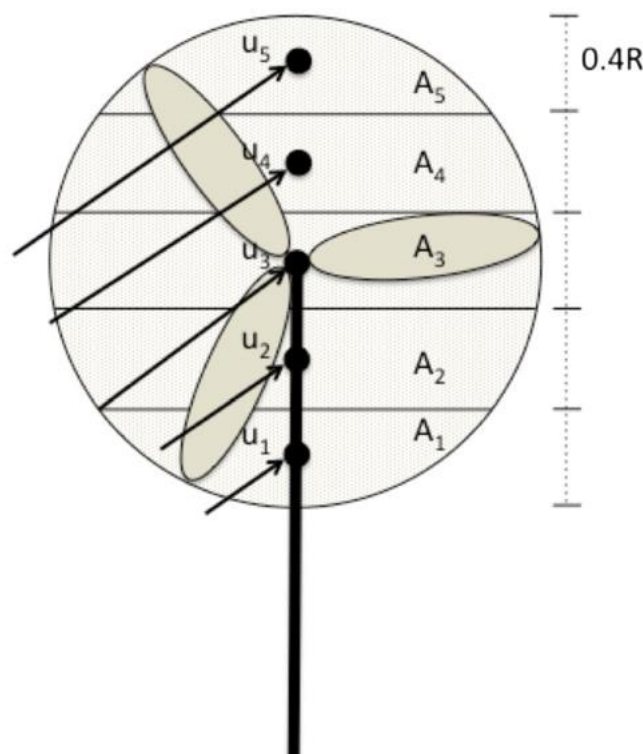


Figure 23: Rotor equivalent wind speed based on five different segments (van Sark et al., 2019)

The velocity values for each segment can be derived through several methods. These could include direct measurements using technologies such as LiDAR, estimated based on the power law as depicted in Eq. (2.9) assuming a constant wind shear coefficient, estimated using the logarithmic law using Eq. (2.10), or estimated through the stability corrected logarithmic law according to Eq. (2.11).

If a constant wind shear coefficient is assumed, the rotor equivalent wind speed can be calculated as

$$REWS = u_h \sqrt[3]{\sum_{i=1}^5 \frac{A_i}{A} \left(\frac{u_i}{u_h}\right)^3} \quad (6.6)$$

Where the values of  $A_i/A$  and  $u_i/u_h$  are listed in Table 14.

Table 14: Rotor equivalent wind speed (REWS) parameter values based on the depicted five segment heights (van Sark et al., 2019)

$i$	$h_i$	$\frac{u_i}{u_H}$	$\frac{A_i}{A}$
1	$H - 0.4D$	$\left(1 - 0.4\frac{D}{H}\right)^\alpha$	0.1424
2	$H - 0.2D$	$\left(1 - 0.2\frac{D}{H}\right)^\alpha$	0.2312
3	$H$	1	0.2529
4	$H + 0.2D$	$\left(1 + 0.2\frac{D}{H}\right)^\alpha$	0.2312
5	$H + 0.4D$	$\left(1 + 0.4\frac{D}{H}\right)^\alpha$	0.1424

### Validation of Rotor Equivalent Wind Speed Method

If a wind turbine power output data is readily available, validating the Rotor Equivalent Wind Speed (REWS) can be carried out by monitoring the power output of a wind turbine and constructing two distinct power curves. The first power curve will be based on the wind speed at the hub height, and the second power curve will be developed using the REWS approach.

Once the two power curves have been constructed, they can be compared to each other. The comparison should focus on the degree of scatter around each curve. Scatter in this context refers to the deviation of individual data points from the overall mean depicted by the power curve. If the REWS method is accurate and effective, it should yield a power curve with less scatter compared to the hub-height based curve. This would imply that the REWS method is better at capturing the real-life, operational performance of the wind turbine, thus increasing the accuracy of power production estimation under varying wind conditions. A similar approach was adopted by Bardal et al. (2015) in which their results showed no clear reduction of the scatter when using the REWS method as demonstrated in Figure 24.

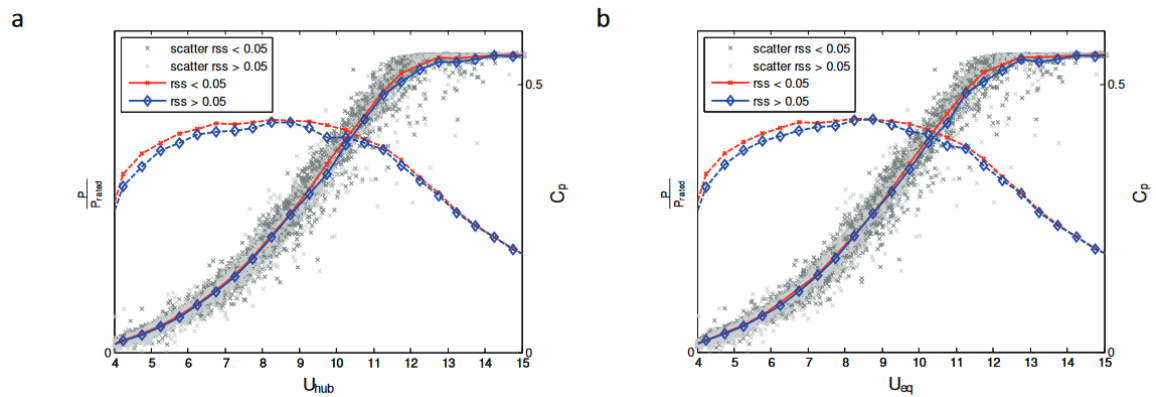


Figure 24: Power curve based on hub wind speed (a) and equivalent wind speed (b) (L. Bardal et al., 2015)

However, data related to actual power measurements of a wind turbine are not easily available. Therefore, this research will adopt the approach of Wagner et al. (2010) by developing simulation based power curves.

The applicability of the REWS method will be validated under two different test condition. First, assuming a constant wind shear PLE coefficient of 0, 0.05, 0.1, 0.15, 0.2 and 0.3. Second, using actual LiDAR measurements of Hollandse Kust (Zuid), which is a more realistic scenario since wind shear in real-world conditions can vary across height.

With regards to the first test condition, the OpenFast simulation outputs of the IEA 15-MW wind turbine outlined in section 4.4 will be utilized. Similar to the approach of Wagner et al. (2010), the effects of turbulence will be eliminated in order to isolate the effects of wind shear. The evaluation will only focus only on wind speeds below the rated wind speed since that the effects of wind shear on power production becomes ambiguous beyond that point. Two power curves will be constructed to evaluate the effectiveness of the REWS method. The first power curve represents the power output as a function of hub height wind speed, and the second power curve represents the power output as a function of the rotor equivalent wind speed. The reliability of these two methods will be gauged using the Root Mean Square Error (RMSE) as a key performance metric.

With regards to the second test conditions, one concern is that LiDAR measurements of Hollandse Kust (Zuid) extend only up to 200 meters, whereas the blades of the 15-MW referenced turbine reach up to a height of 270 meters (Gaertner et al., 2022). To resolve this concern, it is needed to extrapolate the wind speed measurements to different heights. One could utilize the results depicted in section 3.4.2 to evaluate which extrapolation method is most suitable based on the atmospheric stability conditions (e.g., for very unstable atmospheric conditions, it is found that both the free convection and Businger-Dyer extrapolation methods work best). However, for the purpose of simplicity, the power law method will be applied to extrapolate the wind speeds to different heights as depicted in Figure 25. The LiDAR wind speed measurements at heights of 40, 80, 120, 160, and 200 meters are then used as a baseline to estimate wind speeds at the height of 54, 102, 150, 198, 247 meters respectively.

It can be noted from Figure 25 that the LiDAR wind speed measurement at a height of 160 meters is used to extrapolate the wind speed at a height of 198 meters, while the actual wind speed measurements at a height of 200 meters is available. This approach is deliberately employed to maintain the variability, or 'scatter', of wind speed measurements across the rotor swept area. In other words, if a wind turbine's dimensions were to fall within the range of the LiDAR measurements, the scatter of wind speed data points experienced by the turbine would be similar to the scatter captured in this study through extrapolation.

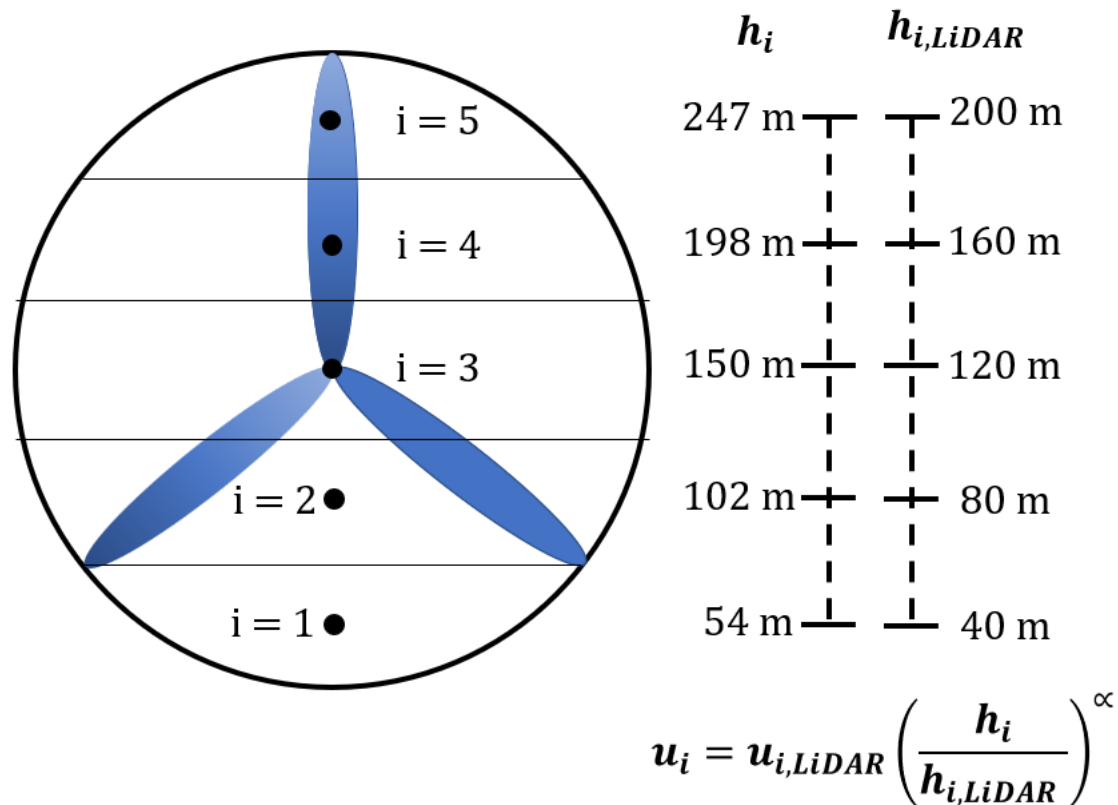


Figure 25: Extrapolation-based process for estimating wind speeds at multiple segments' heights

Following the establishment of the wind speed data at multiple rotor heights through extrapolation, the subsequent phase involves the selection of wind speed data based on the actual LiDAR measurements at Hollandse Kust (Zuid). Given the abundance of available data, specific criteria were developed to guide the selection process.

First, the wind speed data for both the hub height and Rotor Equivalent Wind Speed (REWS) should lie within the 5 to 10 m/s range. This range was chosen because it is within these wind speeds that the influence of wind shear is most noticeable and significant on wind turbine power output. Second, the chosen data should adequately represent different atmospheric stability classes. Drawing from Figure 6 (a) in section 3.3.1, it is evident that within the wind speed range of 5 to 10 m/s, conditions of very unstable atmospheric conditions tend to dominate. To ensure that the data set encompasses a wide range of atmospheric stability conditions, six data sets were chosen to represent very unstable conditions, while three additional data sets were

chosen to represent each of the other stability classes. In total, 18 different data sets have been randomly chosen based on the selection criteria.

Once the specific data sets have been selected, the next phase involves the generation of distinct wind fields. Utilizing TurbSim (NREL et al., 2021), 18 different wind fields are created based on the chosen data sets. Each of these wind fields represents a unique combination of wind speeds and atmospheric stability conditions, thereby enabling the examination of the wind turbine's performance under a wide range of wind conditions. Next, the generated wind fields are used as an input to simulate the performance of the 15-MW reference turbine using OpenFast. Since that the effects of turbulence are not accounted for, the duration of each simulation is set to 10-minutes.

Finally, two power curves will be constructed based on the simulation outputs to evaluate the effectiveness of the REWS method. The first power curve represents the power output as a function of hub height wind speed, and the second power curve represents the power output as a function of the rotor equivalent wind speed. The reliability of these two methods will be gauged using the Root Mean Square Error (RMSE) as a key performance indicator.

### 6.3.3. Turbulence Renormalization Method

This section is subdivided into two parts. First, the method of applying the turbulence renormalization method will be explained. Second, the strategy adopted to verify this method's precision will be discussed.

#### *Turbulence Renormalization Process*

The process for the turbulence renormalization method is fully described by Clifton and Wagner (2014). However, an overview of this process will be presented for enhanced clarity and context. Figure 26 offers a brief visual representation of the process, outlining the key steps involved in turbulence renormalization. Each step in the figure will be further detailed to ensure comprehensive understanding of the method applied in the scope of this study.

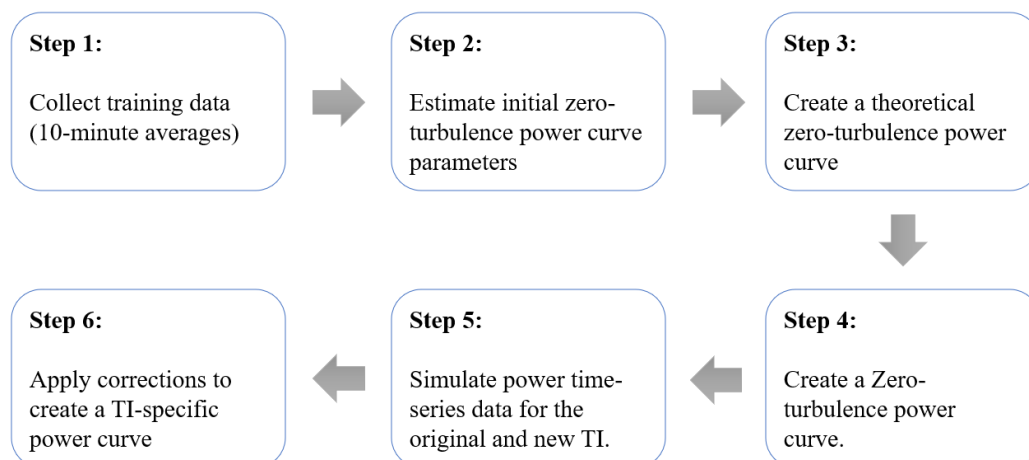


Figure 26: Process of applying turbulence renormalization method

The turbulence renormalization process starts with the collection of data. Specifically, this involves gathering 10-minute averaged wind speed and power output data under specified measured turbulence intensity levels. This data set serves as the foundational 'training data', used to construct power curves which represents the performance of a wind turbine under various turbulence conditions. For the purposes of this study, such data is derived from simulations, as opposed to being sourced from actual power performance tests. The reason for this approach is the limited accessibility of real-world test data.

The data utilized in this study consists of 144 10-minute averaged data points for each turbulence intensity level. This dataset is built on the results of six turbulence seed OpenFast simulations of the 15-MW reference turbine, spanning wind speeds from 2 to 25 m/s, with an interval of 1 m/s between each wind speed. While it is acknowledged that the volume of data collected for this study is much less than what would typically be gathered from actual site measurements, it should still provide some meaningful insights towards the applicability of this method.

### **Step 1: Collect training data**

- Mean hub-height wind speed  $u(k)$  (or REWS ) over 10-minute periods
- Hub height turbulence intensity  $TI(k)$  or standard deviation  $\sigma(k)$  over 10-minute periods
- Power output  $P(k)$  over 10-minute periods

Following the data collection, the **second step** involves estimating the parameters for what is termed the 'initial zero-turbulence power curve.' This estimation is based on the previously collected training data.

In the context of this study, air density is set at a constant value of  $1.225 \text{ Kg/m}^3$ , mirroring the conditions used across all simulation scenarios. Additionally, the rotor area of the wind turbine is assumed to remain constant. In reality, this is an oversimplification, as the area swept by a wind turbine's rotor can change due to blade deflections.

### **Step 2: Estimate initial zero-turbulence power curve parameters**

- Bin average training data ( $P(i)$ ,  $u(i)$  &  $\sigma(i)$ ) in wind speed bins of 0.5 m/s
- Calculate power coefficient  $C_p(i)$  for each bin
  - $C_p(i) = 2P(i)/(\rho u(i)^3 A)$
- Set initial zero-turbulence power curve parameters as
  - $P_{rated} = \max(P(i))$
  - $u_{rated} = \sqrt[3]{\frac{2P_{rated}}{\rho \max(C_p) A}}$
  - $u_{cut-in} = \min(u(i))$  where  $P(i) > 0.001P_{rated}$
  - $u_{cut-out} > 100 \text{ m/s}$

The **third step** calls for the creation of a 'theoretical zero-turbulence power curve.' This is achieved by integrating the initial zero-turbulence power curve over the variation of

wind speed represented by the turbulence standard deviation. A graphical illustration of the integration process considering a wind speed bin of 10 m/s is presented in Figure 27. Subsequently, an iterative process is implemented, the goal of which is to adjust the theoretical parameters - namely the rated power, cut-in wind speed, and power coefficient - to ensure their values align closely with the original parameters.

**Step 3: Create a theoretical zero-turbulence power curve**

- $u_{rated,th} = u_{rated}$ ,  $u_{cut-in,th} = u_{cut-in}$ ,  $P_{rated,th} = P_{rated}$ ,  $C_p = \max(C_p)$
- $P_{0,th} = \begin{cases} 0 & u(i) < u_{cut-in,th} \\ \frac{1}{2} \rho u(i)^3 C_{p,th} A & u_{cut-in,th} < u(i) < u_{rated,th} \\ P_{rated,th} & u(i) > u_{rated,th} \end{cases}$
- Simulate power for all bin-averaged data considering Gaussian distribution of turbulence. This process can be visualized in Figure 27
  - $\hat{P}(i) = \int P_{0,th}(u(i)) \cdot f(u(i), \sigma_u(i)) du$

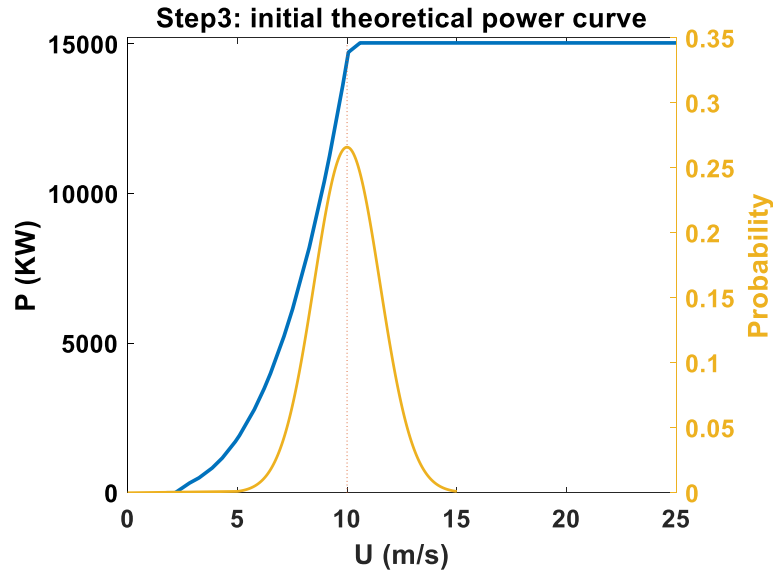


Figure 27: simulating power for bin-averaged data

- Calculate the power coefficient for the new values
  - $\hat{C}_p(i) = 2\hat{P}(i)/(\rho u(i)^3 A)$
- Ensure that the new values of  $\hat{P}_{rated,th}$ ,  $\hat{u}_{cut-in,th}$  &  $\hat{C}_{p,th}$  are within range of the original values
  - $|\max(\hat{P}_{rated}) - \max(P_{rated})| < 0.001P_{rated}$
  - $|\hat{U}_{cut-in,th} - U_{cut-in}| < 0.5 \text{ m/s}$
  - $|\max(\hat{C}_p) - \max(C_p)| < 0.01$
- If found out of range, adjust their respective values, and repeat step 3 till the values converge
  - $P_{rated,th} = P_{rated,th} - \max(\hat{P}) + P_{rated}$
  - $u_{cut-in,th} = u_{cut-in,th} - \hat{u}_{cut-in} + u_{cut-in}$
  - $C_{p,th} = C_{p,th} - \max(\hat{C}_p) + \max(C_p)$

$$\circ u_{rated,th} = \sqrt[3]{\frac{2P_{rated,th}}{\rho C_{p,th} A}}$$

**In the fourth step**, the power output for the training data is estimated using the theoretical zero-turbulence power curve. Since there will always be a disparity between the simulated power curve and the actual generated power, the differences will be incorporated into the zero-turbulence power curve. Subsequently, the data is averaged and organized into bins to determine the final “zero-turbulence power curve”.

**Step4: Create the final zero-turbulence power curve**

- *First, simulate power for all time-series data by integrating the theoretical power curve over the Gaussian distribution of turbulence (Graphical representation is similar to Figure 27).*
  - $\hat{P}(k) = \int P_{0,th}(u(k)) \cdot f(u(k), \sigma_u(k)) du$
- *Next, incorporate disparity between the simulated power and actual observations into the theoretical zero-turbulence power curve*
  - $P_0(k) = P(k) - \hat{P}(k) + P_{0,th}(k)$
- *Bin average  $P_0(k)$  in wind speed bins of 0.5 m/s to find the final Zero-turbulence power curve*

**The fifth step** involves simulating two different power outputs using the zero-turbulence power curve. This is achieved by integrating the curve over the Gaussian distribution of turbulence. The first power output simulation corresponds to the training data - this is the initial set of data used to develop the zero-turbulence power curve. The second power output simulation pertains to site-specific data.

**Step5: Simulate power time-series data for the new and original TI based on the zero-turbulence power curve.**

- *First, simulate power time-series data for the original TI assuming a Gaussian distribution of turbulence. Note that the zero-turbulence power curve, generated in the previous step, is not an explicit function of wind speed as a result of the applied correction function. This means that the equations necessary to describe the relationship between the theoretical zero-turbulence power and wind speed are not easily defined or known, which complicates the process of integrating the zero-turbulence power over the frequency distribution (see Figure 28 (a)). To overcome this challenge, this study uses a numerical technique known as Newton's interpolation. Newton's interpolation is a method used in numerical analysis to estimate unknown values for a given set of data points. In the context of this study, it is used to approximate the power output at various wind speeds along the zero-turbulence power curve (see Figure 28 (b)). The same approach was adopted by (Albers et al., 2007; Clifton & Wagner, 2014)*

$$\circ \hat{P}(k) = \int P_0(u(k)) \cdot f(u(k), \sigma_u(k)) du$$

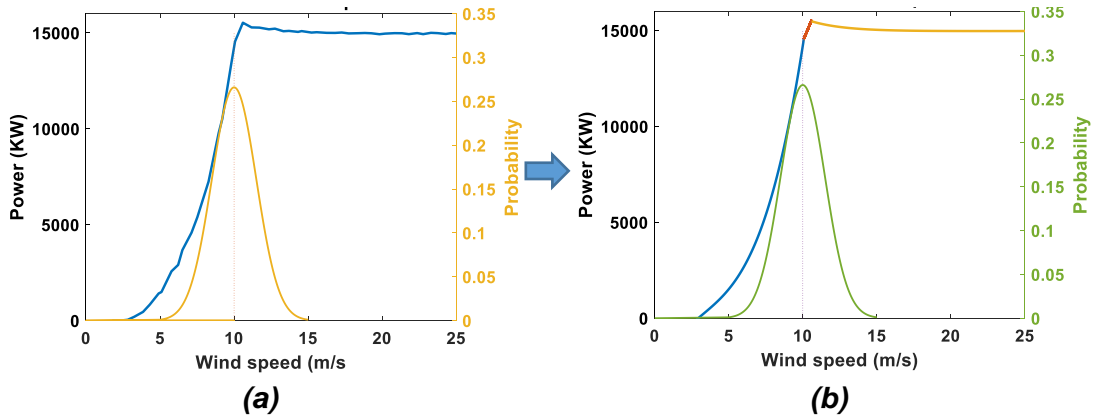


Figure 28: Example of zero-turbulence power curve derived from step 4 (a), and Newton's interpolation of the zero-turbulence power curve (b)

- Next, simulate power time-series data for the new TI assuming a Gaussian distribution of turbulence.

$$\circ \hat{P}_s(k) = \int P_0(u(k)) \cdot f(u(k), \sigma_{u,s}(k)) du$$

Once again, since there will be a disparity between the simulated power curve for the training data and the actual power curve, the differences will be incorporated into the simulated power curve of the new site

#### **Step6: Apply corrections to create a TI-specific power curve.**

- Incorporate disparity between the simulated power for the original TI and the actual observations
  - $P_s(k) = P(k) + \hat{P}_s(k) - \hat{P}(k)$
- Bin average  $P_s(k)$  in wind speed bins of 0.5 m/s to find the TI-specific power curve

#### **Validation of Turbulence Renormalization Method**

In order to verify the accuracy and relevance of the turbulence renormalization method, this study will adopt a methodology similar to the one used by Clifton & Wagner (2014) and Bardal & Sætran (2017). The validation process will start by generating two power curves based on the OpenFast simulations of the 15-MW reference turbine, each reflecting different turbulence intensity levels – one for high-level turbulence and one for low-level turbulence. Subsequently, the turbulence renormalization method will be applied to these power curves to generate predictions for alternate turbulence conditions. Specifically, the power curve derived from low-level turbulence intensity data will be used to predict a power curve that corresponds to high-level turbulence intensity conditions. Conversely, the power curve derived from high-level turbulence intensity data will be used to predict a power curve for low-level turbulence conditions.

The final stage of the validation process will involve comparing these predicted power curves to the actual power curves obtained from the simulations. This comparison will shed light on the effectiveness of the turbulence renormalization method in predicting power curves for differing turbulence conditions, thereby validating its utility and accuracy.

## 6.4. Results

The following section provides a comprehensive analysis of the results obtained in this study. Initially, the effects of wind shear and turbulence intensity on wind turbine performance are explored. The investigation delves into how these two environmental factors influence the energy output of the wind turbine, assessing impacts on the power curve. Subsequently, the section will transition into an evaluation of the Rotor Equivalent Wind Speed (REWS) method. The REWS approach will be validated in terms of its effectiveness in reducing the scatter around the power curve. Lastly, this section examines the effectiveness of the turbulence renormalization method. This process involves adjusting power curves generated under certain turbulence conditions to predict power output under alternative turbulence scenarios.

### 6.4.1. Analysis of the Wind Shear and Turbulence Intensity Effects on Power Production of a wind turbine

#### *Effects of Wind Shear on Wind Turbine Power Production*

Figure 29 illustrates the impact of wind shear on the wind turbine's power output by comparing the power obtained from sheared profiles and the power output achieved with a uniform inflow at the same hub height wind speeds. The dashed line in the figure represents the change in the wind's kinetic energy flux as a function of the PLE which is the underlying assumption behind the concept of REWS as explained in section 6.1. Similar variations in power as a function of the power law exponent have been recorded by Wagner et al. (2010).

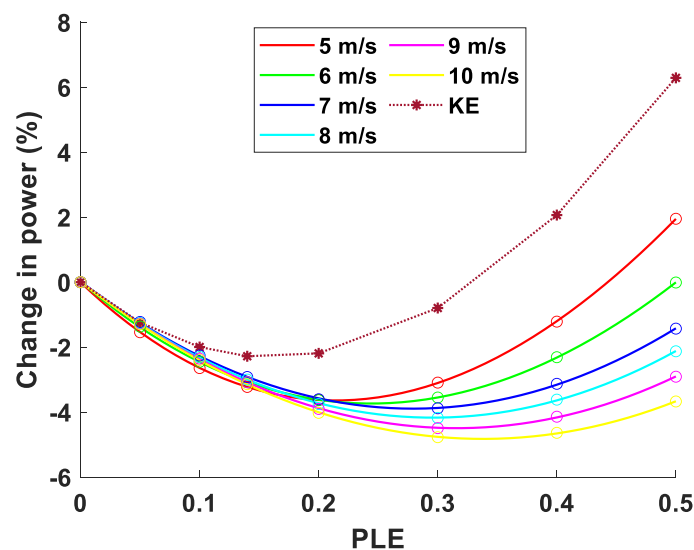


Figure 29: Differences in power output between a sheared wind profile and a uniform wind profile as a function of the shear exponent ranging from 0 to 0.5

Ideally, one would expect that the change in power production of a wind turbine should follow the change in the kinetic energy flux. However, the results show that the change in power production does not necessarily follow the change in kinetic energy flux. As

explained by Wagner et al. (2010), these differences could be associated with the control strategy and the reduced ability of the wind turbine to extract power as a result of wind shear.

In the context of the 15-MW reference turbine (Gaertner et al., 2022), the controller operation is classified into three distinct regions, as explained in section 4.2. For instance, at the lower range of wind speeds (3 m/s to 6.98 m/s), the controller regulates the rotor's speed to 5 rpm through blade pitching regardless if the power output can be maximized. This effect is demonstrated in Figure 30, where the increase in wind shear exponent results in a higher blade pitch angle. Consequently, this increase in the blade pitch angle inversely reduces the power output of the wind turbine.

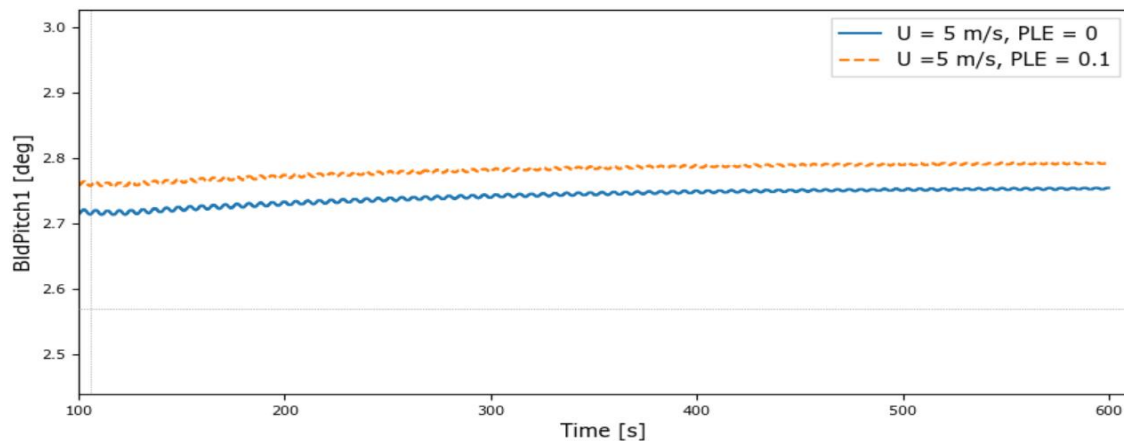


Figure 30: IEA 15-MW turbine's blade pitch at 5 m/s: uniform (blue) vs sheared (yellow)

The control strategy and the blade pitching mechanism are not the only reason why the change in power of a wind turbine does not follow the change in the kinetic energy flux. For instance, at a hub height wind speed of 9 m/s, the blade pitch angle is set by the controller to 0 degree for both a uniform flow and a sheared flow with a PLE = 0.1. However, the power output still deviates from the kinetic energy flux. As explained by Wagner et al. (2010), wind shear introduces a cyclical variation in inflow conditions, which correlates with the rotor's azimuthal position. As the rotor blades rotate, they experience continuously changing wind speeds, which can disrupt optimal power extraction. For instance, blades moving upward through faster wind may generate more lift than blades moving downward through slower wind, creating a vibration or wobble effect. This can limit the turbine's overall efficiency and ability to convert the available power. Figure 31 demonstrates these effects on the power coefficient ( $C_p$ ) of the 15 MW reference turbine at a hub height wind speed of 9 m/s.

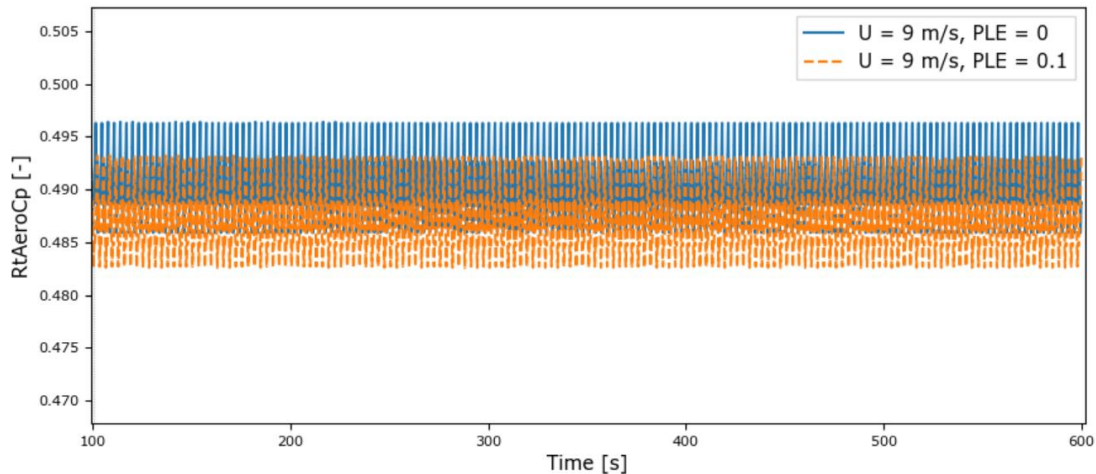


Figure 31: IEA 15-MW turbine's power coefficient at 9 m/s: uniform (blue) vs sheared (yellow)

In an ideal scenario, a wind speed equivalent that capable of accounting for the control mechanism and the aerodynamic shifts due to sheared inflow should yield a power curve unaffected by wind speed shear. This equivalent wind speed would capture the dynamics of the wind profile across the rotor disc, reflecting the real-time changes in wind speed and direction. However, as explained by Wagner et al. (2010), deriving such an equivalent wind speed is a complex task, perhaps impossible. This complexity arises due to the need to fully comprehend the variations in aerodynamics that occur in an inflow environment characterized by vertical shear. Essentially, the aerodynamics of a wind turbine are not merely dictated by the averaged wind speed at the hub height but are influenced by the entire wind profile across the rotor disc, which includes the influence of vertical wind shear.

### **Effects of Turbulence on Wind Turbine Power Production**

The influence of turbulence intensity on the power curve of the 15-MW reference turbine is depicted in Figure 32. A careful examination of the results reveals that turbulence intensity significantly impacts the power output of the wind turbine, but in different ways depending on the wind speed. Specifically, when wind speeds are well below the turbine's rated speed, the power output tends to increase with increasing turbulence. This pattern is expected since at these lower wind speeds, the wind turbine can capture the additional energy generated by the increased turbulence. Given that the power output of a wind turbine is proportional to the cube of the wind speed (refer to Eq. (2.24)), the positive fluctuations in wind speed induced by turbulence result in a significant increase in power. Conversely, the reduction in power associated with the negative fluctuations in wind speed is considerably less impactful.

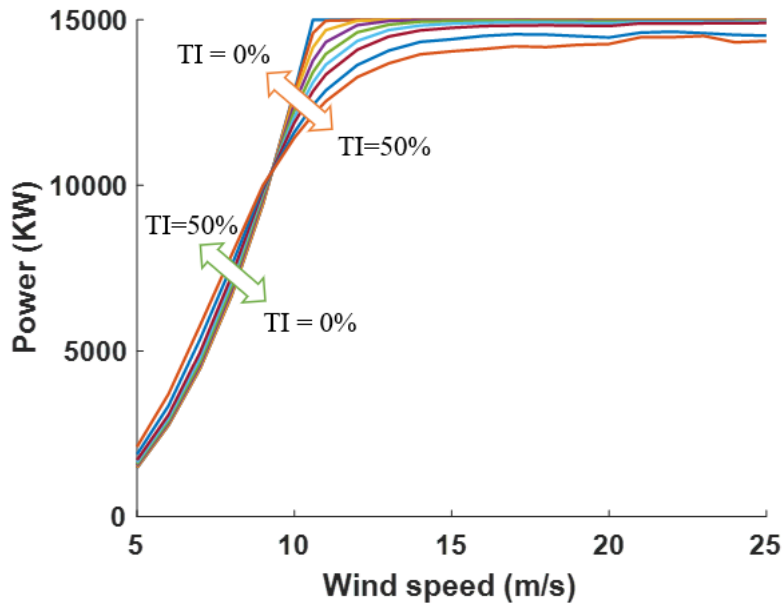


Figure 32: Effects of turbulence intensity on the power curve of the 15MW reference turbine.

However, as the wind speed approaches near to the rated wind speed of the turbine, the relationship between turbulence intensity and power output begins to invert. This shift can be traced back to the influence of turbulence in generating both positive and negative fluctuations in wind speed. When turbulence prompts positive fluctuations, the resulting power generated is limited to the turbine's rated power, irrespective of how much the wind speed exceeds the rated speed. On the other hand, when turbulence promotes negative fluctuations in wind speed, the power output is reduced in line with the cube of the wind speeds. This phenomenon can lead to significant power losses, given the cubic relationship between power and wind speed. Hence, under conditions where the wind speed is near or above the rated speed, turbulence can often lead to an overall reduction in the average power output. Similar results have been recorded in the literature (L. M. Bardal & Sætran, 2017; Dörenkämper et al., 2014; M. C. Holtslag, 2016; Marchena, 2017; Wagner, 2010).

#### 6.4.2. Assessment of Rotor Equivalent Wind Speed Methodology

To assess the applicability of the REWS method in reducing the scatter around a power curve when compared to a simple hub height wind speed, two distinct test scenarios will be considered. The first scenario is built under the assumption of a wind shear profile that follows a constant wind shear exponent. In contrast, the second scenario relies on a wind shear profile that is representative of actual wind speed measurements collected from the Hollandse Kust (Zuid) wind farm.

For each of these cases, the simulated power outputs are used to construct two different power curves. The initial power curve is built based upon the hub height wind speed, while the second is constructed based on the REWS method.

To gauge the effectiveness of the REWS method, the Root Mean Square Error (RMSE) will be used as a key performance metric. This metric quantifies the deviations between

the predictions made by the fitted power curves and the simulated power outputs. A lower RMSE for the REWS power curve, when compared to the hub height wind speed power curve, would indicate that the REWS method is successful in reducing the scatter around the fitted power curve and thus improves the accuracy of the power output predictions.

### Assessment of REWS Method Assuming a Constant Wind Shear Coefficient

OpenFast simulations of the 15-MW reference turbine are used as the primary data source to assess the REWS method's performance. The wind shear profile is characterized by the power law exponent ranging between 0 and 0.3 in alignment with the method used by Wagner et al. (2010). The outcomes of these simulations are used to create two distinct power curves, as depicted in Figure 33.

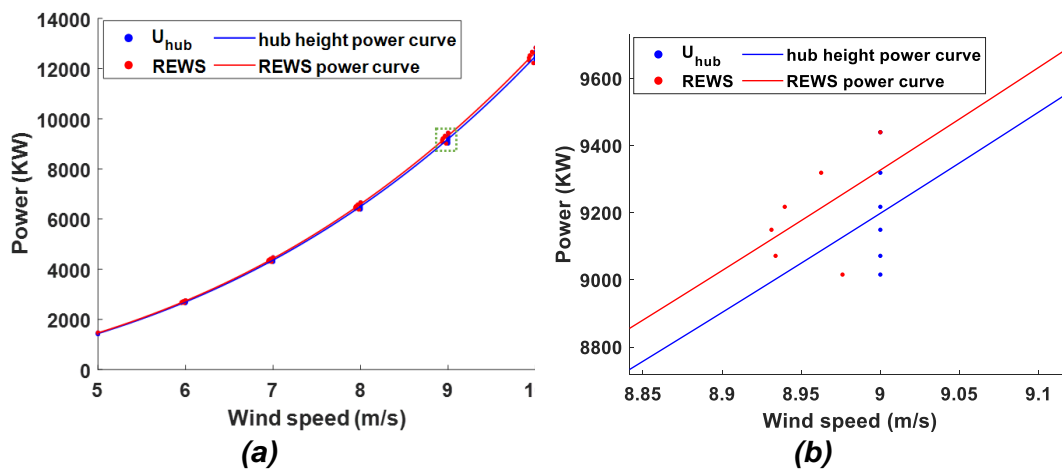


Figure 33: (a), Mean power curve and scatter obtained for two wind speed definitions: the hub height wind speed (blue) and the REWS (red). (b), zoom in of the power curve figure around 9 m/s at hub height

The first power curve, represented by the blue line, corresponds to the power output as a function of the wind speed experienced at the turbine's hub height. In contrast, the second curve, illustrated by the red line, correlates the turbine's power output as a function of the REWS (calculated using Eq. (6.6)). Both power curves are fitted based on the mean values derived from respective wind speed bins and the simulated power outputs.

From Figure 33 (a) & (b), it can be observed that there are minor variations between the two power curves. However, the disparities between these curves appear to increase when the wind speed increases. This observation is expected as the variance of wind speed over the rotor swept area, resulting from wind shear, tends to increase as wind speed increases. For instance, consider a scenario with a fixed power law exponent of 0.1. Under these conditions, when the hub height wind speed is 9 m/s, the wind speed difference between the highest and lowest points of the rotor swept area for the 15-MW turbine is approximately 1.9 m/s. In contrast, when the hub height wind speed drops to 5 m/s, this discrepancy shrinks to around 1 m/s.

To assess the effectiveness of both the REWS method and the hub height wind speed method, Root Mean Square Error (RMSE) values will serve as a performance indicator. The RMSE provides a measure of the differences between values predicted by a

model and the values observed. In the context of this analysis, it quantifies the scatter around the fitted power curves. By comparing the RMSE values obtained from the two methods, one can gauge their relative effectiveness in predicting the power output of a wind turbine.

The findings presented in Table 15 confirm that the REWS method indeed reduces the overall scatter around the fitted power curves compared to the hub height wind speed method for wind shear profiles represented by a constant wind shear coefficient. Quantitatively, the RMSE value saw a decrease from 121 kW when considering the power curve developed using the hub height wind speed method to 103 kW when the REWS method was employed. This signifies an approximately 15% reduction in the scatter, indicating a better fit to the data, and hence an improvement in the predictive power of the model.

*Table 15: Root Mean Square Error (RMSE) values corresponding to power curves fitted using the hub height wind speed method and the rotor equivalent wind speed method. The simulated power outputs are based on fixed wind shear exponents ranging from 0 to 0.3 for each wind speed bin.*

Power curve fitting method	Root Mean Square Error (RMSE)
<b>Hub height wind speed</b>	121 kw
<b>Rotor equivalent wind speed</b>	103 kw

### **Assessment of REWS Method Based on LiDAR Measurements of Hollanse Kust (Zuid) Wind Farm Site**

In real life applications, the wind profile cannot always be represented assuming a constant wind shear coefficient as wind speed can vary greatly over height. Atmospheric stability can play a major role affecting the distribution of wind speeds over heights. For example, during very stable atmospheric conditions, the thickness of the surface boundary layer is reduced which can cause the occurrence of low level jets at heights even below 100 meters (Gutierrez et al., 2016). In such cases, the maximum wind speed may occur at a height level very close to the hub height. An example of this phenomena is depicted in Figure 34, whereas the wind speed is highest close to the hub height level of 150 meters. In such cases, there will be a large scatter around the fitted power curve if one only considers the hub height wind speed. This is where the REWS method could become valuable.

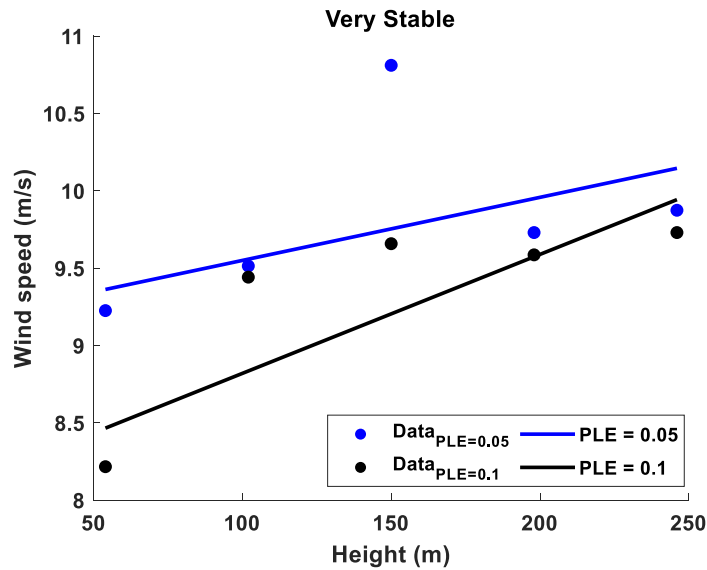


Figure 34: Example of particular instances (10-minute averaged data) where low-level jets occurred at 150 meters height in Hollandse Kust (Zuid) wind farm location. The power law exponent coefficient is calculated based on a linear regression in a  $\log(z)$ - $\log(u)$  scale.

To examine the effectiveness of the REWS method, OpenFast simulations of the 15-MW reference turbine were employed, with the wind shear profile based on actual wind speed measurements at the Hollandse Kust Zuid wind farm (refer to section 6.3.2 for the detailed simulation cases and the criteria used for data selection). These simulation results were then used to construct two separate power curves, as demonstrated in Figure 35. The power curves were developed employing a least squares polynomial regression of the third degree for a well-fitted curve.

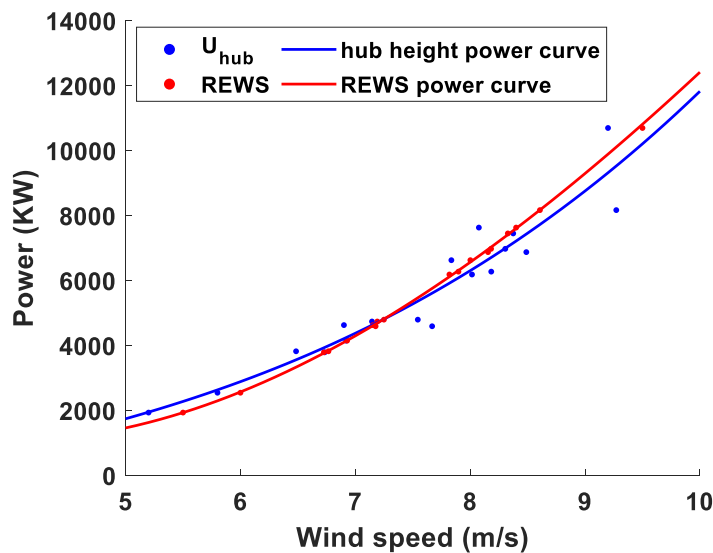


Figure 35: power curve and scatter obtained for two wind speed definitions: the hub height wind speed (blue) and the REWS (red).

A critical analysis of the results, as illustrated in Figure 35, reveal a noticeable increase in scatter when the hub height wind speed is utilized compared to the REWS. This validates the capability of the REWS method in reducing the scatter around the power curve, especially for large wind turbines. Given their size, these turbines can

encounter a variety of wind conditions across different heights, which in turn influences their power output. With traditional methods relying solely on hub height wind speed, this variability is often under-represented, which can lead to inaccurate power curve estimation.

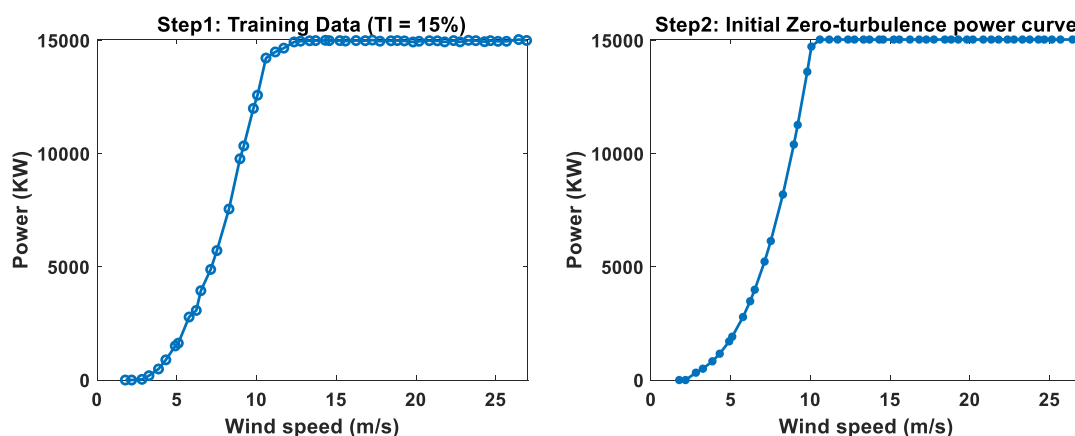
The results presented in Table 16 confirm that the REWS method significantly reduced the overall scatter around the fitted power curves, compared to using the hub height wind speed method. This is particularly apparent when dealing with wind shear profiles that display variations across different heights. The RMSE decreases significantly from 767 kW when utilizing the hub height wind speed method, to 47 kW when employing the REWS method. This dramatic reduction in RMSE signifies an improved fit of the model to the data and, consequently, an enhancement in its predictive power. In other words, the REWS method in this test case scenario is expected to improve the accuracy of power output predictions, especially in an environment with variable wind shear profiles.

Table 16: Root Mean Square Error (RMSE) values corresponding to power curves fitted using the hub height wind speed method and the rotor equivalent wind speed method. The simulated power outputs are based on potential variations in the wind shear profile based on semi-random selections of data obtained from Hollanse Kust (Zuid) wind farm

Power curve fitting method	Root Mean Square Error (RMSE)
Hub height wind speed	767 kw
Rotor equivalent wind speed	47 kw

### 6.4.3. Assessment of Turbulence Renormalization Methodology

To test the applicability of the turbulence renormalization method, two sets of data have been acquired through simulations and turbulence renormalization is applied for each case. The first data set is simulated based on a TI value of 15% and the second data set is based on a TI value of 5%. Figure 36 depicts a stepwise process of renormalizing the 15% TI power curve to predict the power curve at a TI level of 5%.



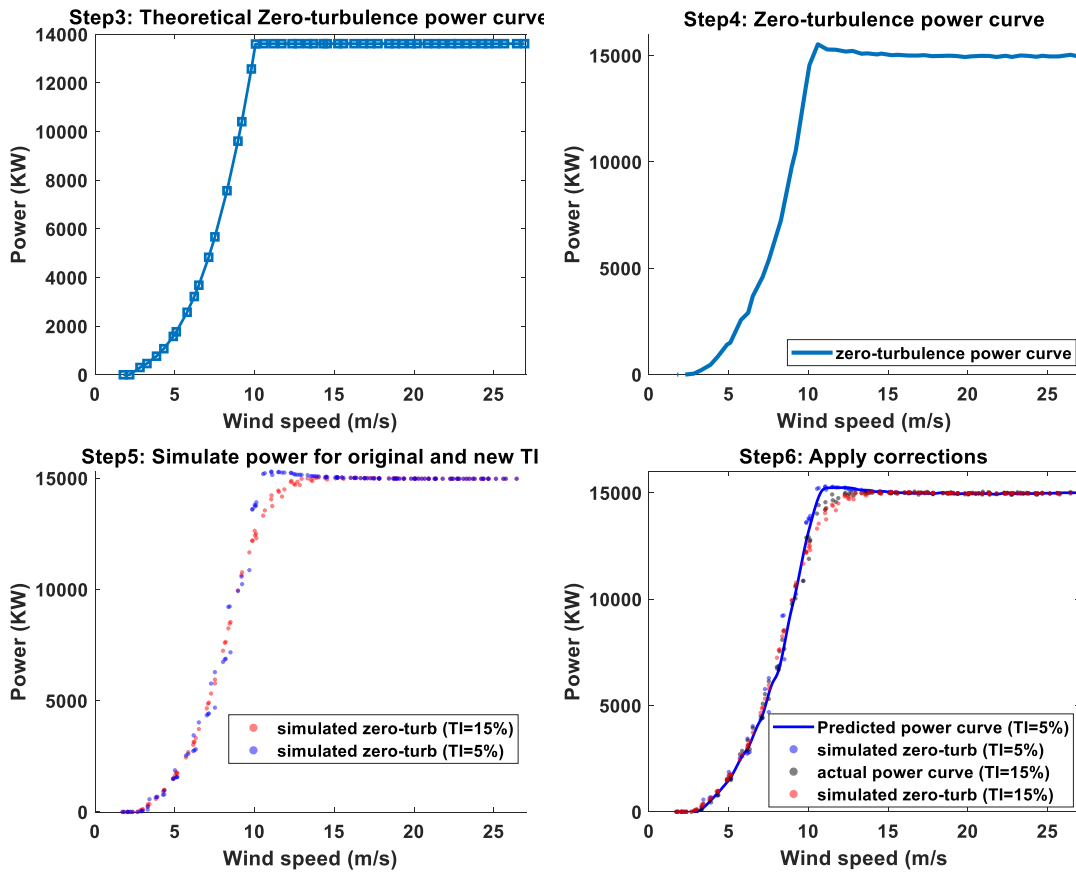


Figure 36: Stepwise figures of applying turbulence renormalization method

The results, as depicted in Figure 37, suggest that the turbulence renormalization method may tends to overestimate turbulence effects. When a power curve with high turbulence is used to estimate a power curve with low turbulence (as illustrated in Figure 37 (a)), the method seems to overestimate power production, particularly in wind speed regions near the rated wind speed. Conversely, when the method is applied in the reverse direction, transitioning from a scenario with low turbulence intensity (TI) to a high TI (as illustrated in Figure 37 (b)), power output appears to be underestimated. These observations align with the results of Clifton and Wagner's (2014), however, they contrast the results of Bardal and Sætran (2017), which reported power being underestimated in both case scenarios.

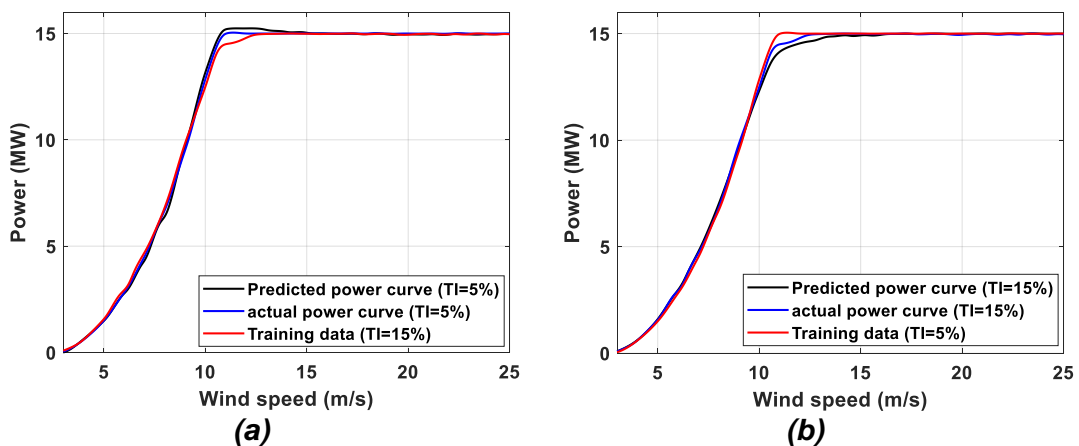


Figure 37: Estimated power curve using TI=15% power data to simulate TI=5% power curve (a) and estimated power curve using TI=5% power data to simulate TI=15% power curve (b)

To verify the accuracy of the turbulence renormalization method, the annual energy production (AEP) for the 15-MW reference turbine will be estimated using the probability distribution function presented in Figure 6 (b) along with the power curves presented in Figure 37. For each wind speed bin size of 1 m/s, the probability of occurrence is multiplied by their respective power output obtained from each power curve. To translate these values into an annual context, they are further multiplied by the total number of hours in a year.

In general, it was found that the predicted power using the turbulence renormalization method provided better predictions than the original non-renormalized power curve. The results showed that the predicted power curve at a TI level of 5% (see Figure 37 (a)) overestimated the AEP by a factor of 1%, whereas the original non-renormalized power curve (training data) underestimated the AEP by a factor of 1.9%. For the second case scenario (see Figure 37 (b)), the predicted power curve at a TI level of 15% underestimated the AEP by a factor of 1.1%, whereas the original non-renormalized power curve overestimated the AEP by a factor of 2.1%.

It is also observed from Figure 37 that the accuracy of the turbulence renormalization method is decreased close to the rated wind speed. Therefore, one might question if the process of turbulence renormalization can be improved to provide better predictions of the power output.

The last step in the turbulence renormalization method (refer to section 6.3.2) involves applying a correction formula as follows:

$$P_s(k) = P(k) + \hat{P}_s(k) - \hat{P}(k) \quad (6.7)$$

Where  $P(k)$  is the measured power output of the training data,  $\hat{P}_s(k)$  is the simulated power output of the new predicted power curve, and  $\hat{P}(k)$  is the simulated power output of the training data.

It is possible that Eq. (6.7) could be readjusted to obtain a better prediction of the power curve. The following formula is proposed:

$$P_s(k) = P(k) + x \left( \hat{P}_s(k) - \hat{P}(k) \right) \quad \text{where } 0 \leq x \leq 1 \quad (6.8)$$

For wind speeds ranging from 5 m/s to 15 m/s with a wind speed bin of 0.5 m/s, the RMSE value is calculated based on the differences between predicted power curve and the actual power curve for values of  $x$  ranging from 0 to 1 in a 0.1 interval. For both two test cases shown in Figure 37, it was found that the RMSE value is minimized when the value of  $x$  is close to 0.5. Therefore, the following correction formulas is proposed:

$$P_s(k) = P(k) + \frac{1}{2} \left( \hat{P}_s(k) - \hat{P}(k) \right) \quad (6.9)$$

The results presented in Figure 38 show a major improvement when the new correction formula is applied as opposed to the one used by (Albers et al., 2007; L. M. Bardal & Sætran, 2017; Clifton & Wagner, 2014). In terms of AEP estimation, the error of the predicted power curve at a TI level of 5% (Figure 38 (a)) is reduced from 1% to 0.5%,

whereas the error of the predicted power curve at a TI level of 15% (Figure 38 (a))) is reduced from 1.1% to 0.5%.

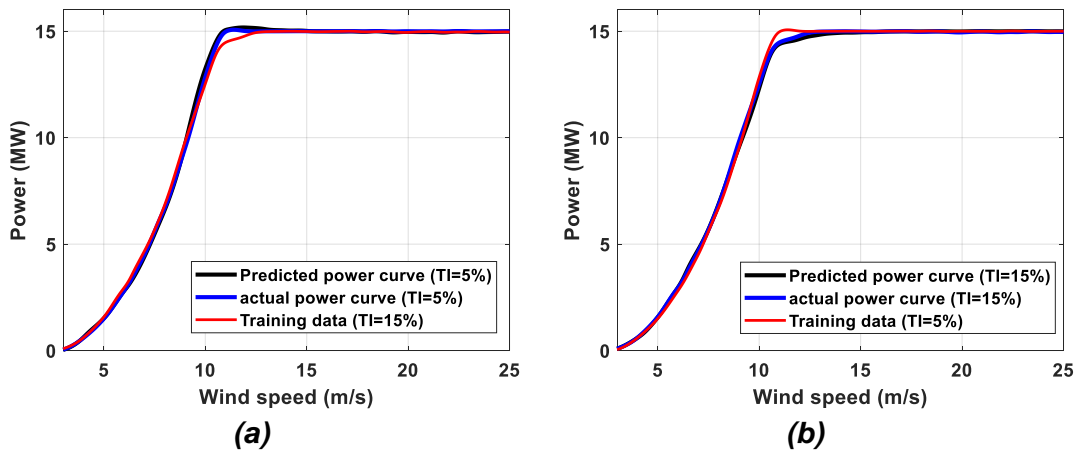


Figure 38: Estimated power curve using TI=15% power data to simulate TI=5% power curve (a) and estimated power curve using TI=5% power data to simulate TI=15% power curve (b). The correction formula proposed in Eq. (6.9) is followed

However, the validity of Eq. (6.9) may be questionable under different atmospheric conditions. To test this, simulations based on data obtained from Hollandse Kust (Zuid) wind farm are used to generate two power curves for the IEC 15-MW reference turbine under two distinct atmospheric conditions; very stable and very unstable (refer to Chapter 3.3.1). Using the turbulence renormalization method, the power curve developed under very stable atmospheric conditions will be used to estimate a new power curve that should represent the performance of the wind turbine under very unstable conditions. The original correction formula (Eq. (6.7)) and the new correction formula (Eq. (6.9)) will both be applied to validate their accuracy.

Following the method depicted in section 6.3.3, a zero-turbulence power curve is created using the power curve data developed under very stable atmospheric conditions as shown in Figure 39 (a). The zero-turbulence power curve is used to estimate a new power curve representing very unstable atmospheric condition. Clifton and Wagner’s (2014) correction formula (Eq. (6.7)) is applied on Figure 39 (b), and the new correction formula (Eq. (6.9)) is applied on Figure 39 (c).

It should be noted that the power curves shown in Figure 39 are smoothed using matlab’s Smoothing Spline function, with a default smoothing parameter of 0.99. The reason for doing so is to reduce the noise caused by the binning mechanism. A similar approach was adopted by Albers et al. (2007) using Newton solver.

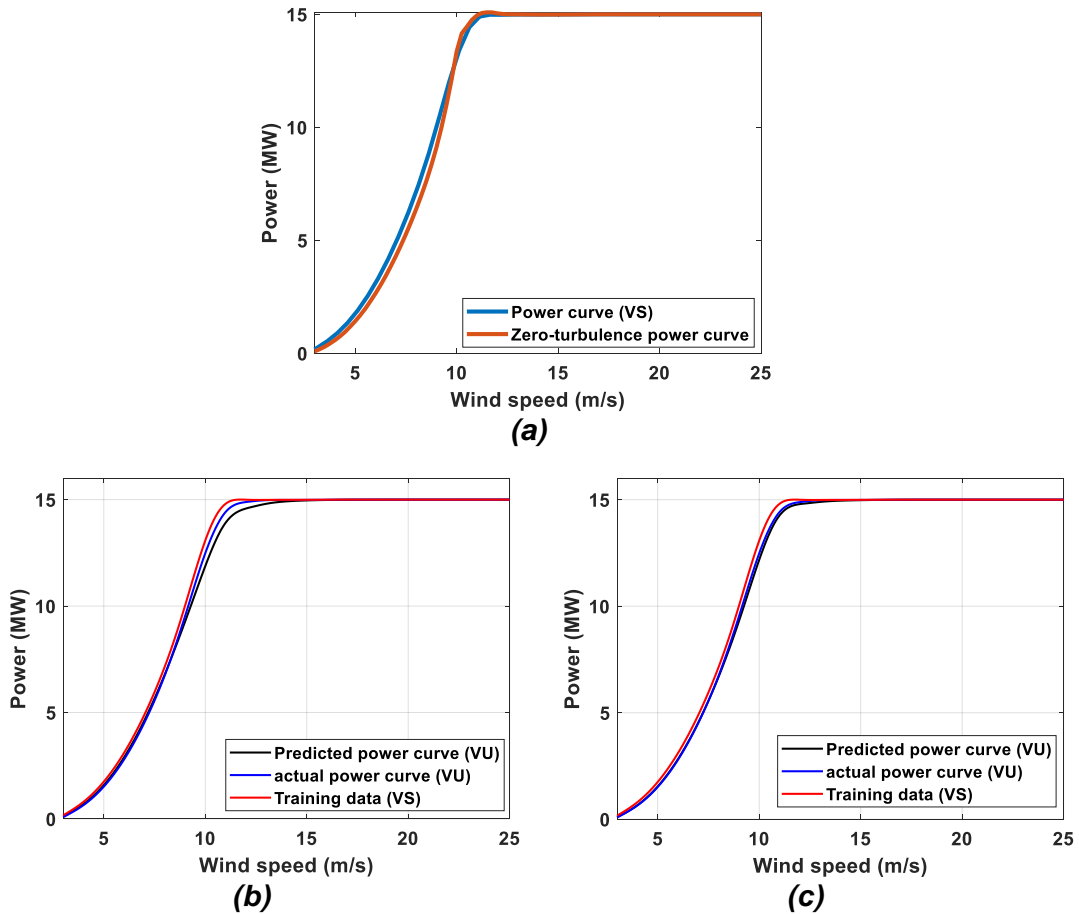


Figure 39: (a): zero turbulence power curve based on data representing very stable atmospheric conditions. (b): Estimated power curve during very unstable conditions using Clifton and Wagner's (2014) correction formula (Eq. (6.7)). (c): Estimated power curve during very unstable conditions by applying the new correction formula (Eq. (6.9)). The power curves are smoothed using a smoothing parameter of 0.99 to reduce the noise caused by the binning mechanism

To evaluate the accuracy of the turbulence renormalization method, the annual energy production (AEP) during very unstable conditions is estimated based on four different cases. First, the actual power curve representing very unstable (VU) conditions will be considered. This will be considered the baseline for comparison. Second, using the original power curve measured during very stable (VS) atmospheric conditions which is the training data set. Third, using the estimated power curve, corrected per Clifton and Wagner's (2014) method (Eq. (6.7)). Lastly, using the estimated power curve, corrected using Eq. (6.9). The Weibull distribution parameters presented in Figure 6 (b) are used to estimate the AEP for all different cases.

The results showed that when compared to the baseline, using the training data set (measured during very stable atmospheric conditions) showed to overestimate the AEP by a factor of 2.6%. However, when considering estimated power curve using Clifton and Wagner's (2014) method, the AEP is underestimated by a factor of 1.3%. The best results were found using the estimated power corrected per Eq. (6.9). This resulted in an underestimation of the AEP by a factor of 0.7%.

Though these results appear to be promising, it is acknowledged that these findings were based on simulations with only limited data points used to validate the turbulence

renormalization model. Therefore, future verifications need to be done in accordance to actual site power measurements.

## 6.5. Discussion and Conclusion

Accurate energy yield prediction is critical in wind resource assessment. It provides insights into a wind energy project's feasibility and profitability, guiding investors' decisions. The prediction of annual energy production (AEP) necessitates careful attention to the ways site-specific atmospheric conditions can influence the power curve of wind turbines.

This chapter therefore explored the influence of wind shear and turbulence intensity on the power output of wind turbines, focusing on the 15MW reference turbine. To incorporate the effects of wind shear and turbulence into a site-specific power curve, this study evaluated two methods - the Rotor Equivalent Wind Speed (REWS) and turbulence renormalization methods.

The impact of wind shear on the power output of a wind turbine was first examined. In general, wind shear causes a variation in wind speed across the rotor swept area of a wind turbine, leading to differences in power output when compared to a uniform inflow at the same hub height wind speeds. Theoretical expectations suggest that the change in a wind turbine's power production should resemble the variation in the wind's kinetic energy flux, a function of the Power Law Exponent (PLE). However, it was observed that the actual change in power production does not consistently follow this theoretical expectation and additional losses were found. This discrepancy can be attributed to factors such as the control strategy employed by the wind turbine and the limitations imposed by wind shear on power extraction efficiency. As explained by Wagner et al. (2010), wind shear introduces a cyclical variation in inflow conditions, which correlates with the rotor's azimuthal position. As the rotor blades rotate, they experience continuously changing wind speeds, which can disrupt optimal power extraction. For instance, blades moving upward through faster wind may generate more lift than blades moving downward through slower wind, creating a vibration or wobble effect which can limit the turbine's overall efficiency and ability to convert the available power.

This study also explored the effects of turbulence on the power production of a wind turbine. Theoretically, turbulence increases the wind's kinetic energy flux and thereby should increase the power output of a wind turbine (Wagner, 2010). However, it was found the effects of turbulence on wind turbine power production are closely related to the control mechanism of a wind turbine. At wind speeds well below the turbine's rated speed, an increase in turbulence corresponds to an increase in power production. This is because, at these lower speeds, the wind turbine can leverage the extra energy induced by higher turbulence. Since the power output of a wind turbine is cubically proportional to the wind speed, the increase in power due to positive fluctuations in wind speed, induced by turbulence, substantially outweighs the reduction in power from negative fluctuations. However, as the wind speed draws closer to the rated speed of the turbine, the relationship between turbulence intensity and power output inverts. This is because When turbulence prompts positive fluctuations, the resulting

power generated is limited to the turbine's rated power, irrespective of how much the wind speed exceeds the rated speed. On the other hand, when turbulence promotes negative fluctuations in wind speed, the power output is reduced in line with the cube of the wind speeds. Hence, under conditions where the wind speed is near or above the rated speed, turbulence can often lead to an overall reduction in the average power output.

In order to incorporate the effects of wind shear into a site-specific power curve, the use of the REWS has been validated. The results indicate that the REWS method generally reduced the scatter around the power curve which should theoretically provide better predictions of the power output than a simple hub height wind speed. Under the assumption that the wind shear profile follows a constant wind shear coefficient, the differences between the two methods were not quite significant. This is in line with the findings of Wagner et al. (2010), Redfern et al. (2019), and van Sark et al. (2019). However, for a non-constant wind shear profile with a shear coefficient that changes over height, it was found that the REWS method significantly reduced the scatter around the power curve which in return should improve the accuracy of the estimated AEP. This aligns well with the findings of Redfern et al. (2019), however, deviate from the results of van Sark et al. (2019) which suggests insignificant difference between REWS and hub height wind speed for energy yield predictions.

The differences in results could be attributed to two factors. First, the size of a wind turbine is an important factor which is to be considered. Large capacity wind turbines can experience different wind profiles over their rotor swept area. For example, during very stable conditions in offshore locations, low level jets can occur at a height of 100 meters (Gutierrez et al., 2016). In such cases, the lower part of the rotor swept area would experience the surface layer wind profile, whereas higher parts can experience low level jets or even geostrophic winds. This in return creates a scatter of strong non-linear shear profile which its effects on power production cannot be captured using a simple hub height wind speed. The second factor could be attributed to the site locations. The study conducted by Wagner et al. (2010) showed a clear reduction in the scatter around the fitted power curve when using REWS, however, in a later study (Wagner et al., 2014), no clear reduction in scatter was observed. It was concluded based on their results that the differences between REWS and hub height wind speed are site dependent.

This study then validated the turbulence renormalization method introduced by Albers et al. (2007). The method was found to generally underestimates the Annual Energy Production (AEP) when transitioning from low to high turbulence environments, and overestimates in the reverse direction. The results are consistent with Clifton and Wagner (2014) but oppos Bardal and Sætran's (2017) who found consistent underestimation of AEP in both case scenarios. The reason for these contradictory results is uncertain. However, both studies showed an improvement in AEP accuracy when using the turbulence renormalization method, which is in line with the results of this study. Much like the findings of Bardal and Sætran (2017), the results of this study showed on average 1% reduction in the AEP error when using the turbulence renormalization method as oppos to using the original non-renormalized power curve.

The study also proposed an enhancement to the turbulence renormalization method by optimizing the correction approach detailed by Clifton and Wagner (2014), aiming to achieve the lowest Root Mean Square Error (RMSE) value. This optimization yielded an average additional 0.5% reduction in AEP error. However, it is important to note that the findings were based on simulations, with limited data points used for validation. Consequently, future verification of the optimization approach should be pursued in accordance with actual site power measurements.

In summary, this study demonstrated that both the rotor equivalent wind speed and turbulence renormalization methods can enhance the accuracy of power output predictions for large-scale wind turbines. However, it is crucial to note that typically these methods are applied using real-world turbine power output data. In this research, due to the difficulty in acquiring such data, a simulation approach was employed instead. Therefore, further validations of these methods, using real-world data from large-scale turbines, are still necessary. As of the time of this report, there are no known studies that have validated these methods against real-world data for wind turbines exceeding 3.6 MW in capacity. Therefore, it is recommended that future studies aim to validate these methods using data collected from large-scale wind turbines. This is particularly applicable for the REWS method, given that large-scale wind turbines can experience a broad range of wind conditions that extend beyond just the surface boundary layer.

# Chapter 7. Conclusions and Recommendations

This final chapter encapsulates the core findings of this research. The narrative of this chapter is organized in a way that initially provides a broad overview of the conclusions, which are then elaborated in three distinctive sections corresponding to the thematic research areas. The chapter concludes in a set of recommendations, drawing from the gained insights to propose potential directions for future work.

## 7.1. Conclusion

The core of this research resided in the comprehensive exploration of the complex dynamics of wind resource and fatigue loads assessment, with a focus on the influences of atmospheric conditions. Considering the complex variables of wind shear, turbulence intensity, and the interaction between the two, the study sought to validate existing methodologies, with the ultimate aim of enhancing the accuracy of wind resource assessments.

### 7.1.1. Analysis of Offshore Wind Conditions

The field measurements from the Hollandse Kust Zuid, though reaching a maximum of 200 meters, do not necessarily cover the heights of new large-capacity wind turbines. As the wind profile does not always follow the power law or the logarithmic law due to its dependence on atmospheric stability, the extrapolation of wind speeds beyond the measured data is an important topic to be explored.

Upon validating multiple stability correction functions against the actual site measurement data, it was observed that the performance of each extrapolation model is heavily influenced by the atmospheric conditions. Particularly, the free convection (FC) and Businger-Dyer (BD) stability correction functions worked well during strong unstable atmospheric conditions. However, under modern instability, it was found that the observed mean shear profile falls between the logarithmic law and the stability corrected logarithmic law (FC & BD), with the latter proving more accurate as instability increases. These findings held true regardless of the starting point of the extrapolation process.

Interestingly, the accuracy of each extrapolation models during stable and very stable atmospheric conditions demonstrated a dependency on the starting point of extrapolation. When extrapolating the wind speed from a height of 100 meters to higher altitudes, the logarithmic law generally performed best under very stable atmospheric conditions, whereas the power law provided superior results in stable atmospheric conditions. However, when extrapolating wind speed from a lower height of 30 meters to high altitudes, the power law proved generally more accurate during stable and very

stable atmospheric conditions, though its performance varied based on the height to which it was extrapolated.

In conditions nearing neutral stability, both Brutsaert and Businger-Dyer stability correction functions provided the best results. In contrast, under conditions that were nearing unstable neutrality, the wind shear profile was best expressed as a function of the logarithmic law.

### **7.1.2. Analysis of Fatigue Loads in Relation to Site-Specific Atmospheric Conditions**

In examining the effects of atmospheric conditions on wind turbine loads, this research was driven by specific key questions: How do wind shear and turbulence influence fatigue loads on a wind turbine? are there any interaction between wind shear and turbulence in the context of fatigue load assessment? How can site-specific fatigue loads be determined while ensuring computational efficiency? With a particular emphasis on the fatigue loads experienced at the wind turbine blade root in the flapwise direction, comprehensive data analysis and aeroelastic simulations have been carried out to explore these inquiries, leading to several key findings.

The results of this study have indicated that turbulence intensity and the Power Law Exponent (PLE) play a critical role in influencing the fatigue loads experienced by wind turbines, specifically at the blade root in the flapwise direction. The turbulence intensity, in particular, exhibited a near-linear relationship with fatigue loads, consistent with previous studies (Slot et al., 2018; Veldkamp, 2007). However, the relationship between the PLE and fatigue loads presented a more nuanced picture. It was found that the relationship between these two variables can be linear or quadratic, depending on the range of PLE values and the specific wind speed conditions. Furthermore, the study delved into the interactive dynamics between wind shear and turbulence. The research found that their combined influence on fatigue loads was not simply additive, but rather involved complex interactions that could either amplify or diminish the individual effects of these factors.

For the purpose of calculating site-specific fatigue loads while retaining computational efficiency, the response surface methodology (RSM) with a central composite design, as proposed by Toft et al. (2016), was adopted. This methodology incorporates a linear regression model, including an interaction term, to account for the effects of interactions between the climate parameters on fatigue loads. While this approach proved effective, it displayed limitations in capturing regions where a non-linear relationship between the Power Law Exponent (PLE) and fatigue loads occurs.

Addressing this limitation, the research proposed and tested a modified version of the central composite design. This novel approach retains the linear regression model for areas where the relationship between PLE and fatigue loads is linear but incorporates a quadratic regression model for regions characterized by non-linearity. Although the modified approach demonstrated a higher degree of accuracy during validation against an artificial site, the differences between the results obtained from both methods were

marginal when applied to actual wind farm site conditions. This outcome suggests that the benefits of the modified central composite design might not justify the additional computational costs it incurs in every situation.

### **7.1.3. Power Production in Relation to Atmospheric Conditions**

This section of the research addressed the question: How do wind shear and turbulence factor into the projected annual energy output of a wind turbine? Specifically, it delves into the ways in which wind shear and turbulence influence the power production of large wind turbines, and how these effects can be integrated into a site-specific power curve.

Investigations into the effects of wind shear on a wind turbine's power output reveal key observations. Wind shear is known to cause variations in wind speed across the rotor swept area of a wind turbine, leading to power output differences when compared to uniform inflow at the same hub height wind speeds. Notably, wind shear causes changes in the wind's kinetic energy flux, typically resulting in reduced energy when the power law exponent (PLE) is less than 1/3. However, actual variations in a wind turbine's power production exceed this decrease in kinetic energy flux. This excess loss can be attributed to several factors, such as the control strategy employed by the wind turbine and the limitations that wind shear imposes on power extraction efficiency. As an example, the effects of wind shear introduce cyclic variations in inflow conditions that correspond with the rotor's azimuthal position. As rotor blades rotate, they encounter continuously varying wind speeds, which can disrupt optimal power extraction and further limit the turbine's overall efficiency.

The turbulence influence on wind turbine power production was also assessed. Theoretically, turbulence contributes to an increase in the wind's kinetic energy flux, and by extension, should lead to a rise in the wind turbine's power output. However, the impact of turbulence on wind turbine power production is closely linked with the turbine's control mechanism. An increase in turbulence generally elevates power production at wind speeds well below the turbine's rated speed. This changes as the wind speed approaches the rated speed, where the relationship between turbulence intensity and power output inversely correlates, often leading to an overall reduction in the average power output.

To integrate the effects of wind shear and turbulence into a site-specific power curve, this study evaluated two methods - the Rotor Equivalent Wind Speed (REWS) and turbulence renormalization. The results indicate that the REWS method generally reduced the scatter around the power curve which should theoretically provide better predictions of the power output than a simple hub height wind speed. Under the assumption that the wind shear profile follows a constant wind shear coefficient, the differences between the two methods were not quite significant. However, for a non-constant wind shear profile with a shear coefficient that changes over height, it was found that the REWS method significantly reduced the scatter around the power curve which in return should improve the accuracy of the estimated AEP.

The turbulence renormalization method, also known as the zero-turbulence power curve method, was validated in this study. Generally, this method was found to underestimate the AEP when transitioning from low to high turbulence environments, and overestimate in the reverse transition. Nevertheless, it resulted in around 1% error reduction in the AEP when compared to the original non-renormalized power curve.

An enhancement to the turbulence renormalization method was also proposed in this study. By optimizing the correction approach detailed by Clifton and Wagner (2014) with an aim to achieve the lowest Root Mean Square Error (RMSE) value, the optimization process resulted in an average additional 0.5% reduction in AEP error. It is important to note, however, that these findings were based on simulations, with a limited set of data points used for validation. Consequently, future verification of the optimization approach should be pursued in accordance with actual site power measurements to validate these findings in real-world scenarios.

## 7.2. Recommendations

The findings of this research pave the way for a series of potential future investigations and improvements. Here are the key recommendations:

- **Extension of Wind Shear Profile:** The understanding of wind profiles at varying atmospheric stabilities is still incomplete, especially beyond the surface boundary layer. This lack of data becomes increasingly crucial as the sizes of wind turbines grow, with blade tips which can reach beyond available measurements. Therefore, further research and development are recommended to create comprehensive models that can accurately represent the wind shear profile, even beyond the surface boundary layer. Such models should be extensively validated against real-world measurements to ensure reliability.
- **Site-Specific Fatigue Load Assessment:** This study has underlined the effectiveness of the response surface methodology using the central composite design for analyzing site-specific fatigue loads. However, its applicability under complex terrains has not yet been validated. Therefore, future research could evaluate its effectiveness in fatigue load assessment for wind turbine sites with very atypical wind conditions
- **Site-Specific Power Curves:** This study examined the efficacy of the turbulence renormalization method as an instrument for creating site-specific power curves. While this method has shown promise in enhancing the accuracy of the power curve, there remains significant potential for further optimization. It is recommended that future research focus on refining this method, specifically using real-world power measurements to further refine and validate the approach. Moreover, further validation of the REWS method is needed based on actual power measurements of large-scale wind turbines. There are still contradicting opinions in the literature pertaining to the validity of this method. However, as of the time of this report, there are no known studies that

have validated this method against real-world data for wind turbines exceeding 3.6 MW in capacity. Finally, the application of the response surface methodology, using the central composite design, is another promising area for future exploration in terms of adjusting wind turbine power curves to reflect a site-specific environment. Comparing the results of this methodology to the turbulence-renormalization method could provide additional insights and potentially lead to further advancements in the creation of more accurate site-specific power curves.

## References

- Albers, A., Jakobi, T., Rohden, R., & Stoltenjohannes, J. (2007). Influence of meteorological variables on measured wind turbine power curves. *European Wind Energy Conference and Exhibition 2007, EWEC 2007*, 3.
- Bailly, C., & Comte-Bellot, G. (2015). Introduction to Turbulence. In C. Bailly & G. Comte-Bellot (Eds.), *Turbulence* (pp. 1–31). Springer International Publishing.  
[https://doi.org/10.1007/978-3-319-16160-0\\_1](https://doi.org/10.1007/978-3-319-16160-0_1)
- Bardal, L. M., & Sætran, L. R. (2017). Influence of turbulence intensity on wind turbine power curves. *Energy Procedia*, 137, 553–558.  
<https://doi.org/10.1016/j.egypro.2017.10.384>
- Bardal, L., Sætran, L., & Wangsness, E. (2015). Performance Test of a 3MW Wind Turbine – Effects of Shear and Turbulence. *Energy Procedia*, 80, 83–91.  
<https://doi.org/10.1016/j.egypro.2015.11.410>
- Beljaars, A. C. M., & Holtslag, A. a. M. (1991). Flux Parameterization over Land Surfaces for Atmospheric Models. *Journal of Applied Meteorology and Climatology*, 30(3), 327–341. [https://doi.org/10.1175/1520-0450\(1991\)030<0327:FPOLSF>2.0.CO;2](https://doi.org/10.1175/1520-0450(1991)030<0327:FPOLSF>2.0.CO;2)
- Bilgili, M., Tumse, S., Tontu, M., & Sahin, B. (2021). Effect of Growth in Turbine Size on Rotor Aerodynamic Performance of Modern Commercial Large-Scale Wind Turbines. *Arabian Journal for Science and Engineering*, 46(8), 7185–7195. <https://doi.org/10.1007/s13369-021-05364-6>
- Box, G. E. P., & Wilson, K. B. (1951). On the Experimental Attainment of Optimum Conditions. *Journal of the Royal Statistical Society: Series B (Methodological)*, 13(1), 1–38. <https://doi.org/10.1111/j.2517-6161.1951.tb00067.x>
- Brutsaert, W. (1982). *Evaporation into the Atmosphere*. Springer Netherlands.  
<https://doi.org/10.1007/978-94-017-1497-6>

- Burton, T. (Ed.). (2001). *Wind energy: Handbook*. J. Wiley.
- Businger, J. A., Wyngaard, J. C., Izumi, Y., & Bradley, E. F. (1971). Flux-Profile Relationships in the Atmospheric Surface Layer. *Journal of the Atmospheric Sciences*, 28(2), 181–189. [https://doi.org/10.1175/1520-0469\(1971\)028<0181:FPRITA>2.0.CO;2](https://doi.org/10.1175/1520-0469(1971)028<0181:FPRITA>2.0.CO;2)
- Carl, D. M., Tarbell, T. C., & Panofsky, H. A. (1973). Profiles of Wind and Temperature from Towers over Homogeneous Terrain. *Journal of the Atmospheric Sciences*, 30(5), 788–794. [https://doi.org/10.1175/1520-0469\(1973\)030<0788:POWATF>2.0.CO;2](https://doi.org/10.1175/1520-0469(1973)030<0788:POWATF>2.0.CO;2)
- Clifton, A., & Wagner, R. (2014). Accounting for the effect of turbulence on wind turbine power curves. *Journal of Physics: Conference Series*, 524, 012109. <https://doi.org/10.1088/1742-6596/524/1/012109>
- Cooperman, A., & Martinez, M. (2014). Load monitoring for active control of wind turbines. *Renewable and Sustainable Energy Reviews*, Vol. 41, 189–201. <https://doi.org/10.1016/j.rser.2014.08.029>
- Dörenkämper, M., Tambke, J., Steinfeld, G., Heinemann, D., & Kühn, M. (2014). Atmospheric Impacts on Power Curves of Multi-Megawatt Offshore Wind Turbines. *Journal of Physics: Conference Series*, 555(1), 012029. <https://doi.org/10.1088/1742-6596/555/1/012029>
- Dyer, A. J. (1974). A review of flux-profile relationships. *Boundary-Layer Meteorology*, 7(3), 363–372. <https://doi.org/10.1007/BF00240838>
- Eecen, P. J., & Machielse, L. A. H. (n.d.). *Meteorological Measurements OWEZ*. 47.
- Fairall, C. W., Bradley, E. F., Godfrey, J. S., Wick, G. A., Edson, J. B., & Young, G. S. (1996). Cool-skin and warm-layer effects on sea surface temperature. *Journal of Geophysical Research: Oceans*, 101(C1), 1295–1308. <https://doi.org/10.1029/95JC03190>
- Fairall, C. W., Bradley, E. F., Rogers, D. P., Edson, J. B., & Young, G. S. (1996). Bulk parameterization of air-sea fluxes for Tropical Ocean-Global Atmosphere

- Coupled-Ocean Atmosphere Response Experiment. *Journal of Geophysical Research: Oceans*, 101(C2), 3747–3764. <https://doi.org/10.1029/95JC03205>
- Fugro. (2018). *Hollandse Kust (zuid) Field Measurement Campaign*.  
[https://offshorewind.rvo.nl/file/download/f23c4b90-a840-48b1-a055-1db4b6218644/hkz\\_20181024\\_fugro\\_tno\\_metocean-campaign-report-june-2016-june-2018-f.pdf](https://offshorewind.rvo.nl/file/download/f23c4b90-a840-48b1-a055-1db4b6218644/hkz_20181024_fugro_tno_metocean-campaign-report-june-2016-june-2018-f.pdf)
- Gaertner, E., Rinker, J., Sethuraman, L., Zahle, F., & IEC. (2022). *Definition of the {IEA} 15-Megawatt Offshore Reference Wind Turbine*.  
<https://github.com/IEAWindTask37/IEA-15-240-RWT>
- Grachev, A. A., & Fairall, C. W. (1997). Dependence of the Monin–Obukhov Stability Parameter on the Bulk Richardson Number over the Ocean. *Journal of Applied Meteorology and Climatology*, 36(4), 406–414.  
[https://doi.org/10.1175/1520-0450\(1997\)036<0406:DOTMOS>2.0.CO;2](https://doi.org/10.1175/1520-0450(1997)036<0406:DOTMOS>2.0.CO;2)
- Greaves, P. (2023). *Rainflow Count (for Wind Turbine Calculations)*.  
<https://www.mathworks.com/matlabcentral/fileexchange/81588-rainflow-count-for-wind-turbine-calculations>
- Gryning, S.-E., Batchvarova, E., Brümmer, B., Jørgensen, H., & Larsen, S. (2007). On the extension of the wind profile over homogeneous terrain beyond the surface boundary layer. *Boundary-Layer Meteorology*, 124(2), 251–268.  
<https://doi.org/10.1007/s10546-007-9166-9>
- Gutierrez, W., Araya, G., Kiliyanpilakkil, P., Ruiz-Columbie, A., Tutkun, M., & Castillo, L. (2016). Structural impact assessment of low level jets over wind turbines. *Journal of Renewable and Sustainable Energy*, 8(2), 023308.  
<https://doi.org/10.1063/1.4945359>
- Högström, U. (1988). Non-dimensional wind and temperature profiles in the atmospheric surface layer: A re-evaluation. *Boundary-Layer Meteorology*, 42(1), 55–78. <https://doi.org/10.1007/BF00119875>

- Holtslag, A. a. M., & Bruin, H. A. R. D. (1988). Applied Modeling of the Nighttime Surface Energy Balance over Land. *Journal of Applied Meteorology and Climatology*, 27(6), 689–704. [https://doi.org/10.1175/1520-0450\(1988\)027<0689:AMOTNS>2.0.CO;2](https://doi.org/10.1175/1520-0450(1988)027<0689:AMOTNS>2.0.CO;2)
- Holtslag, M. C. (2016). *Far offshore wind conditions in scope of wind energy*. <https://doi.org/10.4233/uuid:3c66f401-6cff-4273-aa49-df4274ba767f>
- Holtslag, M. C., Bierbooms, W. a. a. M., & Van Bussel, G. J. W. (2014). Estimating atmospheric stability from observations and correcting wind shear models accordingly. *Journal of Physics: Conference Series*, 555 (2014), 012052. <https://doi.org/10.1088/1742-6596/555/1/012052>
- Hu, W., Han, I., Park, S.-C., & Choi, D.-H. (2012). Multi-objective structural optimization of a HAWT composite blade based on ultimate limit state analysis. *Journal of Mechanical Science and Technology*, 26(1), 129–135. <https://doi.org/10.1007/s12206-011-1018-3>
- IEC. (2005). *IEC 61400-1 ed.3: Wind-turbines—Part 1: Design requirements, Technical report, International Electrotechnical Commission*.
- IEC. (2009). *IEC 61400-3 ed.1: Wind-turbines—Part 3: Design requirements for offshore wind turbines, Technical report, International Electrotechnical Commission*.
- Kim, D.-Y., Kim, Y.-H., & Kim, B.-S. (2021). Changes in wind turbine power characteristics and annual energy production due to atmospheric stability, turbulence intensity, and wind shear. *Energy*, 214, 119051. <https://doi.org/10.1016/j.energy.2020.119051>
- Kovalnogov, V. N., Fedorov, R. V., Chukalin, A. V., Tsvetova, E. V., & Kornilova, M. I. (2022). Modeling and Investigation of the Effect of a Wind Turbine on the Atmospheric Boundary Layer. *Energies*, 15(21), Article 21. <https://doi.org/10.3390/en15218196>

- Lange, B., Larsen, S., Højstrup, J., & Barthelmie, R. (2004). Importance of thermal effects and sea surface roughness for offshore wind resource assessment. *Journal of Wind Engineering and Industrial Aerodynamics*, 92(11), 959–988. <https://doi.org/10.1016/j.jweia.2004.05.005>
- Li, L., Liu, Y., Yuan, Z.-M., & Gao, Y. (2019). Dynamic and structural performances of offshore floating wind turbines in turbulent wind flow. *Ocean Engineering*, 179, 92–103. <https://doi.org/10.1016/j.oceaneng.2019.03.028>
- Mallick, P. K. (2008). *Fiber-reinforced composites: Materials, manufacturing, and design* (3rd ed., [expanded and rev. ed.]). CRC Press.
- Marchena, C. J. (2017). *Assessment of the Validity of the Warranted Power Curve in non-standard Wind Conditions: An Empirical Study of the effects of density, turbulence intensity, wind shear, wind veer, and inflow angle on the Power Curve*. <https://repository.tudelft.nl/islandora/object/uuid%3A332b590a-a0ce-4b86-b4e2-d74cf2f6d168>
- Montgomery, D. C. (2013). *Design and analysis of experiments* (Eighth edition). John Wiley & Sons, Inc.
- Moriarty, P. J., & Hansen, A. C. (2005). *AeroDyn Theory Manual* (NREL/TP-500-36881, 15014831; p. NREL/TP-500-36881, 15014831). <https://doi.org/10.2172/15014831>
- Murphy, P., Lundquist, J. K., & Fleming, P. (2020). How wind speed shear and directional veer affect the power production of a megawatt-scale operational wind turbine. *Wind Energy Science*, 5(3), 1169–1190. <https://doi.org/10.5194/wes-5-1169-2020>
- Nikhar J. Abbas, Dzalkind, Mudafort, R. M., Hylander, G., Mulders, S., Davidheff, & Bortolotti, P. (2021). *NREL/ROSCO: Version 2.8.0 (v2.4.0)*. Zenodo. <https://doi.org/10.5281/ZENODO.7818525>
- NREL. (2021). *OpenFAST V.3.0*. <https://github.com/OpenFAST/openfast>

- NREL, Kelley, N., & Jonkman, B. (2021). *TurbSim*. <https://github.com/old-NWTC/TurbSim>
- Redfern, S., Olson, J. B., Lundquist, J. K., & Clack, C. T. M. (2019). Incorporation of the Rotor-Equivalent Wind Speed into the Weather Research and Forecasting Model's Wind Farm Parameterization. *Monthly Weather Review*, *147*(3), 1029–1046. <https://doi.org/10.1175/MWR-D-18-0194.1>
- Ryu, G. H., Kim, D., Kim, D.-Y., Kim, Y.-G., Kwak, S. J., Choi, M. S., Jeon, W., Kim, B.-S., & Moon, C.-J. (2022). Analysis of Vertical Wind Shear Effects on Offshore Wind Energy Prediction Accuracy Applying Rotor Equivalent Wind Speed and the Relationship with Atmospheric Stability. *Applied Sciences*, *12*(14), Article 14. <https://doi.org/10.3390/app12146949>
- Sakagami, Y., Radünz, W. C., Santos, P., Haas, R., Passos, J. C., & Taves, F. F. (2022). Power curve performance of coastal turbines subject to low turbulence intensity offshore winds. *Journal of the Brazilian Society of Mechanical Sciences and Engineering*, *45*(1), 24. <https://doi.org/10.1007/s40430-022-03942-9>
- Scheurich, F., Enevoldsen, P. B., Paulsen, H. N., Dickow, K. K., Fiedel, M., Loeven, A., & Antoniou, I. (2016). Improving the Accuracy of Wind Turbine Power Curve Validation by the Rotor Equivalent Wind Speed Concept. *Journal of Physics: Conference Series*, *753*(7), 072029. <https://doi.org/10.1088/1742-6596/753/7/072029>
- Slot, R. M. M., Svenningsen, L., Sørensen, J. D., & Thøgersen, M. L. (2018). Importance of Shear in Site Assessment of Wind Turbine Fatigue Loads. *Journal of Solar Energy Engineering*, *140*(4). <https://doi.org/10.1115/1.4039748>
- Stull, R. B., & Ahrens, C. D. (2000). *Meteorology for scientists and engineers* (2nd ed). Brooks/Cole. <http://catdir.loc.gov/catdir/enhancements/fy1215/00266104-t.html>

- Teixeira, R., Moreira, P., Tavares, P., Correia, J., Muñiz Calvente, M., De Jesus, A., & Fernández-Canteli, A. (2017). *FATIGUE ANALYSIS OF WIND TURBINE BLADES*.
- Toft, H. S., Svenningsen, L., Moser, W., Sørensen, J. D., & Thøgersen, M. L. (2016). Assessment of wind turbine structural integrity using response surface methodology. *Engineering Structures*, *106*, 471–483.  
<https://doi.org/10.1016/j.engstruct.2015.10.043>
- Valencia, G. E., Cardenas, Y. D., & Acevedo, C. H. (2018). PEST analysis of wind energy in the world: From the worldwide boom to the emergent in Colombia. *Journal of Physics: Conference Series*, *1126*(1), 012019.  
<https://doi.org/10.1088/1742-6596/1126/1/012019>
- van Sark, W., Velde, H., Coelingh, J., & Bierbooms, W. (2019). Do we really need rotor equivalent wind speed? *Wind Energy*, *22*.  
<https://doi.org/10.1002/we.2319>
- Veldkamp, D. (2007). *A probabilistic approach to wind turbine fatigue design*.
- Viselli, A., Faessler, N., & Filippelli, M. (2022). LiDAR Measurements of Wind Shear Exponents and Turbulence Intensity Offshore the Northeast United States. *Journal of Offshore Mechanics and Arctic Engineering*, *144*(4), 042001.  
<https://doi.org/10.1115/1.4053583>
- Wagner, R. (2010). *Simulation of shear and turbulence impact on wind turbine performance*. 56.
- Wagner, R., Cañadillas, B., Clifton, A., Feeney, S., Nygaard, N., Poodt, M., Martin, C. S., Tüxen, E., & Wagenaar, J. W. (2014). Rotor equivalent wind speed for power curve measurement – comparative exercise for IEA Wind Annex 32. *Journal of Physics: Conference Series*, *524*(1), 012108.  
<https://doi.org/10.1088/1742-6596/524/1/012108>

Wind Europe. (2021). *Offshore wind in Europe—Key trends and statistics 2020*.

WindEurope. <https://windeurope.org/data-and-analysis/product/offshore-wind-in-europe-key-trends-and-statistics-2020>

Zaayer, M. (2021). *AE4W02TU Introduction to Wind Turbines: Physics and*

*Technology*. <https://brightspace.tudelft.nl/d2l/le/content/398145/Home>

## Appendix A.

### Measurements of Turbulence Intensity at Hollandse Kust (Zuid) Within 30° Directional Sectors.

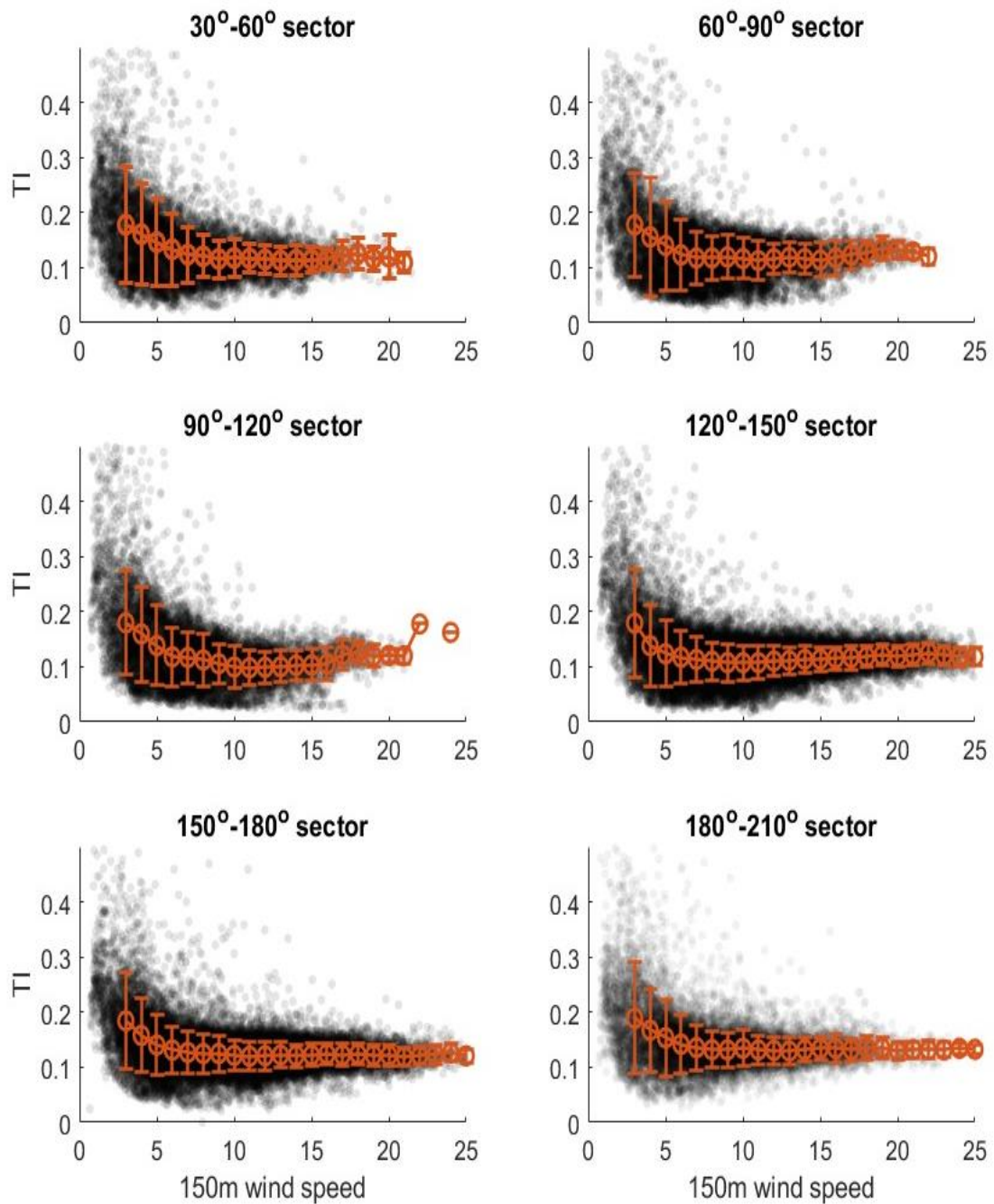


Figure A. 1: Turbulence Intensity measurements at Hollandse Kust (Zuid) wind farm within 30 degrees directional sectors

## Appendix B.

### Calculation of REWS Segment Areas

The process below follows the work of van Sark et al. (2019):

An example will be given on how to calculate the area of five segments of a circle as previously shown in Figure 23. To do so, we will first use a procedure to calculate the shaded area in the circle demonstrated in Figure B. 1. This circular sector has an arc length of  $S$ , a lower chord with length of  $a$ , and a height  $h$ .

The general solution for the area of the shaded part of the circle is: (van Sark et al., 2019)

$$A = R^2 \cos^{-1}\left(\frac{R-h}{R}\right) - (R-h)\sqrt{2Rh-h^2} \quad (B1)$$

If considering an even number of segments (e.g. 5 segments), the upper area of and lower area of the circle would be equal (e.g.  $A_5 = A_1$ ). Both can be directly calculated from Eq. (B1). Note that the height  $h$  for five segments is  $2/5 \cdot R = 0.4R$ .

In order to calculate  $A_2$  (refer to Figure 23), Eq. (B1) will first be utilized to calculate the area  $A_{1\&2}$  which encapsulates the area of both segments  $A_1$  and  $A_2$ . Here, the height  $H$  is equal to  $0.8R$  (the height of the two segments). Next,  $A_2$  can be calculated by subtracting  $A_1$  from  $A_{1\&2}$ . Note again that  $A_2=A_4$ . Therefore, there is only one remaining area which we need to calculate,  $A_3$ .

To calculate  $A_3$ , we can just subtract the areas of the four segments from the overall area of the circle. The same concept can be applied if additional segments need to be considered.

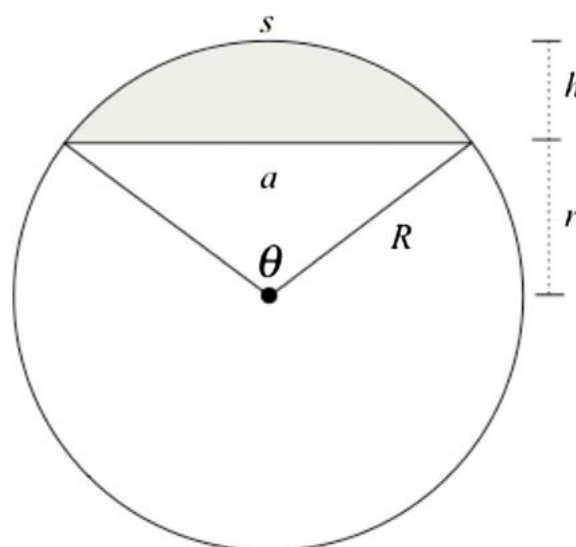


Figure B. 1: Circular sector area calculation (van Sark et al., 2019)

## Appendix C.

### Examples of Calculating the Power Law Exponent Through a Linear Regression in a $\log(z)$ - $\log(u)$ Plot

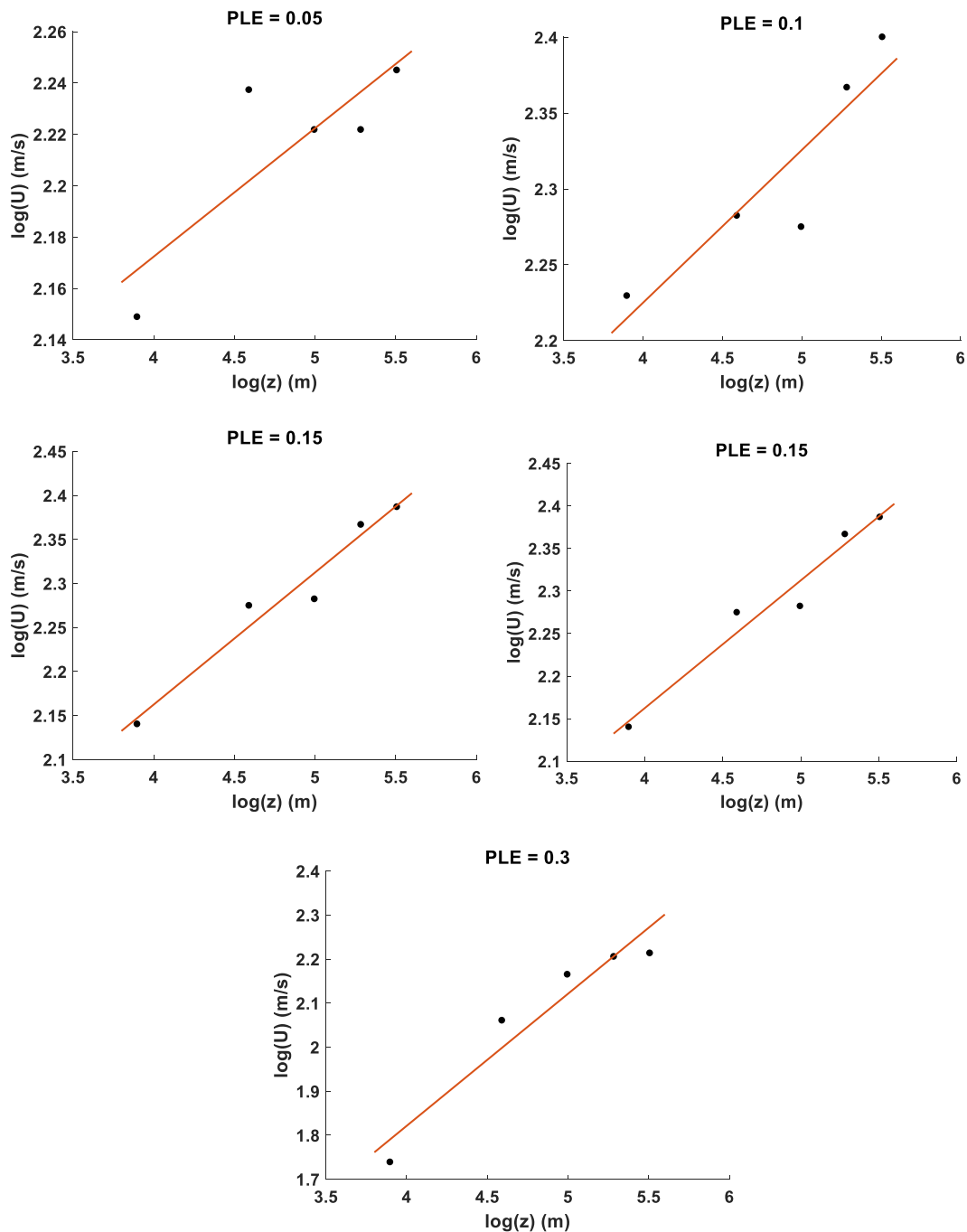


Figure C 1: Examples of calculating the power law exponent using a linear regression in Log